Static and Dynamic Transverse Mode Characteristics of Vertical-Cavity Surface-Emitting Semiconductor Lasers

Ph.D. Thesis

by
Safwat William Zaki Mahmoud
M.Sc. in Physics, El-Minia, Egypt

Work performed
at the Department of Optoelectronics,
Faculty of Engineering Science,
University of Ulm, Germany

Dean of the Faculty: Prof. Dr.-Ing. H.J. Pfleiderer
1st Referee: Prof. Dr. rer. nat. K.J. Ebeling
2nd Referee: Prof. Dr.-Ing. H. Schumacher
Oral examination: 10. June 2002

Preface

This work was supported by the Egyptian Ministry of Education and Scientific Research. As a doctoral student at the Faculty of Science, El-Minia Univeristy, Egypt, I was nominated for a scholarship from the missions department which belongs to this Ministry. After a series of examinations, I was selected for an abroad scholarship to do my Ph.D. research in the field of semiconductor lasers and their applications. I chose Ulm University, Germany since it is one of the leading European centers in optoelectronics. I acknowledge the contributions from the staff of these organizations either in Egypt or in the Egyptian Embassy in Germany.

This work has also been partially supported by the Department of Optoelectronics of Ulm University under a project funded by the German Federal Ministry of Education and Research. During my studies, the department has provided the best research environment. I wish to express my deepest gratitude to Prof. Dr. K.J. Ebeling for being a very devoted supervisor and for getting me started on the subject at his department. His guidance and valuable discussions are greatly appreciated.

I am deeply indebted to Dr.-Ing. R. Michalzik for many helpful discussions during this work and for motivation in any situation. Also, my deep thanks are due to Ursula Wolf for her care for my family.

I would like to express my thanks to all of the Optoelectronics Department's staff for their time and willingness to explain and help me, especially Dr.-Ing. Christian Jung, Dr.-Ing. Dieter Wiedenmann, and Heiko Unold for providing me with the samples for my work and Dr.-Ing. Wolfgang Schmid for his valuable discussions and for sharing the office with me over nearly the whole time of my residence. My deep thanks are due to Dr.-Ing. Klaus Faltin, from Motorola GmbH, Flensburg, for showing me some details about near field measurement setup. I also wish to thank Heiko Unold again for helping me with LaTeX problems while writing this thesis. To them and to those still not referred, I express my deep thanks.

Many thanks go to the department's secretary Christine Bunk for reserving me the apartment and showing me the city of Ulm upon arrival, and also to Sophie Pfetsch for helping

to prepare the foils for my talks in the department seminars and conferences.

Of course, I would like to express my thanks to my wife Nashwa for her support and taking care of our kids Tasnem, Mohammed, and Salsabeel during our residence in Germany.

Finally, my deep thanks from the bottom of my heart are due to my parents, my grandfather Mr. Zaki, and my grandmother for supporting me financially throughout my studies. Their encouragement to continue my studies to higher levels is greatly appreciated.

S.W.Z. Mahmoud
Ulm, Germany
March 2002

Contents

1 Introduction **1**

1.1 Edge-Emitting Lasers 1

1.2 Vertical-Cavity Surface-Emitting Lasers 2

1.3 Arrangement of the Present Work 4

2 Basic Theory of Semiconductor Lasers **5**

2.1 Double-Heterostructure Lasers 5

2.2 Direct and Indirect Semiconductors 6

2.2.1 Energy and momentum conservation 6

2.2.2 Materials for direct and indirect semiconductors 7

2.3 Fabry-Perot Resonator 8

2.4 Standing Wave Pattern in a VCSEL 11

2.5 Simple Model for Quantum Well VCSELs 13

2.6 Bragg Reflector 15

2.7 Threshold Gain and Photon Lifetime 17

2.8 Differential Quantum Efficiency and Conversion Efficiency 19

3 Waveguiding in Oxide-Confined VCSELs **21**

3.1 Theory 21

3.1.1 Formation of an effective index guide in VCSELs 21

3.1.2 Transverse modes of VCSELs 24

3.1.3 Mode spacing of transverse modes 29

3.1.4 Propagation of Gaussian beams 30

3.2 Experiment and Discussion 32

3.2.1 Device output characteristics 32

3.2.2 Near-field analysis 33

3.2.3 Far-field analysis 37

4 Long Monolithic Cavity VCSELs **41**

4.1 Switching Between Longitudinal Modes 41

4.1.1 Device structure and simulations 42

4.1.2 Output characteristics 44

4.1.3 Near-and far-field analyses 45

4.2 Transverse Mode Structure 48

4.2.1 Output characteristics 48

4.2.2 Near-field measurements 49

5 Glass Optical Fibers **59**

5.1 Theory 59

5.1.1 Optical principles and properties 59

5.1.2 Mode profiles in step-index fibers 61

5.1.3 Attenuation by waveguide bends 62

5.1.4 Macrobending of optical fibers 63

5.1.5 Coupling efficiency 65

5.2 Experiment and Discussion 66

5.2.1 Step-index single-mode fibers 66

5.2.2 Graded-index multi-mode fiber 68

6 VCSEL as a Transmitter in Optical Communication Systems **71**

6.1 Requirements on Information Transmission 71

6.2 Optical Fiber Communication Systems 75

6.2.1 Properties of optical information transmission systems 75

6.2.2 Noise sources in optical tansmission systems 76

6.2.3 Detection sensitivity for digital signal 77

6.2.4 Eye diagram 80

6.3 Dynamic behavior of VCSELs 80

6.3.1 Rate equations 81

6.4 Transverse Mode Turn-On Dynamics 83

6.4.1 Device structure and output characteristics 83

6.4.2 Turn-on delay 84

6.4.3 Data Transmission 88

7 Concluding Remarks **95**

References **99**

A Sample Structures **105**

B List of Important Symbols **111**

C List of Own Publications **115**

Chapter 1

Introduction

1.1 Edge-Emitting Lasers

Semiconductor lasers in their conventional form were already demonstrated in the early 1960's. Since then, they have rapidly evolved and nowadays play an important role in our daily lives. They are present in almost every household in CD and CD-ROM players, to name just a few of their applications. The generic architecture of this laser type is shown in Fig. 1.1 [1], [2], where in the given example the amplification takes place in the thin middle GaAs layer. Current is injected uniformly over the whole area to produce population inversion in the semiconductor junction underneath. The light is emitted from the edges of the device, which is cleaved from the semiconductor wafer. Therefore, these devices are known as edge emitting lasers (EELs). Optical confinement in vertical direction is ensured by AlGaAs cladding layers, whereas lateral confinement is usually provided by a waveguide structure through subsequent fabrication steps that are not displayed in Fig. 1.1.

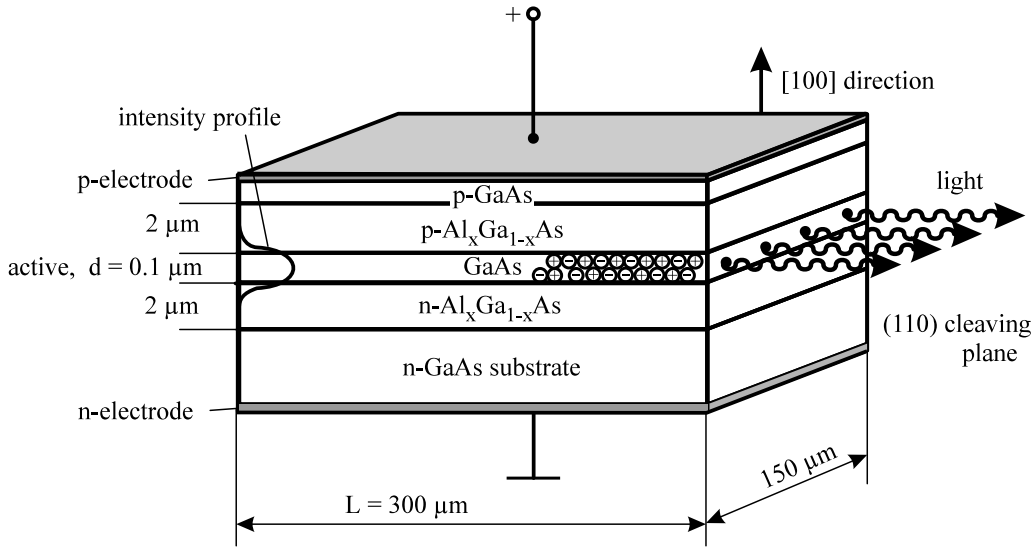


Fig. 1.1: *Schematic view of a broad-area edge-emitting semiconductor laser.*

1.2 Vertical-Cavity Surface-Emitting Lasers

The vertical-cavity surface-emitting laser (VCSEL) is a novel type of semiconductor laser which had been first demonstrated in 1979 [3], but was initially little studied. From the year 1989 on the situation has drastically changed, when by using epitaxially grown semiconductor mirrors, low threshold room temperature operation was demonstrated [4]. Since then, a major technological effort has been put into the development of efficient and reliable VCSEL devices. It is only over the last few years that VCSELs have become commercially available. In Fig. 1.2 a schematic cross section of the VCSEL geometry is shown [1], [5], and [6].

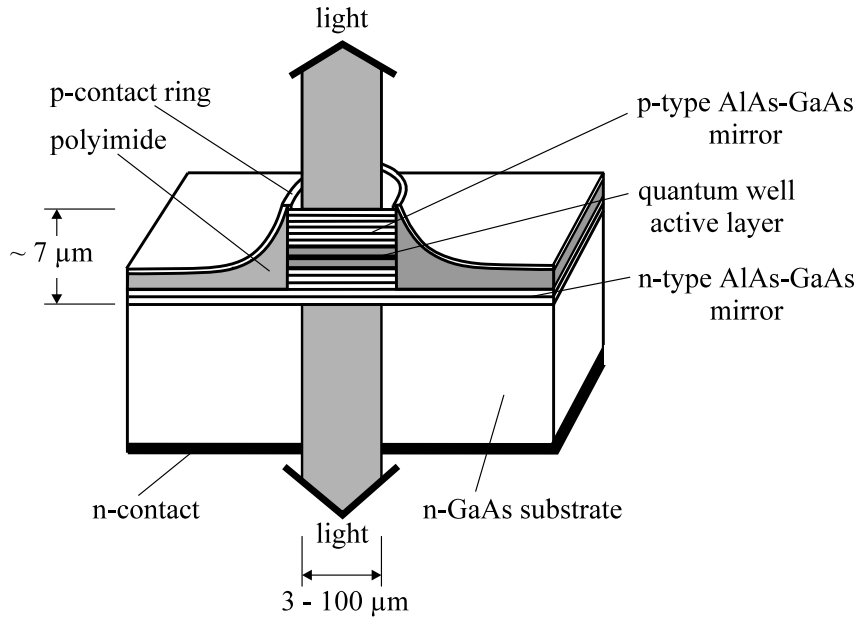


Fig. 1.2: *Schematic view of a vertical-cavity surface-emitting laser diode.*

The inner cavity containing the amplifying layers is surrounded by electrically conductive layer stacks that form the laser mirrors which provide optical feedback. VCSELs designed for emission wavelengths in the 850 to 980 nm spectral range require about 8 μm of epitaxially grown material, whereas the active region is composed of just a few quantum wells (QWs) with some ten nm thickness. Metal organic chemical vapor deposition (MOCVD) or molecular beam epitaxy (MBE) are preferred for crystal growth. The pin-type doping configuration is similar to conventional EELs. In the most simple device layouts, electric current is injected from ohmic contacts on the top epitaxial side and the backside of the substrate. Several methods have been successfully employed to achieve current confinement to a predefined active area. Among those are simple mesa etching of the

top mirror [7], ion implantation to create highly resistive semiconductor regions [8], [9], or selective lateral oxidation [10] of a some ten nm thick semiconductor layer with high aluminum content like $Al_{0.98}Ga_{0.02}As$ or even AlAs. Proton implantation has already been brought to perfection to fabricate commercial VCSELs of outstanding producibility and reliability [11], [12]. On the other hand, selective oxidation introduces less optical losses in the cavity and has produced devices of unrivalled performance [13], [14]. The active diameter of the VCSEL can be reduced to just a few micrometers in order to obtain lowest threshold currents in the sub-100 μA range [15], but can also exceed 100 μm to get high output powers beyond 100 mW [16]. Depending on the wavelength and material composition, VCSELs can be designed for top emission through a ring contact or bottom emission through a transparent substrate.

The different geometry of VCSELs as compared to that of EELs has advantages both for applications and for fabrication. The first difference lies in the cavity length, which for VCSELs is at least two orders of magnitude smaller than for EELs. Typically, this length is 300 μm for EELs, whereas for VCSELs in many cases it comprises only one optical wavelength plus the effective thickness of the distributed laser mirrors. Fabrication of EELs necessarily includes cleavage of the semiconductor wafer while this is not required for VCSELs. Concerning the output beams, EELs emit highly elliptical and strongly divergent beams as a result of the highly asymmetric transverse guiding. In contrast, VCSELs emit a low divergence circular beam, which is advantageous for efficient coupling into optical fibers. On the other hand, the transverse asymmetry in EELs puts strong constraints on the polarization of the output light. Nevertheless, practical VCSELs with a perfect cylindarical symmetry are generally reported to to emit linearly polarized light which, however, has a poor orientational stability [17]. The most obvious advantage of VCSELs over conventional EELs is the possibility to fabricate large two-dimensional arrays. Although from EELs one-dimensional arrays may be produced by employing a number of parallel stripes, the production of two-dimensional arrays is practically impossible. For VCSELs the number of devices that can be processed on one wafer is only limited by the size of the wafer and the minimum distance between the individual devices. The lateral dimensions of a single device can be smaller than 5 μm, which allows very high packing density.

1.3 Arrangement of the Present Work

In this thesis, systematic experimental and theoretical studies on waveguiding mechanisms, mode structure, and mode dynamics in VCSELs are presented. The experiments were all performed on top-emitting VCSELs with an Al_xO_y layer for current confinement.
In Chapter 2, fundamentals of semiconductor lasers are introduced, starting with double heterostructure lasers. Section 2.2 deals with direct and indirect semiconductors, which are necessary to define the conditions for radiative transitions and to classify the materials which satisfy these conditions. This is followed by a section on the Fabry-Perot resonator to study the conditions of threshold gain and resonator modes. In the next five sections, the subject of light propagation in a VCSEL as a multi-layered medium, a model for quantum well VCSELs, Bragg reflectors, laser threshold gain, quantum and conversion efficiencies are considered.
Chapter 3 deals with the waveguiding mechanism in oxide-confined VCSELs and includes two main sections. The first one introduces a theoretical analysis based on the transfer matrix method for the formation of an effective index guide in two samples with different positions of the oxide layer relative to the standing wave pattern in the VCSEL cavity. Also, the transverse LP modes of a VCSEL as a circular waveguide are calculated from the Helmholtz equation under the assumption of a parabolic index profile in a non-absorbing medium. These modes have the same spot size which is proven to be related to the type of index profile. In addition, the propagation of Gaussian beams is derived from the diffraction integral. The second part concerns with experiments which include device output characteristics, optical spectra, and near- and far-field analyses. Interpretations of the observed data are also present throughout the discussion.
Chapter 4 deals with a new class of VCSELs with long monolithic cavity for large area and high power singlemode devices and is devided into two sections. In the first one, switching between longitudinal modes in VCSELs as a new phenomenon is studied from theoretical and experimental points of view. The second section presents experimental comparisons between characteristic curves, spectra, and transverse mode structures of long-cavity VCSELs and the standard devices.
Since VCSELs represent attractive light sources for communication systems, it is important to study the media through which the light can be transmitted. These media are either the singlemode fiber or multimode plastic and glass fibers. Chapter 5 presents some characteristics of the latter type, like eigenmodes, butt-coupling efficiency, and macrobending effects from theoretical and experimental points of view.
Chapter 6 is arranged around the dynamic characteristics of VCSELs and their application as transmitters for optical communication systems. Moreover, spatial investigations of tansverse mode turn-on dynamics in VCSELs are presented.

Chapter 2

Basic Theory of Semiconductor Lasers

This chapter is devoted to a brief description of the conditions needed to obtain a useful lasing structure using a semiconductor. Also, since it will be the main subject of the present work theory of the VCSEL as a novel type of semiconductor laser will be presented in detail to get a better understanding of its design and performance.

2.1 Double-Heterostructure Lasers

The principle of the semiconductor laser is simply to combine a *pn*-junction with a resonant cavity. The recombination of the injected carriers at this junction has to be of radiative type, i.e., be accompanied with emission of photons of the desired wavelength. The optical cavity provides the essential feedback mechanism for optical amplification of these photons and finally yields the laser emission. In order to achieve high carrier densities at low currents it is necessary to confine the recombining carriers to an as small volume as possible. This can be done by using a double-heterostructure where the carriers recombine in an active layer embedded between barrier layers having larger bandgap energies. In Fig. 2.1 a schematic energy band diagram of a laser diode under forward current bias is depicted.

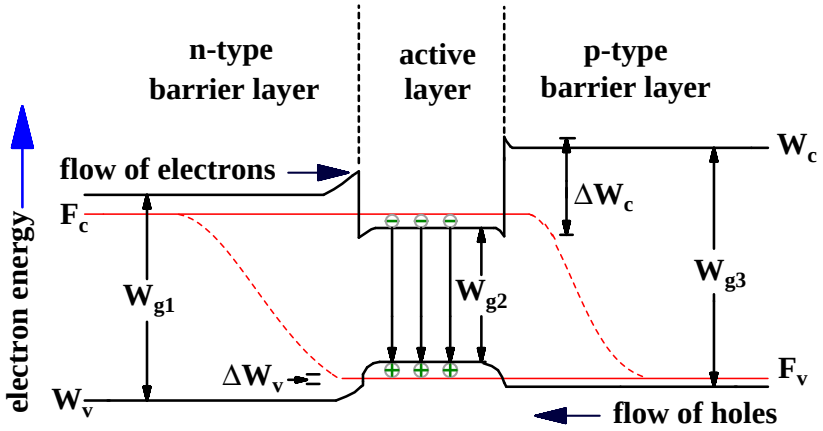


Fig. 2.1: *Schematic band diagram of a double heterostructure laser diode under forward bias.*

The Fermi levels of the conduction and valence bands are denoted as F_c and F_v, respectively, and the energy gaps of the n-type barrier layer, active layer, and p-type barrier layer are W_{g1}, W_{g2}, and W_{g3}, respectively, where usually $W_{g1} = W_{g3}$ is chosen. When the diode is under forward bias, the current flow yields an injection of electrons from the n-doped confinement layer and holes from the p-type barrier layer into the active region. At the interface between the active layer and the p-type barrier, the energy step ΔW_c prevents electrons from leaving the potential well and ΔW_v prevents holes from passing into the n-doped confinement layer. Finally, the injected carriers recombine predominantly in the active layer, since there the electrons in the conduction band with energy W_c find an almost identical number of holes in the valence band with energy W_v.

2.2 Direct and Indirect Semiconductors

2.2.1 Energy and momentum conservation

In semiconductors, an electron transition from a state in the conduction band with energy W_c and wave vector k_c (or momentum $hk_c/2\pi$ with Plank's constant h) to a state in the valence band with energy W_v and wave vector k_v is either radiative or non-radiative. Laser emission relies on radiative transitions and hence according to the conservation of energy and momentum involves a photon with energy

$$h\nu = W_c - W_v \tag{2.1}$$

and momentum

$$k_p = k_c - k_v \quad , \tag{2.2}$$

where ν is the light frequency. For optical frequencies in the near infrared, the wavelength λ (being about 850 nm for GaAs as an example) is more than three order of magnitude larger than the lattice constant $\hat{a}$ ($\hat{a} \approx 0.6$ nm for GaAs). Hence, the photon wave vector $k_p = 2\pi/\lambda$ may be neglected in (2.2), yielding

$$k_c = k_v \quad . \tag{2.3}$$

When the transition obeys (2.1) and (2.3), it is called a direct transition, and the corresponding semiconductors are called direct semiconductors.

2.2.2 Materials for direct and indirect semiconductors

For fiber-optic communications, wavelengths of 1.3 and 1.55 μm are of special significance because optical fibers based on fused silica show zero dipersion and minimum losses (about 0.2 dB/km) at these wavelengths, respectively. Besides these wavelengths, the 0.85 μm and 0.98 μm spectral regions also became very important fiber-optic communication bands for short-distance optical interconnects. Therefore III-V compounds serve as the materials of choice for laser diodes in the 0.7 to 1.6 μm wavelength range. The energy gap versus lattice constant for several families of III-V semiconductors is shown in Fig. 2.2.

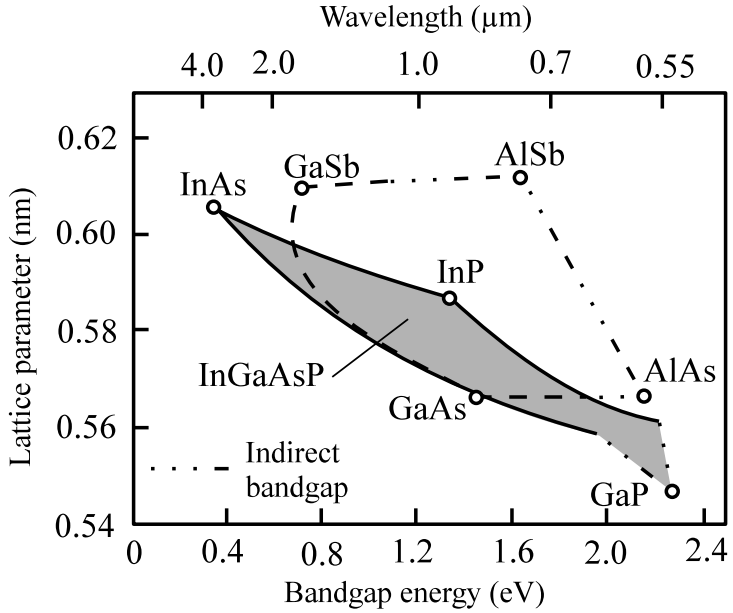


Fig. 2.2: *Lattice constant of various III-V compound semiconductors versus bandgap energy at room temprature and corresponding emission wavelength [18].*

The open circles correspond to binary semiconductors and the connecting lines denote ternary materials. Solid and dashed lines correspond to direct semiconductors whereas the dashed dotted lines indicate indirect ones. Laser diodes which operate at 0.85 μm wavelength are based on GaAs/$Al_xGa_{1-x}As$, where x denotes the relative number of atoms for which Ga is replaced by Al. For $x \leq 0.37$ the material is a direct semiconductor whereas for larger x values it becomes indirect [18]. The bandgap energy of the former is determined in the range for $x \leq 0.37$ by

$$W_g = (1.424 + 1.266x + 0.266x^2)eV \quad . \tag{2.4}$$

Since the direct bandgap and the emission wavelength λ are connected by the relation

$$W_g = hc/\lambda \quad , \tag{2.5}$$

where c is the vacuum velocity of light, lasing from AlGaAs layers is possible in the wavelength region between 620 and 870 nm. One of the most fundamental requirements for these different materials is that they have the same crystal structure and nearly the same lattice constant. In this way an almost defect-free heterostructure crystal can be epitaxially grown. Moreover, it is well known that a lattice mismatch of $\Delta\hat{a}/\hat{a} \approx 1\%$ can be tolerated up to a certain critical layer thickness of around 20 nm without introducing any defects [6]. Such lattice mismatch is commonly employed in active regions from InGaAs/GaAs quantum wells for emission wavelength around 980 nm.

2.3 Fabry-Perot Resonator

Fabry-Perot resonator consists simply of two mirrors separated by a distance L as illustrated schematically in Fig. 2.3. This distance is called the resonator length. An incident wave $E_y = E_0 \exp(-i\gamma z)$ for $z < 0$, polarized in y direction, with the complex amplitude E_0 is reflected back and forth many times at these two mirrors. The propagation consatant $\gamma = \beta - i\alpha/2$ is complex, where α denotes the intensity absorption coefficient and β is the wave number. The amplitude reflection coefficients of the two mirrors r_1 and r_2 are assumed real for simplicity and hence are related to the power reflectivities as $R_1 = r_1^2$ and $R_2 = r_2^2$. The amplitude transmission coefficients for the incident and transmitted waves are denoted by t_1 and t_2, respectively. The resultanting transmitted wave E_{ty} is found by superposition of the transmitted partial waves according to

$$\begin{aligned} E_{ty} &= t_1 t_2 E_0 \exp\{-i\gamma L\} \sum_{j=0}^{\infty} \left[(r_1 r_2)^j \exp\{-2ji\gamma L\} \right] \\ &= \frac{t_1 t_2 E_0 \exp\{-i\gamma L\}}{1 - r_1 r_2 \exp\{-2i\gamma L\}} \quad . \end{aligned} \tag{2.6}$$

Threshold Gain and Resonator Modes

If the denominator in (2.6) becomes zero, an incident wave of finite amplitude produces a transmitted wave of infinitely large amplitude i.e. the condition for laser oscillation is

$$r_1 r_2 \exp(-2i\gamma L) = 1 \quad . \tag{2.7}$$

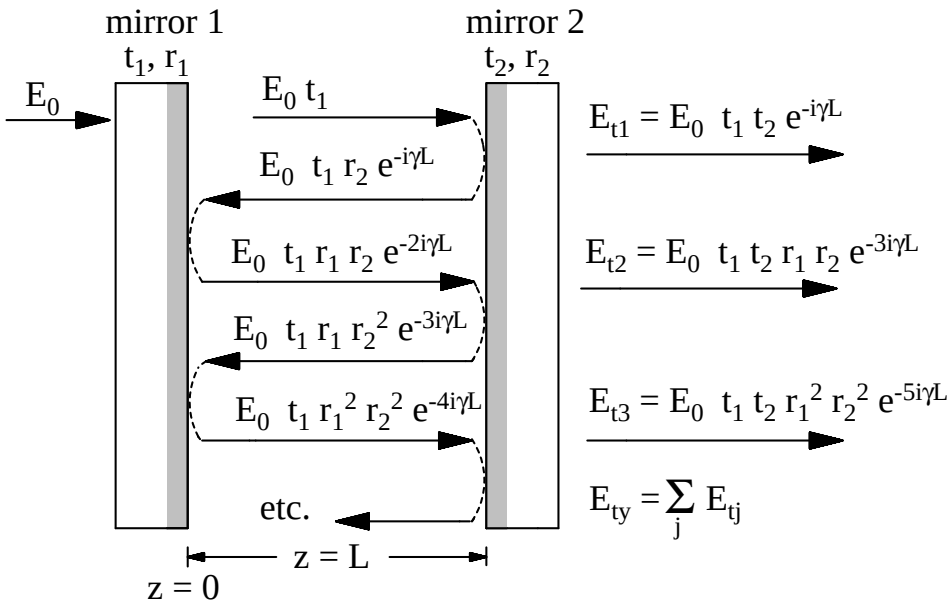


Fig. 2.3: *Schematic of Fabry-Perot resonator.*

This is also known as the threshold condition. The relation between the propagation constant γ, the intensity absorption coefficient α and the refractive index $\bar{n}$ is

$$\gamma = \frac{2\pi}{\lambda}\left(\bar{n} - i\frac{\alpha\lambda}{4\pi}\right) \quad . \tag{2.8}$$

The absorption coefficient α is the sum of the gain g of the laser transition and the intrinsic losses α_i

$$\alpha = \alpha_i - g \tag{2.9}$$

and (2.7) can be written as

$$r_1 r_2 \exp\{(g - \alpha_i)L\} \exp(-4\pi i\bar{n}L/\lambda) = 1 \quad . \tag{2.10}$$

The amplitude leads to the threshold condition

$$r_1 r_2 \exp[(g_{\text{th}} - \alpha_i)L] = 1 \tag{2.11}$$

and the phase gives the resonance condition

$$\frac{4\pi\bar{n}L}{\lambda_m} = 2m\pi \tag{2.12}$$

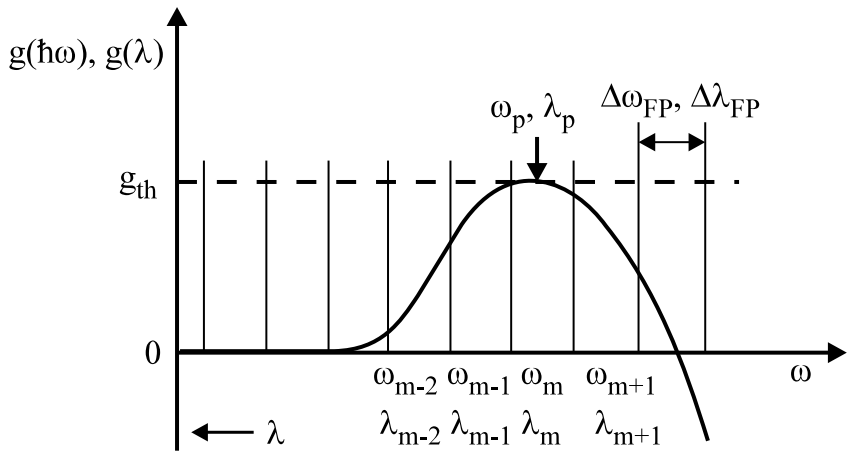


Fig. 2.4: *Wavelength dependence of the material gain of a semiconductor and position of the Fabry-Perot resonances ω_m, λ_m (schematic). The peak gain occurs at ω_p and λ_p.*

with $m = 1, 2, 3$, etc. which determines the possible eigenmodes of the system. The index m is called the order of the mode. The wavelength separation between two neighboring modes $\Delta\lambda_{FP} = \lambda_m - \lambda_{m+1}$ is found to be

$$\Delta\lambda_{FP} = \frac{\lambda^2}{2L\bar{n}(1 - (\lambda/\bar{n})(d\bar{n}/d\lambda))} \quad . \tag{2.13}$$

Fig. 2.4 shows the schematic wavelength dependent gain coefficient and the positions of the resonance wavelengths. The intrinsic losses include material absorption and scattering losses. For realistic current densities of 1 to 10 kA/cm^2 one finds overall gain coefficients on the order of $g = 1000$ cm^{-1}. Intrinsic losses in good crystals lie in the range $\alpha_i = 1$ to 10 cm^{-1}. To a first approximation, in bulk material a linear relationship between peak gain g_p and injected carrier density n can be assumed [1]

$$g_p(n) = a \cdot (n - n_{\mathrm{t}}) \quad . \tag{2.14}$$

The differential gain coefficient amounts to $a = \partial g_p/\partial n \approx 2 \ldots 3 \cdot 10^{-16}\,\mathrm{cm}^2$, and the transparency carrier density is $n_t \approx 2 \cdot 10^{18}\,\mathrm{cm}^{-3}$. For quantum well (QW) material, a better fit is obtained with

$$g_p(n_{\mathrm{w}}) = g_0 \ln(n_{\mathrm{w}}/n_{\mathrm{t,w}}) \quad , \tag{2.15}$$

where the parameters $g_0, n_{\mathrm{t,w}}$ dependent on the material system [6], [19]. For $n > n_{\mathrm{t}}$ or $n_{\mathrm{w}} > n_{\mathrm{t,w}}$ there is positive gain. Because of spontaneous emission into the lasing mode the gain of a semiconductor laser always remains just below the threshold gain

$$g_{\mathrm{th}} = \alpha_i + \frac{1}{L} \ln \frac{1}{\sqrt{R_1 R_2}} \quad , \tag{2.16}$$

as is obtained from (2.11).
For laser oscillation the amplification must obviously compensate for the intrinsic losses and the reflection losses. Laser oscillation will occur at wavelengths which satisfy the resonance condition (2.12) and at which the amplification is at the same time large enough to overcome the intrinsic losses and the reflection losses according to (2.16).

2.4 Standing Wave Pattern in a VCSEL

For designing high performance VCSELs it is important to know the electric field distribution in the resonator. The layer structure of the device can be represented by the multilayer system depicted in Fig. 2.5. For a linearly polarized wave in a one-dimensional approach, the Helmholtz equation describing the wave propagation in z-direction has the form

$$\frac{d^2 E(z)}{dz^2} + \gamma^2 E(z) = 0 \quad . \tag{2.17}$$

The complex propagation coefficient γ defined as before by

$$\gamma_m = \beta_m - i\alpha_m/2 \tag{2.18}$$

is constant in each homogeneous layer of index m and the absorption coefficient fulfills $\alpha_m \geq 0$ except from the quantum well layers where gain leads to $\alpha_m < 0$. The real part β_m of the propagation constant is related to the real part of the refractive index $\bar{n}_m$ by

$$\beta_m = 2\pi \bar{n}_m / \lambda \quad . \tag{2.19}$$

In each layer the phasor of the electric field is the superposition of two monochromatic plane waves of $e^{i\omega t}$ harmonic time dependence ($i = \sqrt{-1}$)

$$E_m(z) = E_m^+ \exp[-i\gamma_m(z - z_m)] + E_m^- \exp[+i\gamma_m(z - z_m)] \tag{2.20}$$

counterpropagating in z-direction. According to Fig. 2.5, E_m^+ and E_m^- denote the complex field amplitudes of the waves in section m at the interface $z = z_m$ with $m = 1, ..., M + 1$.

In nonmagnetic materials, continuity of the electric field $E(z)$ and its derivative dE/dz is required at each interface, leading to conditions

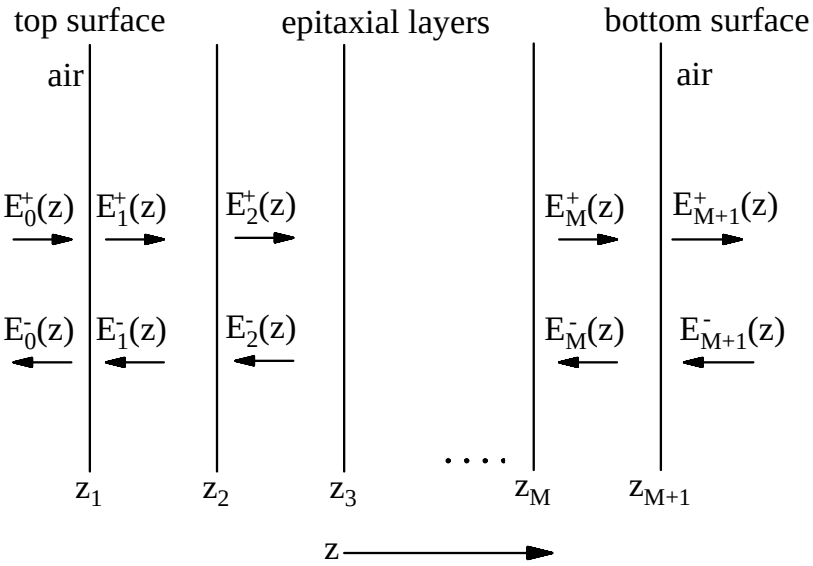


Fig. 2.5: *One-dimensional multilayer structure for the transfer matrix method.*

$$\vec{E}_m = \begin{pmatrix} E_m^+ \\ E_m^- \end{pmatrix} = \begin{pmatrix} Q_m^{++} & Q_m^{--} \\ Q_m^{-+} & Q_m^{+-} \end{pmatrix} \cdot \begin{pmatrix} E_{m+1}^+ \\ E_{m+1}^- \end{pmatrix} = \bar{T}_m \cdot \vec{E}_{m+1} \tag{2.21}$$

for amplitudes in subsequent layers. $\bar{T}_m$ is the so-called transfer matrix with

$$Q_m^{+-} = \gamma_m^+ \exp[-i\gamma(z_{m+1} - z_m)] \tag{2.22}$$

and corresponding definitions for the other elements, where

$$\gamma_m^+ = \frac{\gamma_m + \gamma_{m+1}}{2\gamma_m} \quad \text{and} \quad \gamma_m^- = \frac{\gamma_m - \gamma_{m+1}}{2\gamma_m} \quad . \tag{2.23}$$

The reflection coefficient is defined as the ratio between the backward and the forward travelling wave in region m as

$$r_m = \left.\frac{E_m^-}{E_m^+}\right|_{E_{m+1}^-=0} \quad . \tag{2.24}$$

Also, the transmission coefficient is given by dividing the forward travelling wave amplitude in region $m+1$ by the forward travelling wave amplitude in region m such that the backward travelling wave in medium $m+1$ vanishes, i.e.

$$t_m = \left.\frac{E_{m+1}^+}{E_m^+}\right|_{E_{m+1}^-=0} \quad . \tag{2.25}$$

The reflectance and transmittance are defined respectively as

$$R_m = |r_m|^2 \tag{2.26}$$

and

$$T_m = |t_m|^2 \tag{2.27}$$

and related by

$$R_m + T_m = 1 \tag{2.28}$$

in lossless media. The calculation of the field in the multilayer stack using the matrix notation (2.21) is known as transfer matrix method [20], [21].

In addition to continuity at the interfaces, lasing requires just outgoing waves in the terminating sections $m = 0$ and $m = M + 1$, i.e. [22]

$$E_0^+ = 0 \text{ and } E_{M+1}^- = 0 \quad . \tag{2.29}$$

These kinds of solutions are possible only for sufficiently large gain in the quantum wells. In this case (2.21) along with the conditions in (2.29) determine the lasing wavelength and also the threshold gain.

2.5 Simple Model for Quantum Well VCSELs

An idealized quantum well VCSEL consists of upper and lower Bragg reflectors that are separated by upper and lower cladding layers and active layers of thickness d, as illustrated in Fig. 2.6. Cladding and active layers form the laser cavity of length L. Bragg mirrors have the maximum reflectivity at the Bragg wavelength λ_B. The laser length is chosen as the material wavelength

$$L = \lambda_B/\bar{n} \quad , \tag{2.30}$$

where $\bar{n}$ is the refractive index averaged over active and cladding regions. In the Bragg mirrors the thickness of individual layers is $\lambda_B/(4\bar{n}_l)$ and $\lambda_B/(4\bar{n}_h)$ for the low index AlAs and high index GaAs layers, respectively. The refractive indices are $\bar{n}_l \approx 3.0$ for AlAs and $\bar{n}_h \approx 3.56$ for GaAs. Employing the approach from the previous Section, Fig. 2.6 indicates the standing wave pattern of the electric field established in the cavity and in

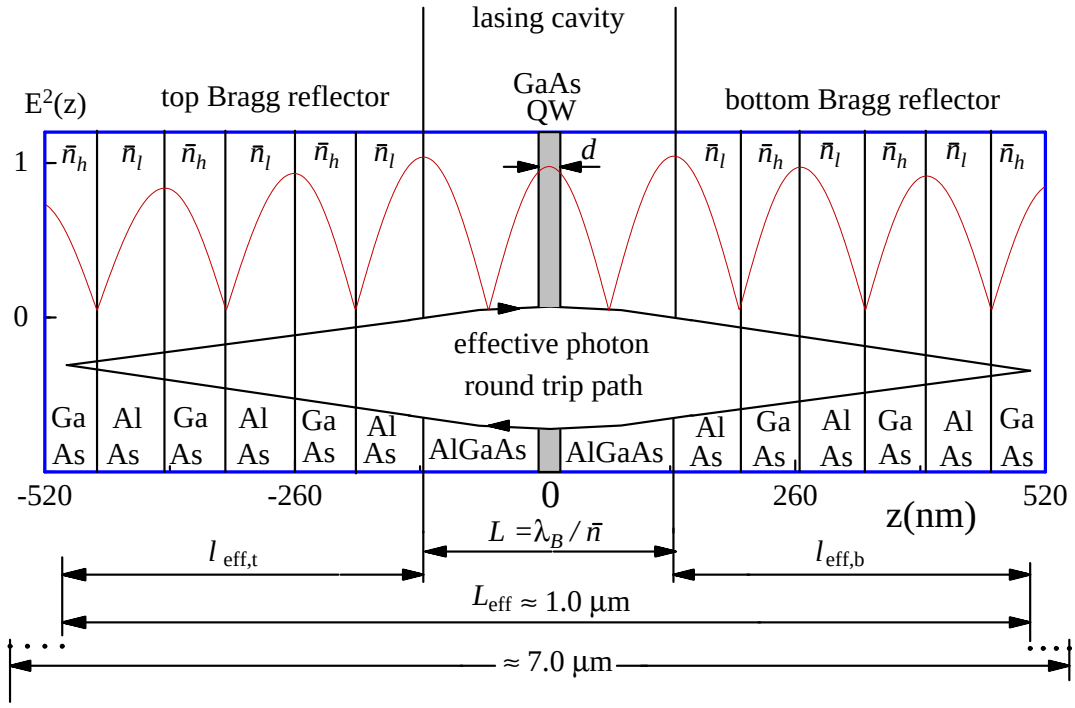


Fig. 2.6: *VCSEL resonator.*

3 mirror pairs of each surrounding Bragg region for clarity. The photons penetrate into the Bragg reflectors such that the effective photon round trip length $2L_{\text{eff}}$ becomes larger than $2L$. With top and bottom penetration depths $l_{\text{eff,t}}$ and $l_{\text{eff,b}}$, respectively, the effective resonator length can be written as

$$L_{\text{eff}} = L + l_{\text{eff,t}} + l_{\text{eff,b}} \quad . \tag{2.31}$$

An analytical expression for the penetration depth will be given in the next section.
To define the suitable thickness d and position of the active gain region in the cavity of length L, the sampling by the standing wave pattern should be taken into account in order to obtain the average gain in the cavity [23], [24]. Accordingly, the relative confinement factor is defined as

$$\Gamma_{\text{r}} = \frac{L}{d} \cdot \frac{\int_{-d/2}^{d/2} |E(z)|^2 dz}{\int_{-L/2}^{L/2} |E(z)|^2 dz} \quad . \tag{2.32}$$

If g is the gain in the quantum well, the average gain in the cavity is given by $\Gamma_{\text{r}} g$. The intensity profile plotted in Fig. 2.6 can be approximated by

$$E^2(z) = E_0^2 \cos^2(2\pi \bar{n} z/\lambda) \tag{2.33}$$

in the inner cavity. The relative confinement factor is then given by

$$\Gamma_{\mathrm{r}} = 1 + \frac{\sin\left(2\pi\bar{n}d/\lambda\right)}{2\pi\bar{n}d/\lambda} \quad . \tag{2.34}$$

Figure 2.7 plots the confinement factor Γ_{r} as a function of the thickness d of GaAs active layer for wavelength $\lambda = 850\,\mathrm{nm}$ and refractive index $\bar{n} = 3.3$. It is seen that Γ_r behaves like *si* function with an amplitude shifted by one i.e. it reaches its maximum value of 2 for a thin quantum well and equals one for thicknesses of multiple integers of $\lambda/2\bar{n}$. For a VCSEL with three 8 nm thick quantum wells separated by 10 nm barriers located in the center of the cavity one has $\Gamma_{\mathrm{r}} \approx 1.8$. By exploiting the standing wave effect, one can therefore almost double the available amount of optical amplification. Obviously it is required that the quantum well be placed in an antinode of the standing wave pattern to provide a good coupling between electrons and photons.

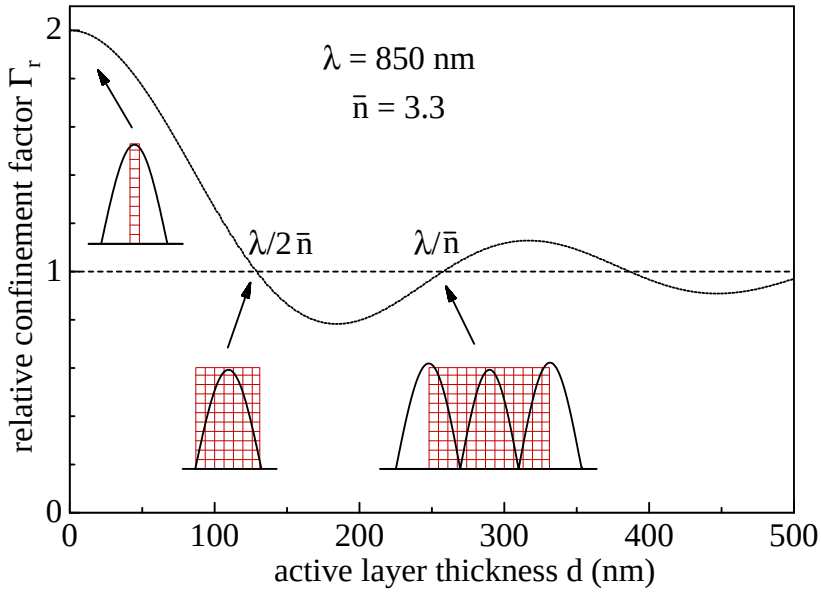


Fig. 2.7: *Dependence of the relative confinement factor Γ_r on the thickness d of the active layer.*

2.6 Bragg Reflector

Bragg reflectors typically consist of an alternating sequence of high and low refractive index layers with quarter-wavelength thickness. Field distributions and reflectivity spectra are suitably calculated by the transfer matrix method. Alternatively, the theory of coupled modes for the Bragg reflector [1] provides simple approximate analytical expressions that

are extremely helpful to understand the properties of the multilayer structure. For M_B mirrors pair with layers of thicknesses $d_l = \lambda_B/(4\bar{n}_l)$ and $d_h = \lambda_B/(4\bar{n}_h)$ the total thickness of the Bragg reflector is

$$L_B = M_B(d_l + d_h) = M_B \frac{\lambda_B}{4}\left(\frac{1}{\bar{n}_l} + \frac{1}{\bar{n}_h}\right) \quad . \tag{2.35}$$

The coupling coefficient is defined as

$$\kappa = 2\Delta\bar{n}/\lambda_B \quad , \tag{2.36}$$

where $\Delta\bar{n} = \bar{n}_h - \bar{n}_l$ is the refractive index difference of the composing layers in the structure. The intensity reflection coefficient is given by

$$R = \tanh^2(\kappa L_B) = \tanh^2\left(\frac{M_B}{2}\left[\frac{\bar{n}_h}{\bar{n}_l} - \frac{\bar{n}_l}{\bar{n}_h}\right]\right) \quad . \tag{2.37}$$

For $\bar{n}_h = 3.56$, $\bar{n}_l = 3.0$, and $M_B = 16$ one obtains $R = 99.2$ %. For incidence from a high index material the phase φ_r of the complex amplitude reflection coefficient $r = \sqrt{R}e^{i\varphi_r}$ is zero at the Bragg wavelength but varies linearly with phase coefficient or inverse wavelength deviation, i.e.

$$\varphi_r = 2l_{\text{eff}}(\beta_B - \beta) = 4\pi l_{\text{eff}}\left(\frac{\bar{n}(\lambda_B)}{\lambda_B} - \frac{\bar{n}(\lambda)}{\lambda}\right) \quad . \tag{2.38}$$

As already indicated in Fig. 2.6, the effective length l_{eff} is to be considered as the penetration depth of the incident wave into the Bragg reflector. From the phase change the penetration depth is obtained as

$$\begin{aligned} l_{\text{eff}} &= -\frac{1}{2}\frac{d\varphi_r}{d\beta} = \frac{\lambda^2}{4\pi\langle\bar{n}_g\rangle}\frac{d\varphi_r}{d\lambda} = \frac{\tanh(\kappa L_B)}{2\kappa} \\ &= \frac{\sqrt{R}}{2\kappa} = \frac{\sqrt{R}\lambda_B}{4\Delta\bar{n}} \approx \frac{\lambda_B}{4\Delta\bar{n}} \quad , \end{aligned} \tag{2.39}$$

where $\langle\bar{n}_g\rangle$ is the spatially averaged group index

$$\bar{n}_g = \bar{n} - \lambda d\bar{n}/d\lambda \tag{2.40}$$

and the approximation on the right-hand side of (2.39) is valid for $\sqrt{R} \approx 1$. The values of $\lambda_B = 980\,\text{nm}$ and $\Delta\bar{n} = 0.56$ for AlAs-GaAs mirrors [25] give $l_{\text{eff}} \approx 438\,\text{nm}$. Bragg reflectors of sufficiently large κL_B product show a broad spectral plateau around the

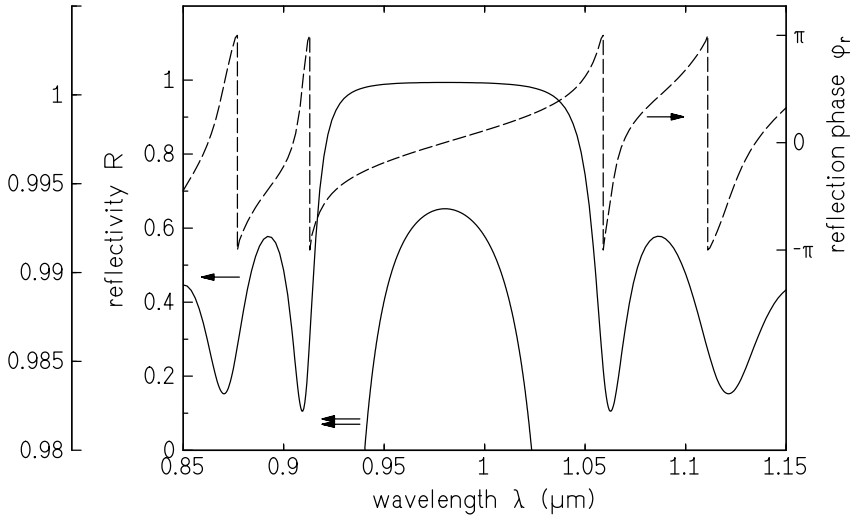


Fig. 2.8: *Spectral dependence of the intensity reflection coefficient R and the phase φ_r of the amplitude reflection coefficient for a Bragg mirror consisting of 16 pairs of AlAs-GaAs layers with 20 cm^{-1} intrinsic absorption coefficient. Surroundings are $Al_{0.3}Ga_{0.7}As$ at the bottom and air at the top. The outer left hand ordinate presents details of $R(\lambda)$ in the center of the stop band. Incidence is from the AlGaAs side [26].*

Bragg wavelength where the reflection coefficient is large. The width of this stop band is roughly estimated from [1], [21]

$$\Delta\lambda_{stop} = \frac{2\lambda_B \Delta\bar{n}}{\pi\langle\bar{n}_g\rangle} \quad . \tag{2.41}$$

The AlAs-GaAs Bragg reflector considered has $\Delta\lambda_{stop} \approx 100$ nm. Figure 2.8 shows spectral reflectivity R and phase φ_r for a 16 pair AlAs-GaAs Bragg reflector calculated with the transfer matrix approach. It is seen that the approximate results obtained from the coupled mode theory are well supported.

2.7 Threshold Gain and Photon Lifetime

For lasing the gain in the cavity has to overcome the losses. With intrinsic losses α_i and α_a in the passive and active sections, respectively, considerations of gain enhancement and penetration of the waves into Bragg reflectors lead to the lasing threshold condition

$$g_{\text{th}} = \alpha_a + \frac{1}{\Gamma_r d}\left[\alpha_i(L_{\text{eff}} - d) + \ln\frac{1}{\sqrt{R_t R_b}}\right] \quad , \tag{2.42}$$

where L_{eff} is given by (2.31) and d represents the total thickness of the active layer. The intrinsic absorption coefficient is a spatial average over the locally varying absorption

coefficient where weighting with the standing wave intensity profile has to be applied. The intensity reflection coefficients R_t and R_b are valid for lossless mirrors and can be determined from (2.37). Alternatively, the threshold condition can be formulated using the maximum reflectivity of a Bragg mirror with homogeneously distributed losses

$$R_\alpha = R \exp\{-2\alpha_i l_{\text{eff}}\} \approx R(1 - 2\alpha_i l_{\text{eff}}) \quad , \tag{2.43}$$

where in the case of small losses with $2\alpha_i l_{\text{eff}} \ll 1$ the approximation in the right-hand side can be applied. Thereby it is assumed that the wave traverses the distance l_{eff} back and forth and experiences losses α_i. Due to mirror losses the maximum achievable reflectivity is limited to values less than one even in the case of an infinite number M_B of Bragg pairs.

Using (2.43) the threshold condition (2.42) is rewritten as

$$g_{\text{th}} = \alpha_a + \frac{1}{\Gamma_{\text{r}} d}\left[\alpha_i(L-d) + \ln\frac{1}{\sqrt{R_{t\alpha}R_{b\alpha}}}\right] \quad , \tag{2.44}$$

where the effective length L_{eff} is now replaced by the inner cavity length L. Assuming equal intrinsic losses $\alpha_i = \alpha_a$ the photon lifetime τ_p in the cavity can be expressed as

$$\frac{1}{\tau_p} = \frac{c}{\langle \bar{n}_g \rangle}\left(\alpha_i - \frac{1}{L_{\text{eff}}}\ln\sqrt{R_t R_b}\right) \quad . \tag{2.45}$$

As an example, with $\langle \bar{n}_g \rangle = 3.6$, $L_{\text{eff}} = 1.2\ \mu$m, $R_t = R_b = 99.2\ \%$ and $\alpha_i = 20\ \text{cm}^{-1}$ one obtains $\tau_p = 1.4$ ps.

From 2.13 the longitudinal mode spacing is now estimated from

$$\Delta\lambda_m = \frac{\lambda^2}{2L_{\text{eff}}\langle \bar{n}_g \rangle} \quad . \tag{2.46}$$

For $\lambda = \lambda_B = 980\,\text{nm}$ one obtains $\Delta\lambda_m = 110\,\text{nm}$ which is similar to the stop band width 2.41 and larger than the spectral gain bandwidth of the quantum well material. Therefore just a single longitudinal mode can oscillate in a VCSEL with a short inner cavity. However, depending on the lateral size of the VCSEL several transverse modes may oscillate simultaneously.

2.8 Differential Quantum Efficiency and Conversion Efficiency

Above threshold current I_{th}, top and bottom light output powers P_{t} and P_{b} linearly increase with driving current I [5]–[6] as

$$P_{\mathrm{t,b}} = \eta_{\mathrm{i}}\eta_{\mathrm{dt,b}}\frac{\hbar\omega}{q}(I - I_{\mathrm{th}}) \;, \tag{2.47}$$

where an internal quantum efficiency η_{i} is introduced to exclude current and carrier leakage that do not contribute to the generation of coherent emission. The differential quantum efficiency $\eta_{\mathrm{dt,b}}$ characterizes the percentage of generated coherent light that is available in the top or bottom radiation, and $\hbar\omega$, q denote photon energy and electron charge, respectively. In well designed VCSELs with high quality active QWs, $\eta_{\mathrm{i}} > 90\,\%$ can be achieved. Due to absorption in the mirrors, $\eta_{\mathrm{dt}} + \eta_{\mathrm{db}}$ is always less than 100 %. In fact, the emitted coherent power is related to the time averaged Poynting vector [1]

$$\vec{S} = \mathrm{Re}\{\vec{E} \times \vec{H}^*\} \tag{2.48}$$

with $*$ denoting complex conjugation. In the one-dimensional with $\vec{E} = (E_x, 0, 0)^T$ used in Section 2.4 the linearly polarized magnetic field is

$$H = H_y = \frac{i}{\omega\mu_0}\frac{dE_x}{dz} \;, \tag{2.49}$$

and thus energy flux occurs in $\pm z$-directions only. Substitution of (2.20) and (2.49) into (2.48) yields for the energy flux in section m of the multilayer structure the expression

$$\begin{aligned} S_m(z) \;=\; & \frac{\beta_m}{\omega\mu_0}|E_m^+|^2\exp\{-\alpha_m(z-z_m)\} - \frac{\beta_m}{\omega\mu_0}|E_m^-|^2\exp\{\alpha_m(z-z_m)\} \\ & + \frac{\alpha_m}{\omega\mu_0}\,\mathrm{Im}\left\{E_m^+(E_m^-)^*\exp\{-i2\beta_m(z-z_m)\}\right\} \;. \end{aligned} \tag{2.50}$$

The first and second term describe the energy flux of the forward and backward propagating waves, respectively. The third term takes into account energy exchange that arises in media with gain or loss. The differential quantum efficiency for top and bottom emission $\eta_{\mathrm{d}} = \eta_{\mathrm{dt}} + \eta_{\mathrm{db}}$ is identified as the fraction of the generated flux that is emitted through top or bottom mirrors, i.e. [26], [27]

$$\eta_{\mathrm{d}} = \frac{g_{\mathrm{th}}}{g_{\mathrm{th}} + \alpha_{\mathrm{a}}}\left(1 + \frac{\sum_{i,\mathrm{pass.}}\Delta S_i}{\sum_{i,\mathrm{act.}}\Delta S_i}\right) \quad \text{with} \quad \Delta S_i = S(z_{i+1}) - S(z_i) \;, \tag{2.51}$$

where g_{th} is the threshold gain previously determined by the transfer matrix method. The sum in the numerator or denominator extends over all passive or active segments,

respectively. Obviously, absorption leads to flux increments $\Delta S_i < 0$ and thus to $\eta_\mathrm{d} < 1$. Denoting top and bottom emitted energy flux by $S_\mathrm{t} = S(z_1) < 0$ and $S_\mathrm{b} = S(z_{M+1}) > 0$, respectively, the corresponding differential quantum efficiencies are

$$\eta_\mathrm{dt} = \eta_\mathrm{d} \frac{|S_\mathrm{t}|}{|S_\mathrm{t}| + |S_\mathrm{b}|} \qquad \text{and} \qquad \eta_\mathrm{db} = \eta_\mathrm{d} \frac{|S_\mathrm{b}|}{|S_\mathrm{t}| + |S_\mathrm{b}|} \; . \tag{2.52}$$

Wallplug or conversion efficiency η_c for emission through the top or bottom mirror is defined as the ratio of coherent light output power and electrical input power

$$\eta_\mathrm{ct,b} = \frac{P_\mathrm{t,b}}{IV} \; , \tag{2.53}$$

where V is the voltage applied across the VCSEL. In an ideal device, the current-voltage characteristics can be approximated as [24]

$$V \approx V_\mathrm{k} + R_\mathrm{s} I \; , \tag{2.54}$$

where $R_\mathrm{s} = dV/dI$ denotes the differential series resistance, and the kink voltage V_k is related to the separation of the quasi-Fermi energies but can be approximated by $V_\mathrm{k} \approx \hbar\omega/q$. Non-perfect grading of heterointerfaces induces a larger voltage offset accompanied by a pronounced curvature of the I-V characteristics [28]. Combining (2.47), (2.53), and (2.54) leads to

$$\eta_\mathrm{ct,b} = \eta_\mathrm{dt,b} \eta_\mathrm{i} \frac{\hbar\omega}{q} \frac{I - I_\mathrm{th}}{IV_\mathrm{k} + I^2 R_\mathrm{s}} \; , \tag{2.55}$$

showing that for $I \gg I_\mathrm{th}$ the series resistance is responsible for the decrease of $\eta_\mathrm{ct,b}$ with increasing current.

Chapter 3

Waveguiding in Oxide-Confined VCSELs

The performance of VCSELs has greatly advanced in recent years. The use of Al_xO_y apertures for fabrication constricts the current flow into the active region and consequently gives rise to reduced threshold and high efficiency as has been achieved in [15], [29]. Furthermore, transverse optical confinement occurs due to the reduced refractive index of the dielectric aluminum oxide. This chapter consists of two main sections. The first one presents the simulations based on the transfer matrix method (TMM) to explain the waveguiding mechanism in this type of VCSEL for two different samples with two different positions of the oxide layer relative to the standing wave pattern in the cavity. By solving the Helmholtz equation in cylindrical coordinates, the resulting eigenfunctions give the transverse modes of VCSEL and the eigenvalues can be used to estimate their mode spacing. Moreover, the propagation of Gaussian beams using the diffraction integral is presented. The second section presents experimental analyses concerning the device output characteristics, spectra, and near- and far-field measurements. The latter concentrate on the fundamental LP_{01} mode to show how this mode is confined by the induced refractive index due to the presence of the oxide layer in the cavity.

3.1 Theory

3.1.1 Formation of an effective index guide in VCSELs

The lasers under investigation are designed for the emission near 850 nm wavelength. The layer structure of these devices is described in tables A.1, A.2 in Appendix A, where the one wavelength thick inner cavity contains three active quantum wells, composed of 8 nm thick GaAs separated by 10 nm $Al_{0.2}Ga_{0.8}As$ barriers. The n-type bottom distributed Bragg reflector (DBR) consists of 39.5 silicon doped $AlAs/Al_{0.2}Ga_{0.8}As$ pairs. The p-type top DBR consists of 23 pairs of carbon doped $Al_{0.9}Ga_{0.1}As/Al_{0.2}Ga_{0.8}As$. Lateral current confinement is achieved by partial wet oxidation of a single 30 nm thick AlAs layer embedded in a quarter-wavelength layer, three mirror periods from the active region for sample M46/97, and directly above the active region for sample M108/97. The resulting aluminum oxide Al_xO_y is electrically isolating and thus provides an aperture for current

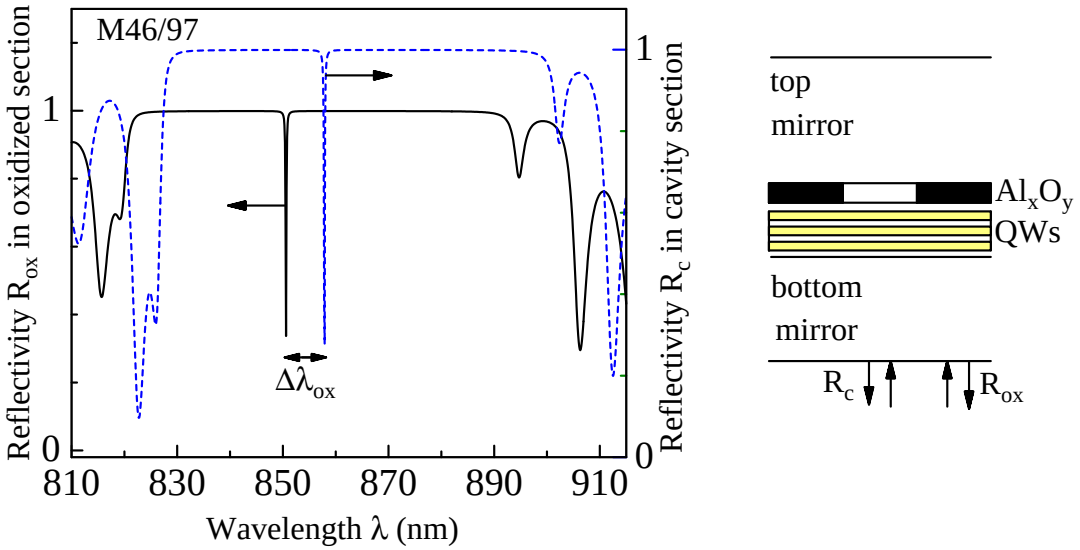


Fig. 3.1: *Calculated reflectivity spectra in the cavity section and the oxidized section of the selectively oxidized VCSEL structure given in the text (left), and schematic cross-section of the device (right).*

injection, as illustrated schematically in Fig. 3.1.
Since the refractive index of Al_xO_y has a value of $\bar{n}_{ox} = 1.6$ [30] which is nearly half that of AlAs, one can expect a built-in refractive index step in the active region due to the reduction of the mean refractive index $\langle\bar{n}\rangle$ in the passive part of the laser. Figure 3.1 shows the calculated reflectivity spectrum $R_c(\lambda)$ using the one-dimensional TMM for this VCSEL structure without Al_xO_y layer. When this layer is considered in the calculations, the reflectivity spectrum $R_{ox}(\lambda)$ shows a detuning in the cavity resonance wavelength by an amount $\Delta\lambda_{ox}$. A theoretical formula relating the induced built-in refractive index step to this detuning has been given in the form [31]

$$\Delta\bar{n}_{ox} = \Delta\lambda_{ox}\frac{\langle\bar{n}\rangle}{\lambda_0} \tag{3.1}$$

where λ_0 is the resonance wavelength in the absence of the oxide layer. In the top part of Fig. 3.2, the calculated field amplitude (solid curve) for a plane wave at the resonance wavelength is shown for the present VCSEL. Also this figure illustrates the calculated refractive index change (open circles) using (3.1) at different positions of the oxide layer relative to the standing wave pattern for an oxide thickness $d_{ox} = 30\,\text{nm}$. It is seen that $\Delta\bar{n}_{ox}$ varies periodically with the longitudinal position of the oxide layer. This oscillation is similar to that of the amplitude, i.e., it reaches its minimum or maximum value when the Al_xO_y layer lies at a node or antinode of the standing wave pattern in the cavity, respectively. The solid square and triangle in this figure define the position of the oxide

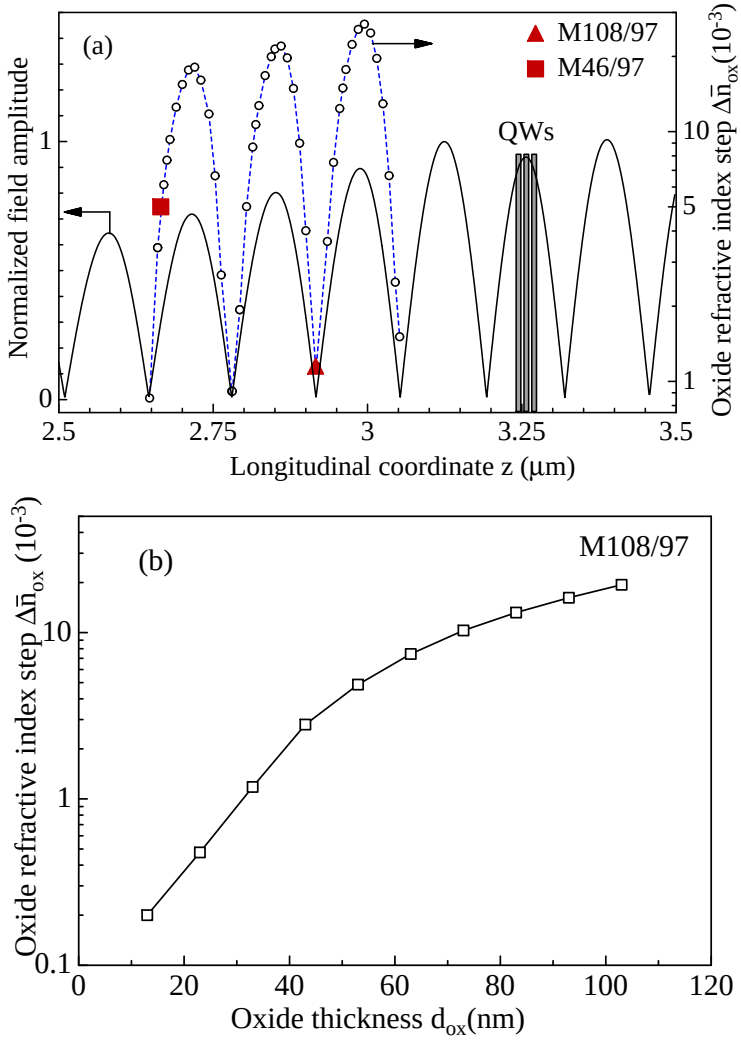


Fig. 3.2: *Calculated resonant standing wave pattern and refractive index change for different longitudinal positions of the oxide layer within the VCSEL of Fig. 3.1 (a) and dependence of the effective refractive index change on the thickness of the oxide layer which is centered in the node of the standing wave pattern at z= 2.92 µm (b).*

layer and at the same time the refractive index change for samples M46/97 and M108/97, respectively. For the latter, in which the oxide layer lies exactly at the node of the standing wave pattern, Fig. 3.2(b) reveals an increase of the induced refractive index step when increasing the oxide layer thickness. According to these simulations the oxide layer has to be placed in a node of the standing wave pattern to reduce the induced refractive index step. In addition, its thickness should also be as small as possible, where $d_{ox} \approx 20\,nm$ might be regarded as practical lower limit for the selective oxidation process and to be on the safe side considering voltage breakthrough and carrier tunneling effects.

3.1.2 Transverse modes of VCSELs

The circularly symmetric oxidized VCSEL structure can be approximated by a cylindrical waveguide with effective refractive indices $\bar{n}_c$ for the core and $\bar{n}_{\mathrm{cl}}$ for the cladding, as illustrated in Fig. 3.3. The core radius a_c is identical to the width of the oxide aperture. Neglecting losses, the Helmholtz equation can be written in cylindrical coordinates (r, φ, z) as [32]

$$\nabla^2 E(r,\varphi,z) + \bar{n}^2(r)\left(\frac{2\pi}{\lambda}\right)^2 E(r,\varphi,z) = 0 \quad . \tag{3.2}$$

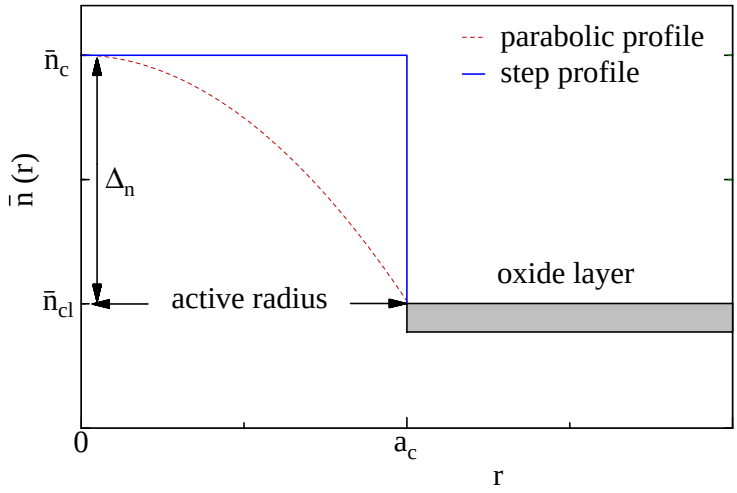


Fig. 3.3: *Cavity model with step or parabolic radial refractive index profiles* $\bar{n}(r)$.

The solutions of this differential equation have the form

$$E(r,\varphi,z) = \Psi(r)\left\{\begin{matrix}\cos l\varphi \\ \sin l\varphi\end{matrix}\right\}\exp(-i\beta z) \tag{3.3}$$

with a non-negative integer l and a choice of either $\cos l\varphi$ or $\sin l\varphi$ azimuthal dependence. Putting (3.3) in (3.2) gives

$$\frac{d^2\Psi}{dr^2} + \frac{1}{r}\frac{d\Psi}{dr} + k_r^2\Psi = 0 \tag{3.4}$$

for the radial profile $\Psi(r)$, where the radial propagation constant k_r is given by

$$k_r^2 = \bar{n}^2(r)4\pi^2/\lambda^2 - \beta^2 - l^2/r^2 \quad . \tag{3.5}$$

The radial refractive index profile produced in the core is approximated by the truncated parabolic profile

$$\bar{n}^2(r) = \begin{cases} \bar{n}_c^2(1 - 2\Delta r^2/a_c^2) & \text{for } r \le a_c, \\ \bar{n}_{\mathrm{cl}}^2 = const & \text{for } r > a_c \end{cases} \tag{3.6}$$

with the normalized refractive index difference between center and cladding

$$\Delta = \frac{\bar{n}_{\mathrm{c}}^2 - \bar{n}_{\mathrm{cl}}^2}{2\bar{n}_{\mathrm{c}}^2} \approx \frac{\bar{n}_{\mathrm{c}} - \bar{n}_{\mathrm{cl}}}{\bar{n}_{\mathrm{c}}} = \frac{\Delta_{\mathrm{n}}}{\bar{n}_{\mathrm{c}}} \quad . \tag{3.7}$$

The approximation on the right-hand side holds for $\bar{n}_{\mathrm{c}} - \bar{n}_{\mathrm{cl}} \ll \bar{n}_{\mathrm{c}}$ which is always the case. Solutions of (3.4) for a full parabolic profile are given by Laguerre-Gaussian functions

$$\Psi(r) = \sqrt{\frac{2}{\pi}\frac{(p-1)!}{(p-1+l)!}}\frac{1}{w_0}\left(\frac{\sqrt{2}r}{w_0}\right)^l L_{p-1}^{(l)}\left(\frac{2r^2}{w_0^2}\right)\exp\left\{-\frac{r^2}{w_0^2}\right\} \quad , \tag{3.8}$$

where $L_{p-1}^{(l)}$ is the generalized Laguerre polynomial of kind l and integer order defined by $(q \geq 0)$

$$L_q^{(l)}(u) = \sum_{\nu=0}^{q}\binom{q+l}{q-\nu}\frac{(-1)^\nu}{\nu!}u^\nu \quad . \tag{3.9}$$

Low order generalized Laguerre polynomials are

$$\begin{aligned} L_0^{(l)}(u) &= 1, \quad L_1^{(l)}(u) = 1 + l - u \ , \\ L_2^{(l)}(u) &= (1/2)(l+1)(l+2) - (l+2)u + u^2/2 \quad . \end{aligned} \tag{3.10}$$

The parameter w_0 is the spot radius given by

$$w_0 = a_{\mathrm{c}}\sqrt{2/\bar{V}} \tag{3.11}$$

with the frequency parameter

$$\bar{V} = \frac{2\pi a_{\mathrm{c}}}{\lambda}\sqrt{\bar{n}_{\mathrm{c}}^2 - \bar{n}_{\mathrm{cl}}^2} = 2\pi\bar{n}_{\mathrm{c}}a_{\mathrm{c}}\sqrt{2\Delta}/\lambda \quad . \tag{3.12}$$

The solutions (3.8) for the full parabolic profile are assumed to be reasonably accurate approximate solutions also for the parabolic profile (3.6) if the amplitude decay is sufficiently large at the boundary $r = a_c$. Putting (3.8) into (3.3) gives the near field intensity profiles of transverse modes L_{lp} written as

$$S_{lp}(r,\varphi) \propto |E_{lp}(r,\varphi)|^2 \propto \left(\frac{2r^2}{w_0^2}\right)^l \left[L_{p-1}^{(l)}\left(\frac{2r^2}{w_0^2}\right)\right]^2 \left\{\begin{matrix}\cos^2(l\varphi)\\ \sin^2(l\varphi)\end{matrix}\right\} \exp\left\{-\frac{2r^2}{w_0^2}\right\} \quad . \tag{3.13}$$

Figure 3.4 shows the intensity distributions of the first twelve transverse LP_{lp} modes calculated using (3.13) with identical spot size w_0. Instead of $\cos(l\varphi)$, alternatively $\sin(l\varphi)$ or the superposition of both is used for $l > 0$. As can be seen, the intensity distributions of the LP_{l1}^* modes with $l > 0$ (so-called donut-modes), where $*$ denotes the superposition between cos and sin solutions, look the same, but the maxima are further displaced from the origin as the order l increases. The same observation is made for the transverse modes LP_{l2}^*, LP_{l3}^*, etc., again with $l > 0$.

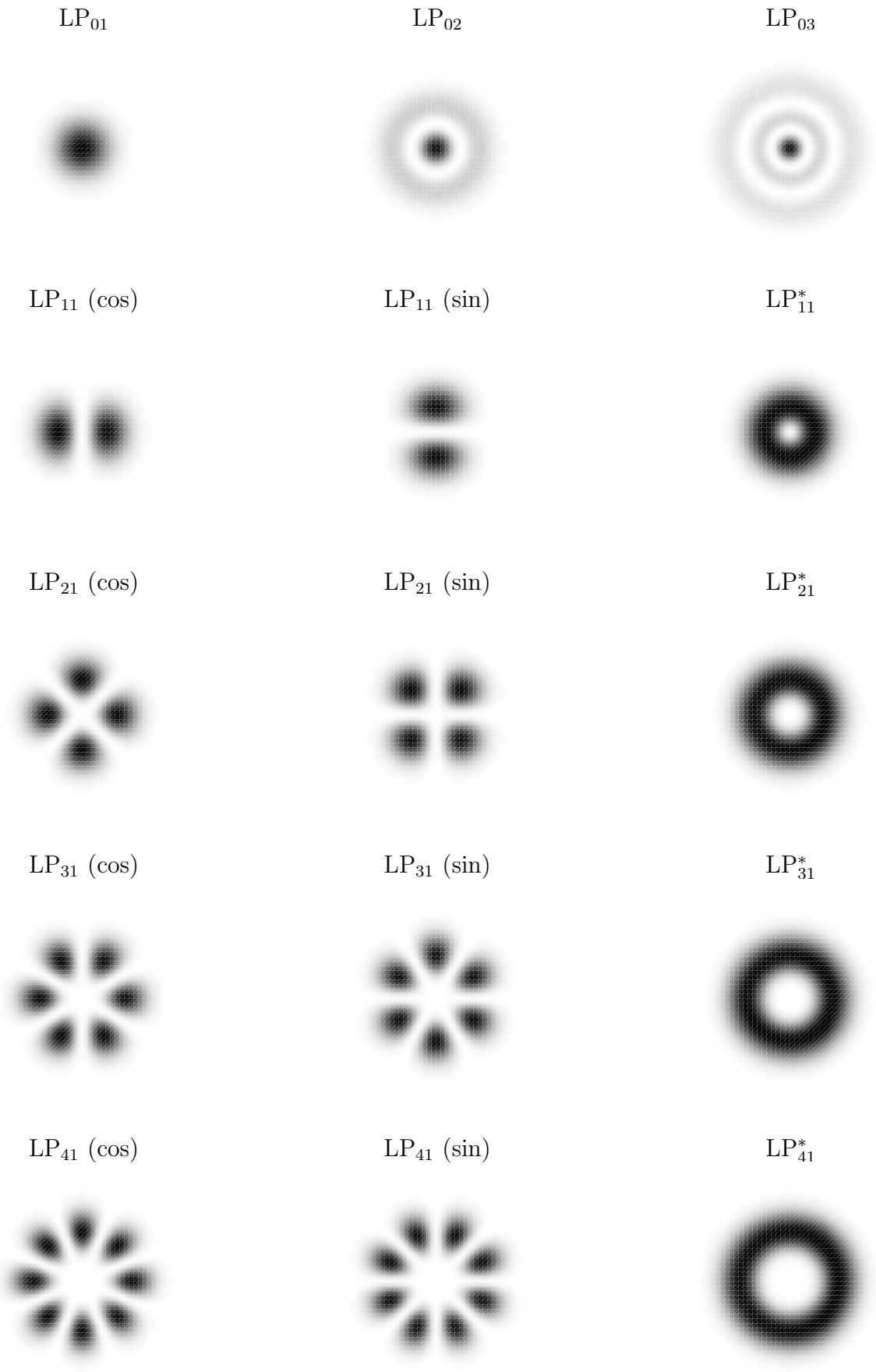


Fig. 3.4: *Calculated intensity distributions of LP_{lp} modes in cylindrical waveguides using (3.13).*

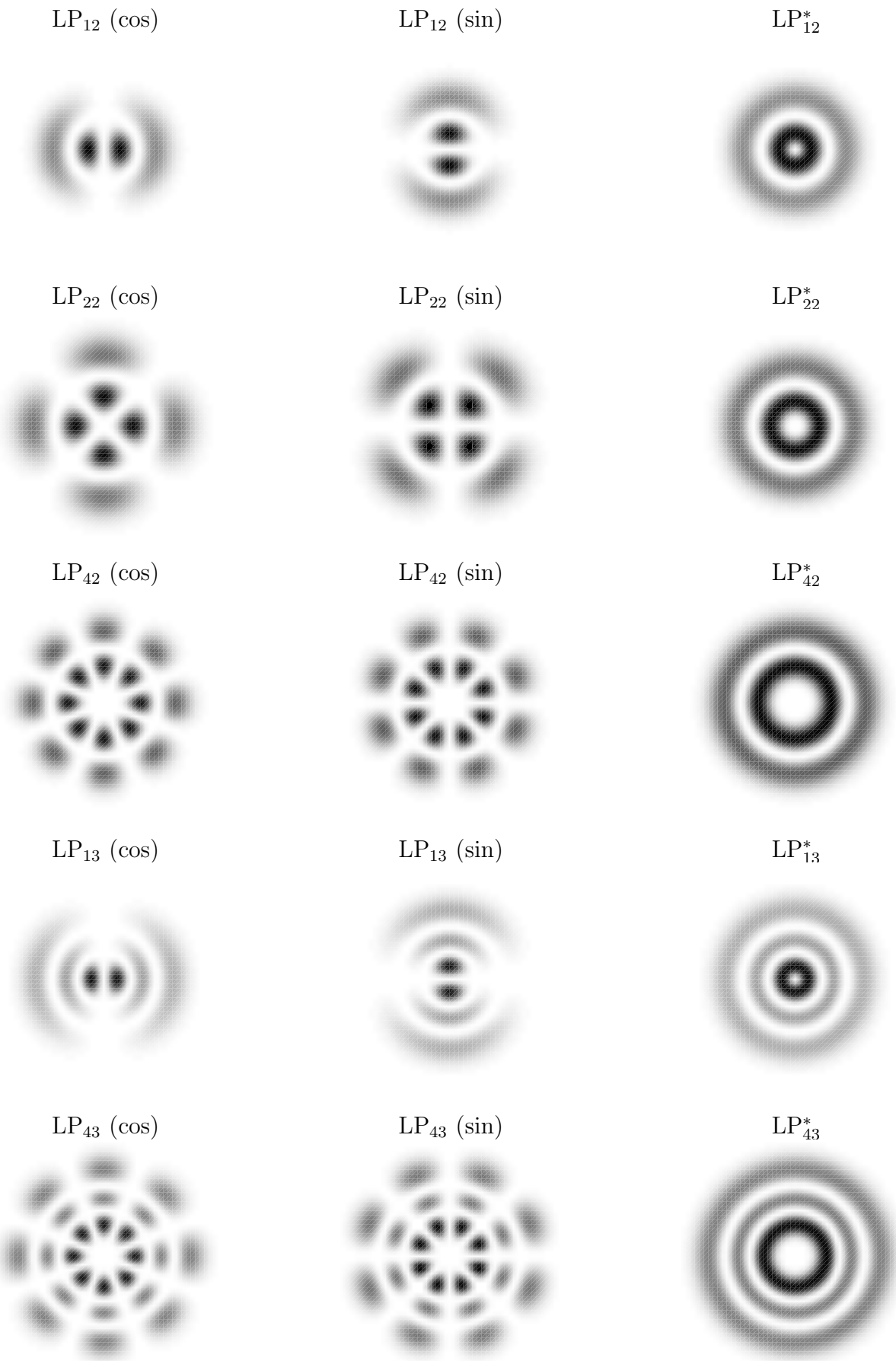


Fig.3.4: *Continued calculations of intensity distribution of LP_{lp} modes using (3.13).*

In larger size VCSELs several transverse modes may oscillate simultaneously. However, when the active diameter is typically kept below 10 μm for proton-implanted VCSELs or below 5 μm for oxidized VCSELs, fundamental transverse mode oscillation occurs. The total number of guided transverse modes of the structure can be estimated as [32]

$$M = \bar{V}^2/4 \tag{3.14}$$

for $M \gg 1$. The condition for transverse singlemode oscillation is generally written as

$$\bar{V} < 2.405 \cdot \sqrt{2} \quad , \tag{3.15}$$

which for weak lateral guiding $\bar{n}_{\mathrm{c}} \approx \bar{n}_{\mathrm{cl}}$ can be expressed as

$$\frac{2\pi a_{\mathrm{c}}\sqrt{\bar{n}_{\mathrm{c}}}}{\lambda}\sqrt{\bar{n}_{\mathrm{c}} - \bar{n}_{\mathrm{cl}}} < 2.405 \quad . \tag{3.16}$$

In this case the spatial variation $\Psi_0(r)$ is the fundamental-mode solution ($l = 0$) of the wave equation (3.4). Hence, its form normalized to unity according to (3.8) is

$$\Psi_0(r) = \exp\left\{-\frac{r^2}{w_0^2}\right\} \quad . \tag{3.17}$$

Concerning the spot size w_0 of the oscillating mode, 3.11 is valid for a parabolic index profile. In fact, there is an inherent relation between w_0 and the refractive index profile [33]. To find this relation for other profiles like step index for the case $l = 0$, (3.4) after multiplication by $r\Psi(r)$ has the form

$$r\Psi(r)\frac{d^2\Psi(r)}{dr^2} + \Psi(r)\frac{d\Psi(r)}{dr} + rk^2\bar{n}^2(r)\Psi^(r) - r\beta^2\Psi^2(r) = 0 \tag{3.18}$$

with $k = 2\pi/\lambda$. By using the identity

$$\frac{d}{dr}\left(r\Psi(r)\frac{d\Psi(r)}{dr}\right) = r\Psi(r)\frac{d^2\Psi(r)}{dr^2} + \Psi(r)\frac{d\Psi(r)}{dr} + r\left(\frac{d\Psi(r)}{dr}\right)^2 \quad , \tag{3.19}$$

the first two terms in (3.18) can be re-expressed as

$$\frac{d}{dr}\left(r\Psi(r)\frac{d\Psi(r)}{dr}\right) - r\left(\frac{d\Psi(r)}{dr}\right)^2 + rk^2\bar{n}^2(r)\Psi^2(r) - r\beta^2\Psi^2(r) = 0 \quad . \tag{3.20}$$

The integration of (3.20) from $r = 0$ to $r = \infty$ yields the stationary expression

$$\beta^2 = \frac{\int_0^\infty \left(k^2\bar{n}^2(r)\Psi^2(r) - (\frac{d\Psi(r)}{dr})^2\right) r dr}{\int_0^\infty r\Psi^2(r)dr} \quad , \tag{3.21}$$

where the first term in (3.20) vanishes at the integration limits. The refractive index profile in (3.6) can be re-expressed in the general form

$$\bar{n}^2(R) = \bar{n}_c^2\{1 - 2\Delta f(R)\} \quad , \tag{3.22}$$

where $f(R)$ defines the functional dependence of the refractive index profile over the normalized radius $R = r/a_c$. The spot size is determined by substituting (3.17) and (3.22) into (3.21) and by solving the equation

$$\frac{\partial \beta^2}{\partial w_0} = 0 \quad . \tag{3.23}$$

One obtains

$$\frac{1}{\bar{V}^2} = \int_0^\infty \frac{df(R)}{dR} R^2 \exp\left\{-\frac{2R^2}{R_0^2}\right\} dR \tag{3.24}$$

with the normalized spot size $R_0 = w_0/a_c$.
The e^{-2}-beam half-width w_0 of the fundamental approximative Gaussian mode of a step index profile is obtained by identifying

$$f(R) = \begin{cases} 0 & \text{for } 0 \le R < 1, \\ 1 & \text{for } 1 < R < \infty \end{cases} \tag{3.25}$$

and the derivative $df(R)/dR$ as the Dirac delta function $\delta(R-1)$. Substitution into (3.24) gives

$$\frac{1}{\bar{V}^2} = \int_0^\infty \delta(R-1) R^2 \exp\left\{-\frac{2R^2}{R_0^2}\right\} dR = \exp\left\{-\frac{2}{R_0^2}\right\} \quad , \tag{3.26}$$

and the spot size then is given as

$$w_0 = \frac{a_c}{\sqrt{\ln \bar{V}}} \quad . \tag{3.27}$$

3.1.3 Mode spacing of transverse modes

The propagation coefficient β of the LP_{lp} mode is obtained from the eigenvalue k_r in (3.5) which can be calculated by inserting (3.8) into (3.4) and using the full parabolic index profile. The result is

$$\begin{aligned} \beta &= \sqrt{4\pi^2 \bar{n}_c^2/\lambda^2 - 4\pi(2p + l - 1)\bar{n}_c\sqrt{2\Delta}/(a_c\lambda)} \\ &\approx \frac{2\pi \bar{n}_c}{\lambda}\left[1 - (2p + l - 1)\frac{\sqrt{\bar{n}_c - \bar{n}_{cl}}}{\sqrt{2}\pi \bar{n}_c^{3/2}}\frac{\lambda}{a_c}\right] \end{aligned} \tag{3.28}$$

For a one wavelength long inner cavity as in Fig. 2.6 the resonance condition is

$$\beta = \frac{2\pi}{L} \tag{3.29}$$

which determines the emission wavelength λ. For $\bar{n}_c = \bar{n}_{cl}$ the earlier result $\lambda = \bar{n_c} L = \lambda_B$ is reobtained. For $\bar{n}_c \neq \bar{n}_{cl}$ the emission wavelength of the LP_{lp} mode is

$$\lambda_{lp} = \lambda_B \left[1 - (2p + l - 1) \frac{\sqrt{\bar{n}_c - \bar{n}_{cl}}}{\sqrt{2\bar{n}_c}\pi} \frac{\lambda_B}{\bar{n}_c a_c} \right] \quad . \tag{3.30}$$

With increasing index $m = 2p+l-1$ the emission wavelength decreases. The fundamental mode $l = 0,\ p = 1$ has the longest emission wavelength. Modes with the same mode index m have the same emission wavelength. Including polarization the degenercy of modes with $l > 1$ is fourfold, and for $l = 0$ it is twofold. The mode spacing between modes LP_{lp} and $LP_{l^*p^*}$ is

$$|\lambda_{lp} - \lambda_{l^*p^*}| = |2(p^* - p) + l^* - l| \frac{\sqrt{\bar{n}_c - \bar{n}_{cl}}}{\sqrt{2\bar{n}_c}\pi} \frac{\lambda_B^2}{\bar{n}_c a_c} \quad . \tag{3.31}$$

In particular, the mode spacing between the fundamental LP_{01} mode and the next higher order LP_{11} mode is

$$\Delta\lambda = \lambda_{01} - \lambda_{11} = \frac{\sqrt{\bar{n}_c - \bar{n}_{cl}}}{\sqrt{2\bar{n}_c}\pi} \frac{\lambda_B^2}{\bar{n}_c a_c} \approx \frac{\sqrt{\Delta_n}}{\sqrt{2\bar{n}_c}\pi} \frac{\lambda_B^2}{\bar{n}_c a_c} \tag{3.32}$$

and the mode spacing of any other two modes is an integer multiple of this figure. From this equation it is clear that the mode spacing is inversely proportional to the active radius a_c of VCSEL and directly proportional to the emission wavelength squared and to the square root of the induced index step Δ_n.

3.1.4 Propagation of Gaussian beams

In the near-field, a coherent light beam generated by a VCSEL can be assumed to have a Gaussian field as described by (3.17) with $r^2 = x^2 + y^2$. This beam has its minimum diameter $2w_0$ at the beam waist at $z = 0$ where the phase front is plane. In order to find out how this field distribution evolves as it propagates along z-axis as in the coordinate system in the left part of Fig. 3.5, one uses the Kirchhoff-Huygens diffraction integral in its frensel approximation [34]

$$\Psi(x', y', z) = \frac{i}{\lambda z} \int\int_{-\infty}^{+\infty} \Psi(x, y, 0) \exp\left\{ -i \frac{k}{2z} \left[(x' - x)^2 + (y' - y)^2 \right] \right\} dxdy \quad . \tag{3.33}$$

By inserting (3.17) into (3.33) one obtains the normalized field at any given distance z in the form

$$\Psi(x', y', z) \propto \frac{1}{\sqrt{w(z)}} \cdot \exp\left[-ikz + i\phi(z) \right] \cdot \exp\left[-\frac{r'^2}{w^2(z)} - ik \frac{r'^2}{2R(z)} \right], \tag{3.34}$$

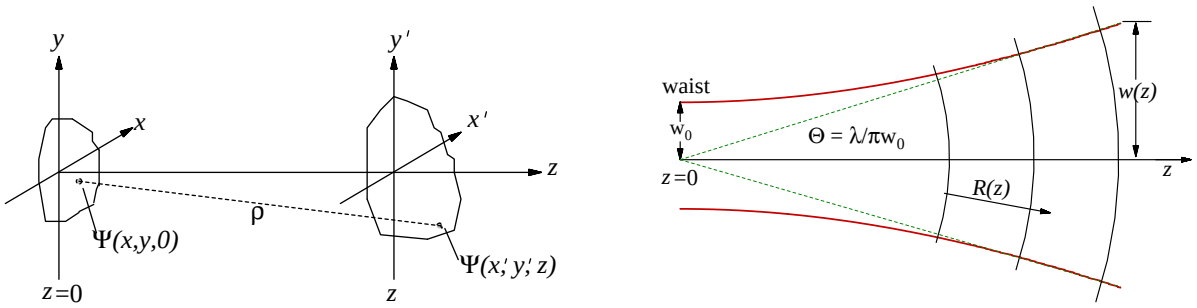


Fig. 3.5: *Coordinate system for integral (3.33), where* $\rho = \sqrt{(x'-x)^2 + (y'-y)^2 + z^2}$ *(left) and amplitude contours as well as phase front of a Gaussian beam (right).*

where $r'^2 = x'^2 + y'^2$ and the beam width $w(z)$, the wavefront radius of curvature $R(z)$ and the phase variation $\phi(z)$ are defined, respectively, as

$$w(z) = w_0\sqrt{1+\left(\frac{z}{z_R}\right)^2} \quad , \tag{3.35}$$

$$R(z) = z + \frac{z_R^2}{z} \quad , \tag{3.36}$$

$$\phi(z) = \tan^{-1}\left(\frac{z}{z_R}\right) \tag{3.37}$$

with the Rayleigh distance of the Gaussian beam $z_R = \pi\bar{n}_0 w_0^2/\lambda$ in a homogeneous medium with refractive index $\bar{n}$. The right part of Fig. 3.5 shows the expansion of the beam width according to (3.35). The beam contour $w(z)$ is a hyperbola with asymptotes inclined to the axis at an angle

$$\Theta = \lim_{z\to\infty}\frac{w(z)}{z} = \frac{\lambda}{\pi\bar{n}_0 w_0} \quad . \tag{3.38}$$

This is the far-field diffraction angle of the fundamental mode. Now one can write the far field intensity profile $I(\theta)$ for $z \gg z_R$

$$I(\theta) = \Psi(r',z)\cdot\Psi^*(r',z) \propto \frac{1}{w(z)}\exp\left\{-2\left(\frac{\pi\bar{n}_0 w_0\tan(\theta)}{\lambda}\right)^2\right\} \quad , \tag{3.39}$$

where $\tan(\theta) = r'/z$. In this manner, the intensity of a Gaussian beam can be tranformed from the near-field into the far-field.

3.2 Experiment and Discussion

3.2.1 Device output characteristics

An optical power meter[1] is employed to measure the optical power emitted from the VCSEL. This power meter is placed under slightly tilted angle in front of the VCSEL to avoid multiple light reflections which might cause measurement errors. The optical signal is converted to a correspondig electrical signal by the power meter and then digitized with an analog-to-digital (A/D) converter. Figure 3.6(a) depicts the continuous wave (cw) output characteristics of two devices from sample M108/97 with different active diameters D_a. It is seen that the small device has 0.9 mA threshold current while this value is increased by increasing the active diameter. Also, with increasing pump current a typical rollover of the output power is seen due to internal heating, mainly giving rise to carrier and current leakage. In Fig. 3.6(b), the characteristics of two different devices from sample M46/97 in cw operation are shown. It is obvious that these devices have significantly increased threshold currents in comparison with identical diameter lasers of the aforementioned sample. Most probably this is due to the presence of the oxide layer in the third mirror pair above the active layer in this sample as shown in Fig. 3.2(a) and as a result the current leakage is increased.

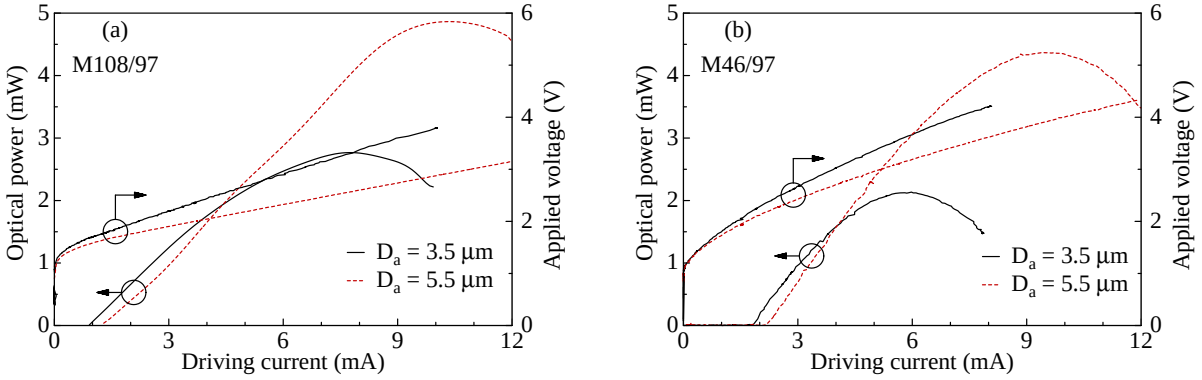


Fig. 3.6: *Output power and current-voltage characteristics for VCSELs with active diameters of 3.5 and 5.5 µm from sample M108/97 (a) and sample M46/97 (b).*

Concerning the spectrum of the emitted light, the VCSEL output is collimated with an aspheric collimating lens and coupled into a graded-Index multimode optical fiber with 50 μm core diameter. This fiber is then connected to an optical spectrum analyzer[2] with

[1] Advantest, TQ8210

[2] Anritsu Optical Spectrum Analyser MS 9001 B1

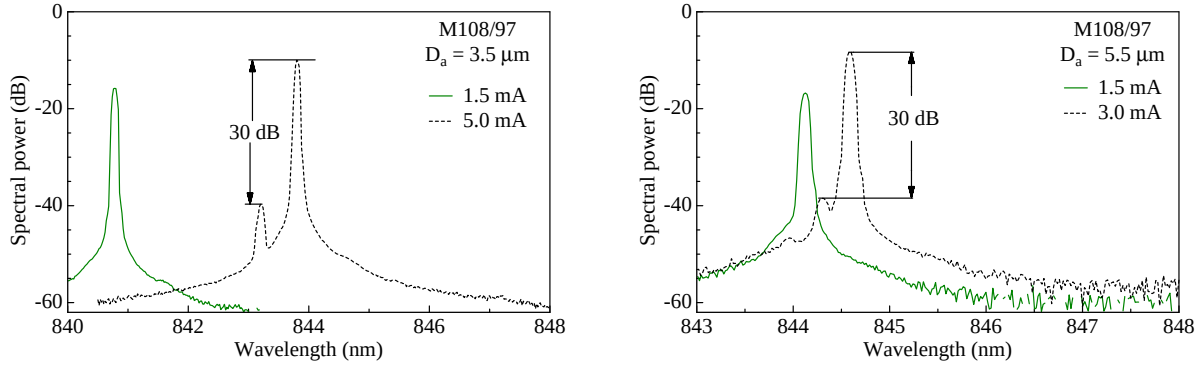


Fig. 3.7: *Emission spectra at various driving current defined by the legends for a* 3.5 μm *(left) and* 5.5 μm *(right) diameter selectively oxdized VCSELs from sample M108/97.*

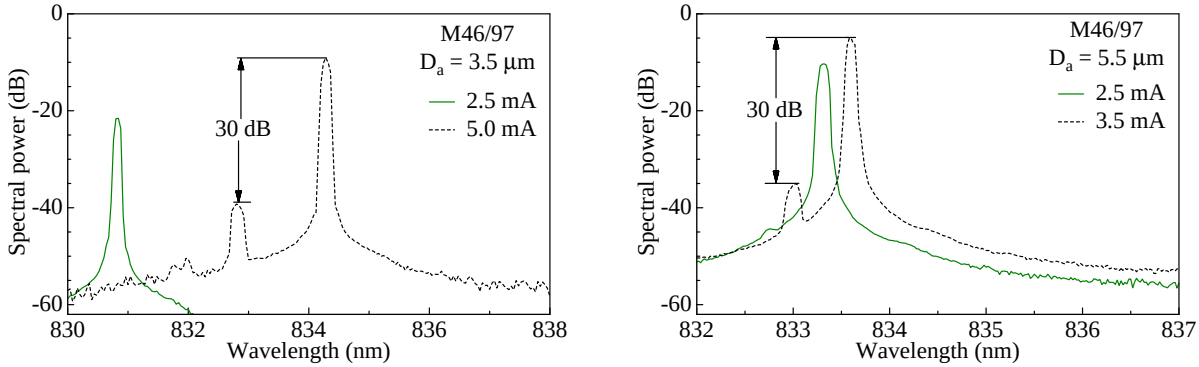


Fig. 3.8: *The same as Fig. 3.7, but for a* 3.5 μm *(left) and* 5.5 μm *(right) diameter selectively oxdized VCSELs from sample M46/97.*

a maximum wavelength resolution of 0.1 nm. Figure 3.7 illustrates the oscillation of the two different VCSELs of Fig. 3.6(a) on a single mode up to 5 mA current for the small device and up to 3 mA for the larger one. The single-mode emission limit is defined here through a side-mode suppression ratio (SMSR) of 30 dB. It is seen from these spectra that the transverse mode spacing $\Delta\lambda$ is decreased by increasing the active diameter as to be expected from (3.32). In addition, the resonance wavelength shows a red-shift with increasing current. This shift is mainly governed by the temperature gradient of mean refractive index in the resonator. In Fig. 3.8 the emission spectra of the VCSELs from Fig. 3.6(b) are depicted.

3.2.2 Near-field analysis

To analyze the spatial profiles of the lasing modes, near-field measurements are carried out based on a fiber tip scanning technique. The setup is shown in Fig. 3.9 and consists mainly

of a high precision 3-axes piezoelectrically driven stage[3] and digital control electronics. Within the travel range of 100 μm for each of the three directions, the spatial resolution is better than 50 nm [35]. The optical output power from the VCSEL is launched into a 2 m long single-mode optical fiber [36] whose tip has a semi-spherical lens shape with radius of curvature $R = 6\,\mu$m [36]. A multi-wavelength meter[4] is employed to detect the frequency-resolved laser input signal with a sensitivity, frequency resolution, and absolute accuracy in the order of -25 dBm, 20 GHz, and ± 3 ppm, respectively, for the wavelength range of interest [37]. Finally these data can be collected with the help of a PC program.

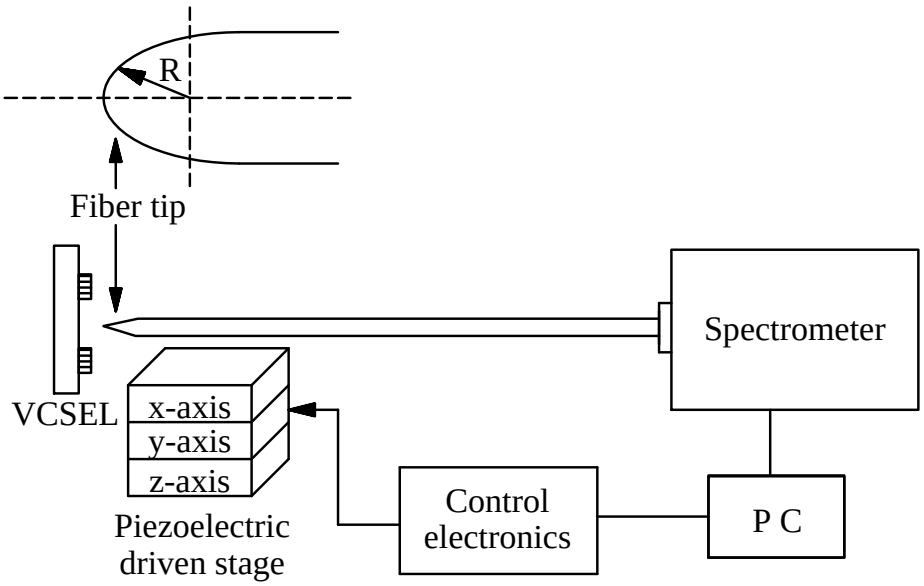


Fig. 3.9: *Near-field measurement setup.*

The principle of the fiber tip scanning technique is illustrated in the left part of Fig. 3.10. The sample is positioned in front of the fiber tip such that the fiber-coupled optical power is maximized when the distance to the beam waist equals the focal length [38] $f = R/(\bar{n} - 1) \approx 12\,\mu$m for the above fiber with refractive index $\bar{n} = 1.5$. When the fiber tip moves from an arbitrary central position z_0 towards the VCSEL along the z-axis, the coupled power into the fiber increases from P_0 to P. The increase of the coupled power η_{inc} is defined as

$$\eta_{\text{inc}} = \frac{P - P_0}{P_0} \quad . \tag{3.40}$$

The right part of Fig. 3.10 shows measured data η_{inc} at different fiber positions relative to the beam waist for a 3.5 μm active diameter single-mode VCSEL of sample M108/97

[3] Physik Instrumente Digital Piezoelectric Positioning System P-762.00/P-925.272
[4] Hewlett Packard, Multi-Wavelength Meter 86120A

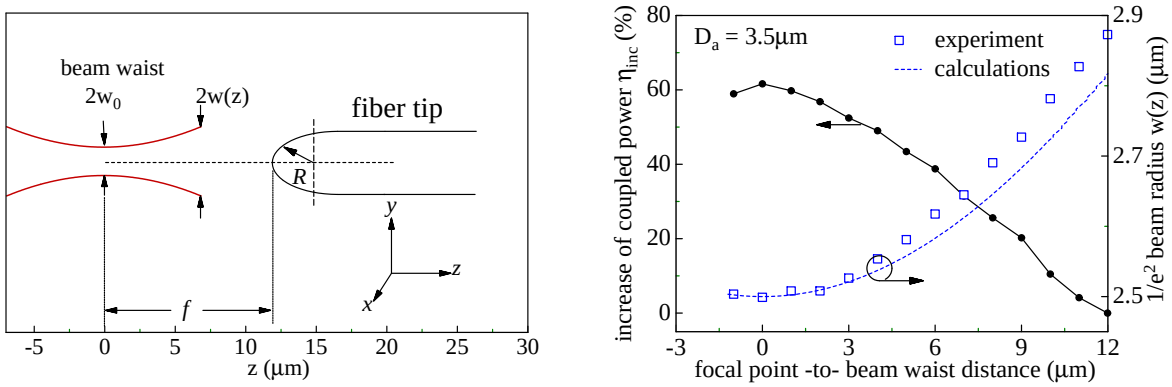


Fig. 3.10: *Schematic of operation principle of the fiber tip scanning system (left), measured increase of the coupled power into the fiber η_{inc}, and measured contour radius $w(z)$ (open squares) of a VCSEL fundamental mode compared with calculations for a Gaussian beam (dashed curve) using (3.35) (right).*

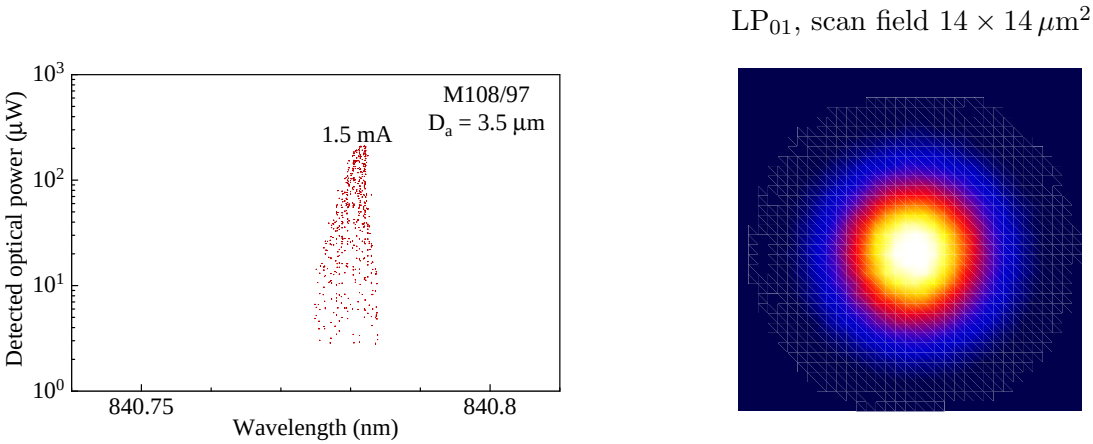


Fig. 3.11: *Measured spectrum of a 3.5 µm active diameter VCSEL from sample M108/97 at 1.5 mA current using the near-field setup (left). Intensity distribution of the oscillating LP_{01} mode (right).*

at 1.5 mA bias. At each longitudinal position, the fiber is moved laterally in x- or y-direction to locate the intensity drop by $1/e^2$ and thus identify the beam radius w. It becomes clear that the calculated beam radius using (3.35) is in good agreement with the observed data which indicates the close similarity of the VCSEL LP_{01} mode to a Gaussian beam. Moreover, when the focal point of the fiber tip coincides with the beam waist, the power coupled into the fiber is maximum. Having adjusted the fiber at this position, a BASIC program is employed to control its position in the desired 2-dimensional scan field of the oscillating mode. Results obtained with this system are described in Fig. 3.11. The left part shows the peak laser spectrum for every point in the scan field at 1.5 mA. In total, it looks like a line spectrum with some broadening of about 6 pm which lies nearly

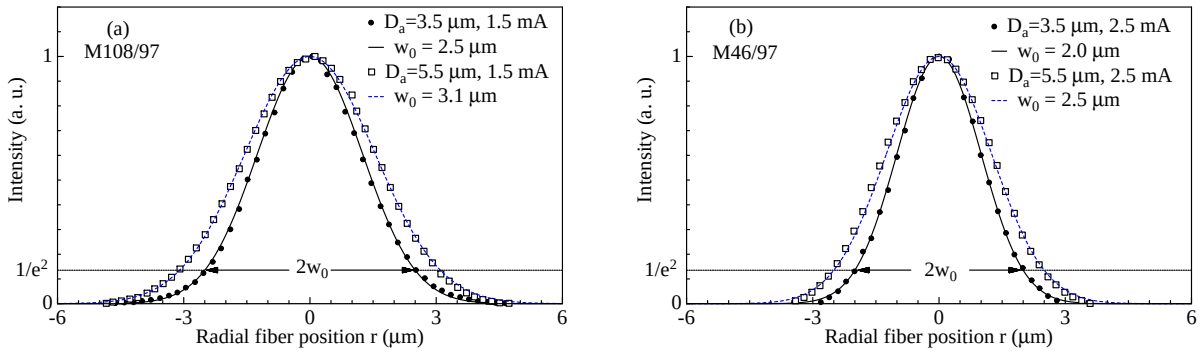


Fig. 3.12: *(a) Measured near-field intensity distributions for VCSELs of sample M108/97 with 3.5 (solid circles) and 5.5 µm (open squares) active diameters at 1.5 mA and fits to Gaussian profiles (dashed and solid curves) with the mode radii w_0 given in the legend. (b) The same measurements as in (a) for VCSELs of sample M46/97 with 3.5 (solid circles) and 5.5 µm active diameters at 2.5 mA, respectively and fits to Gaussian profiles (dashed and solid curves).*

in the range of the absolute accuracy of the multi-wavelength meter where the latter is ±3 ppm (part per milion) which means ±2.55 pm for 850 nm wavelength. Moreover, it is similar to that of the left part of Fig. 3.7, but this system is insensitive for signals of power < -25 dBm. The right part of Fig. 3.11 shows the 2-dimensional intensity distribution of that mode. It is seen that the mode is circularly symmetric, has its intensity mamimum in the center and from Fig. 3.4 has thus to be denoted as LP_{01}. In order to find the spot size w_0 of the oscillating mode, it is convenient to cut a transverse line from the center of the image and fit it to a Gaussian profile according to (3.17). Figure 3.12(a) summarizes the measured near-field intensity profiles for 3.5 µm and 5.5 µm aperture VCSELs of sample M108/97 at 1.5 mA driving current fitted to Gaussian profiles with e^{-2}-beam half-width w_0 of 2.5 and 3.1 µm, respectively. The same measurements are shown in Fig. 3.12(b), but in this case for 3.5 µm and 5.5 µm aperture VCSELs of sample M46/97 at 2.5 mA driving current fitted to Gaussian profiles with w_0 of 2.0 and 2.5 µm, respectively. It is clear from these measurements that the fundamental mode of VCSEL is well described by a Gaussian profile and its spot size increases for larger active areas. In fact, the measured Gaussian profile of spot size w_m is related to that of the laser w_0 and fiber w_f by

$$w_m^2 = w_0^2 + w_f^2 \tag{3.41}$$

taking convolution effects of the finite spot size w_f of the focussed fiber beam into account. The plot of w_0 and the relative difference $(w_m - w_0)/w_m$ as a function of w_m is depicted in Fig. 3.13 with $w_f = 0.75\,\mu$m [39] . As can be seen, $(w_m - w_0)/w_m$ has large values for $0.75 < w_m < 2.0\,\mu$m wheras it is reduced significantly for larger values. As an approximation, measured values of $w_m \geq 2.0\,\mu$m can be considered to be equal to w_0 since the relative difference in between is less than 7 %.

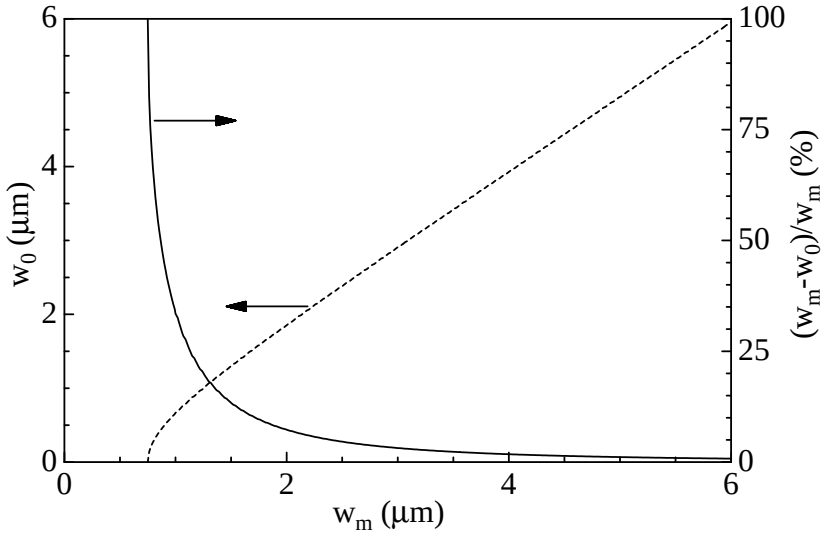


Fig. 3.13: *Calculated laser spot size w_0 from (3.41) for different values of w_m and the relative difference in between.*

3.2.3 Far-field analysis

In Fig. 3.14 the far-field measurement setup is depicted. It consists of a Si-photodiode[5] (PD) mounted on the free end of an arm with the VCSEL sitting underneath its center of rotation. Potentiometer is employed to measure the rotation angle of the arm. The output analog signals from both the detector and the potentiometer are translated to digital ones using A/D converter. Finally, the data are collected with a PC program. By adjusting the height of the PD for maximum light intensity emanating from the VCSEL and arm rotation up to 180^o the far field intensity distribution of the oscillating mode is obtained. Especially, as outlined theoretically in Sect. 3.1.4) a Gaussian profile is invariant to transformation between near- and far-fields. Figures 3.14 (a) and (b) represent the measured far-field intensity distributions for the two cases considered in Fig. 3.12 including the corresponding transformations of the Gaussian profiles (3.39) (dashed and solid curves). It becomes apparent that the Gaussian profiles fit the measured data very well. In addition, the formula (3.38) for calculating the e^{-2}-beam divergence half-angle Θ reproduces the measured data for all lasers.

As can be seen, the spot sizes of the devices belonging to sample M46/97 are smaller than those of sample M108/97 although the lasers have the same active diameter. This indicates the presence of stronger optical confinement in sample M46/97. Other data cofirming this result are the mode spacings $\Delta\lambda_m$ between the fundamental LP_{01} mode and the next higher order LP_{11} mode which for sample M108/97 are smaller than for

[5]Optical Silicon Integrated Detector OSI5-10M/10K

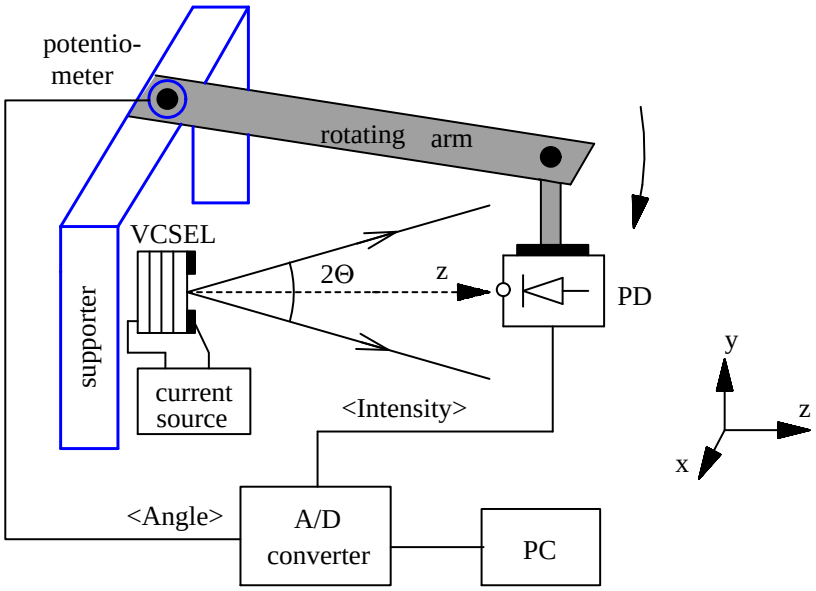


Fig. 3.14: *Far-field measurement setup.*

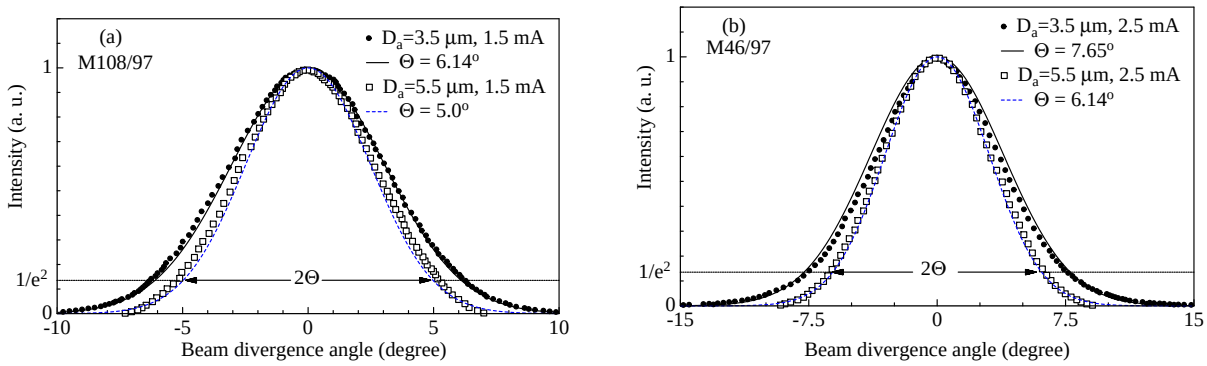


Fig. 3.15: *(a) Measured far-field intensity distributions for the same case as in Fig. 3.12(a) compared with the calculations using (3.39) (dashed and solid curves) with their respective values of* Θ*. (b) Measurements and calculations as in (a) for the same case as in Fig. 3.12(b).*

M46/97, as can be seen in the spectra of Figs. 3.7 and 3.8 and as can be estimated from (3.32). To understand the underlying reason, the built-in effective index step Δ_n can be defined as a linear combination of all induced indices as [40]

$$\Delta_n = \Delta\bar{n}_{ox} + \Delta\bar{n}_{fc} + \Delta\bar{n}_t \quad . \tag{3.42}$$

The first term represents the effective refractive index induced by the oxide aperture and is defined in (3.1). For sample M46/97 its value is $5 \cdot 10^{-3}$ which is five times larger than for sample M108/97, as can be seen in Fig 3.2(a). The second term is the free carrier induced index which can be set to a value [41] of -10^{-3} which is taken constant due

Tab. 3.1: *Measured spot size w_0, divergence far-field angle Θ, and mode spacing $\Delta\lambda_m$ for VCSELs with different active diameters D_a from samples M108/97 and M46/97. The mode spacing $\Delta\lambda_c$ is calculated for the induced index Δ_n of the two samples.*

	sample M108/97					sample M46/97				
D_a (μm)	w_0 (μm)	Θ ($^\mathrm{o}$)	Δ_n	$\Delta\lambda_c$ (nm)	$\Delta\lambda_m$ (nm)	w_0 (μm)	Θ ($^\mathrm{o}$)	Δ_n	$\Delta\lambda_c$ (nm)	$\Delta\lambda_m$ (nm)
3.5	2.5	6.14	$3.3 \cdot 10^{-3}$	0.82	0.61	2.0	7.65	$8.2 \cdot 10^{-3}$	1.34	1.45
5.5	3.1	5.0	$1.4 \cdot 10^{-3}$	0.35	0.31	2.5	6.14	$6.2 \cdot 10^{-3}$	0.72	0.58

to carrier clamping at laser threshold. The last term stands for the thermally induced refractive index change which is defined as

$$\Delta\bar{n}_\mathrm{t} = \frac{\partial\bar{n}}{\partial T}\,\Delta T \quad , \tag{3.43}$$

where $\partial\bar{n}/\partial T \approx 4\cdot10^{-4}\,\mathrm{K}^{-1}$. The temperature difference between the center and the edge of the active region ΔT can be obtained as [41]

$$\Delta T = \frac{Q}{2\pi\sigma} \tag{3.44}$$

with $Q = P_{abs}/d_\mathrm{eff}$ as the heat generation per unit distance along the symmetry axis of the VCSEL, where the absorbed power P_{abs} is the difference between the electrical input and optical output power, $d_\mathrm{eff} \approx 5\,\mu$m is the effective thickness of layers contributing to heat generation, and $\sigma = 0.44$ W/(K cm) is the thermal conductivity of GaAs.
For sample M108/97, $\Delta\bar{n}_\mathrm{t}$ is calculated at 5 and 3 mA currents for the 3.5 and 5.5 μm aperture devices, respectively, whereas for sample M46/97 it is calculated at 5 and 3.5 mA currents for the 3.5 and 5.5 μm diameter VCSELs, respectively. Table 3.1 summarizes the measured spot size w_0, far-field divergence angle Θ, and the mode spacing $\Delta\lambda_m$ for the devices under investigation. Also, this table includes the calculated total induced index step Δ_n and the mode spacing $\Delta\lambda_c$. As shown in this table, the devices from sample M46/97 have larger Δ_n than those from sample M108/97, and consequently the former experience stronger optical confinement than the latter. In addition, the calculated mode spacings $\Delta\lambda_c$ using (3.32) are in good agreement with the observed ones.

Chapter 4

Long Monolithic Cavity VCSELs

In recent years, there has been extensive interest in large area single-mode VCSELs of low electrical resistance which are especially attractive for high-speed optical data communications and array applications. To date, conventional single-mode VCSELs with the largest lateral dimensions use proton-implanted designs. Although selectivity oxidized VCSELs offer much improved electrical and optical properties, the increased optical guiding due to the presence of the oxide layer requires much smaller active diameters to keep the frequency parameter $\bar{V}$ in the single-mode regime. To increase the active area in single mode operation, an approach based on a long monolithic cavity has resulted in single-mode devices with far-field divergence angles of only 1.6° (e^{-2}-beam half-angle) for a 30 μm aperture diameter [42]. In recent work [43], the incorporation of a lightly n-doped GaAs spacer of thickness $L_s = 4\,\mu$m directly underneath the active region of a 7 μm aperture device has led to single-mode VCSELs with output power of 5 mW under continuous wave (cw) operation. With this kind of device, we have observed for the first time longitudinal mode switching in a VCSEL using 2 and 8 μm cavity spacers. This chapter presents a more detailed investigation of the experimentally observed longitudinal mode structure in these devices. In addition, the transverse mode structure of the 4 μm spacer devices will be compared with those of the 0 μm spacer where in both two cases only one longitudinal mode oscillates.

4.1 Switching Between Longitudinal Modes

This section presents simulations based on transfer matrix method for VCSELs with a long monolithic cavity to show how the number of longitudinal modes increases by increasing the cavity length. In addition, these simulations are compared with the observed spectra and near-far field measurements to explain the switching phenomena between longitudinal modes.

4.1.1 Device structure and simulations

The selectively oxidized VCSEL structures for this work are grown using solid-source molecular beam epitaxy (MBE). The standard 980 nm VCSEL structure is depicted in

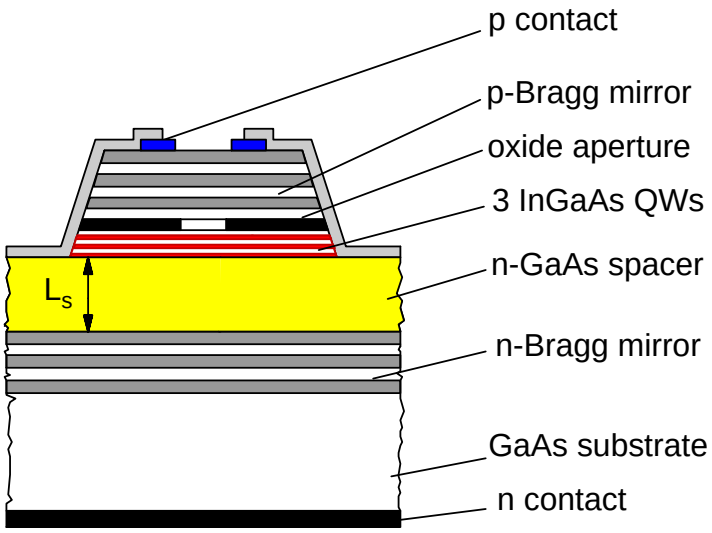


Fig. 4.1: *General VCSEL structure with long monolithic cavity*

table A.3 in Appendix A. It consists of a 40.5-pair n-doped $Al_{0.93}Ga_{0.07}As$/GaAs Bragg mirror, three 8 nm $In_{0.19}Ga_{0.81}As$ quantum wells, 30 nm AlAs-aperture layer in the p-mirror pair closest to the active region and an 18-pair p-doped $Al_{0.93}Ga_{0.07}As$/GaAs Bragg mirror. To increase the cavity length, a lightly n-doped GaAs spacer is added underneath the active region as shown in Fig. 4.1. A series of 2, 4 and 8 μm spacer lengths are fabricated for samples M17/99, M67/99, and M80/99, respectively. From a theoretical point of view, based on the transfer matrix method, it is found that the number of longitudinal modes is increased by increasing the cavity length, as illustrated by the reflectivity spectra (dashed curves) in Figs. 4.2(a)-4.2(c) for 2, 4 and 8 μm spacers, respectively. We also see that a central mode $LP_{01}^{(0)}$ in the two cases of 2 and 8 μm spacers is present, while in case of 4 μm it is absent due to a slightly too thick inner cavity. The curves in the lower part of these figures illustrate the observed emission spectra of 4, 7 and 8 μm aperture devices, respectively. These observed spectra show the switching between two longitudinal modes except in case of $L_s = 4\,\mu$m where lasing on the same longitudinal mode is observed over the whole current range. The mode separations of these observed modes are in good agreement with the values obtained from the calculations. The calculated standing wave patterns of the optical fields are depicted in Fig. 4.3 for the case of Fig. 4.2(a). It is seen that the resonator is designed such that the oxide layer Al_xO_y is centered at a node of the $LP_{01}^{(0)}$ optical field while it is shifted from the node of the $LP_{01}^{(\pm1)}$ fields and as a result,

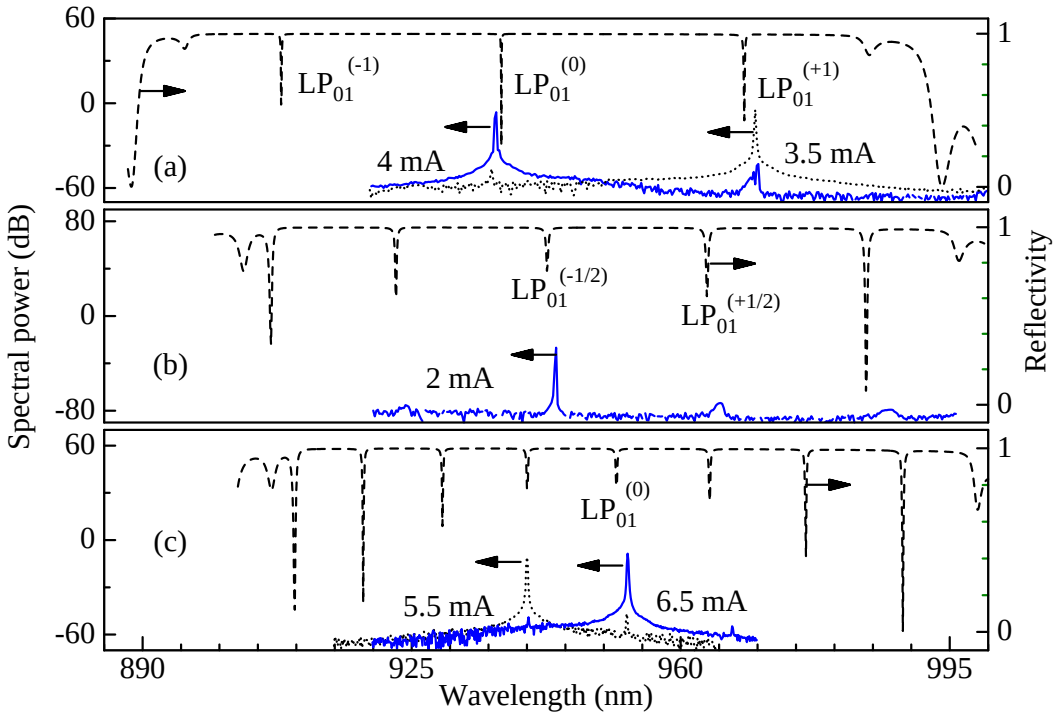


Fig. 4.2: *Calculated reflectivity spectra (dashed curves) of VCSEL structures with (a) $L_s = 2\,\mu m$ and measured spectra at 3.5 mA (dotted curve) and 4 mA (solid curve) for a $D_a = 4\,\mu m$ active diameter device (b) $L_s = 4\,\mu m$ and spectrum at 2 mA (solid curve) for $D_a = 7\,\mu m$ (c) $L_s = 8\,\mu m$ and spectra at 5.5 mA (dotted curve) and 6.5 mA (solid curve) for $D_a = 8\,\mu m$.*

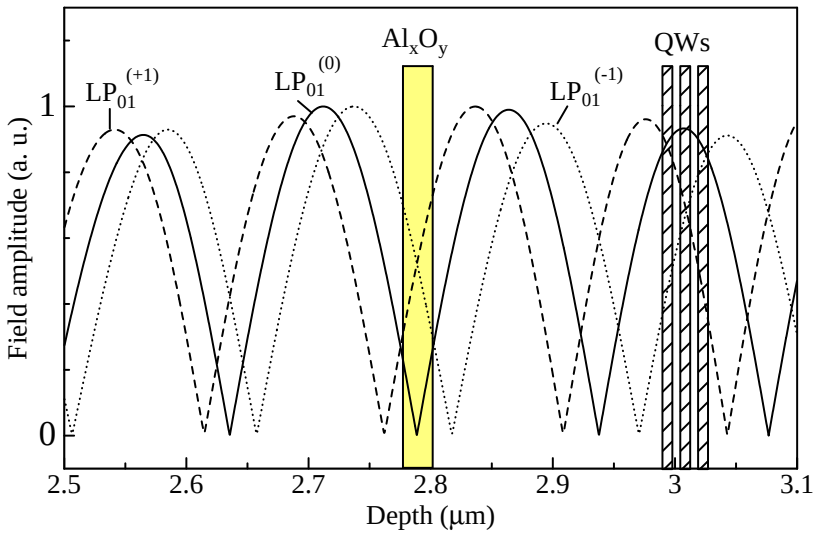


Fig. 4.3: *Resonant standing wave patterns corresponding to the fundamental and the neighboring order longitudinal modes for the VCSEL structure of Fig. 2(a).*

the latter experience much stronger index guiding. Although the one-dimensional calculations show that the central mode $LP_{01}^{(0)}$ in case of 2 and 8 μm spacers has a lower threshold gain than the $LP_{01}^{(\pm1)}$ modes, the latter start oscillating first because they are more strongly index guided and thus have a higher lateral confinement factor associated with lower losses. At higher driving currents, thermal lensing reduces the mode diameter so that the central mode is finally excited. The importance of thermal lensing as an aid to excite a weakly guided mode is also pointed out in [41]. In case of $L_s = 4\,\mu$m the situation is different. The optical fields of the modes labeled as $LP_{01}^{(\pm1/2)}$ have the same overlap with the oxide layer and thus simply the longitudinal mode positioned closer to the center of the stop-band is dominating over the whole current range.

4.1.2 Output characteristics

Figure 4.4 shows light output characteristics for the VCSELs of Fig. 4.2. Emission is in the Gaussian-like fundamental transverse mode up to 7 mA for the device with $L_s = 2\,\mu$m, 9 mA for the 4 μm spacer, and 12 mA for longest VCSEL, corresponding to 3.4, 5.0 and 5.5 mW maximum output powers. It is seen that the output power of the 2 μm spacer device exhibits a dip at 4 mA where switching between the $LP_{01}^{(+1)}$ and $LP_{01}^{(0)}$ modes takes place, as illustrated also by the spectra in Fig. 4.2(a). The 8 μm spacer device has a similar output power dip at 6 mA but in this case switching between the $LP_{01}^{(-1)}$ and $LP_{01}^{(0)}$ modes is observed, as illustrated by the spectra in Fig. 4.2(c). The output curve of the 4 μm spacer device shows no dip because there exists only a single longitudinal mode.

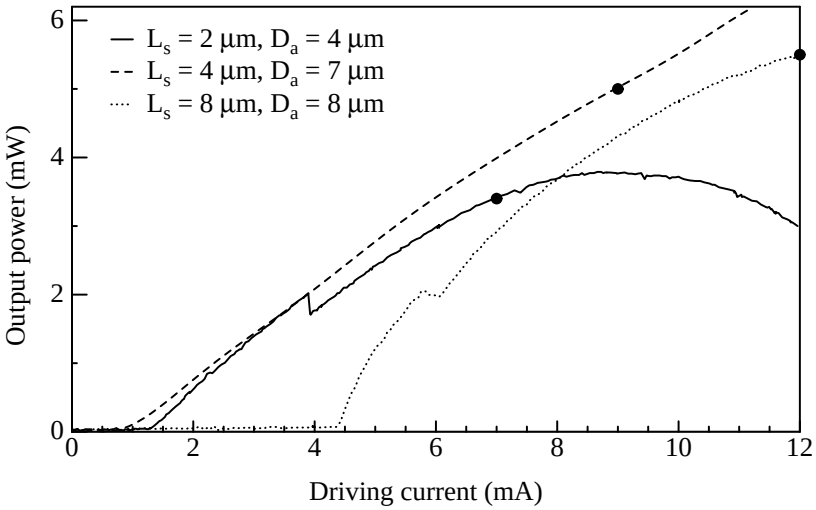


Fig. 4.4: *Light output characteristics for VCSELs with different spacer thickness L_s and active diameters D_a from Fig. 4.2. Dots indicate the onset of higher order transverse modes, i.e. the decrease of sidemode suppression ratio below 30 dB.*

4.1.3 Near-and far-field analyses

To analyze the spatial profiles of the lasing modes, the near-field measurement setup described in Chapter 3 is used. Figure 4.5(a) shows the measured near-field intensity profiles for the 4 μm aperture device with 2 μm spacer at 3.5 mA and 4 mA current, fitted to Gaussian profiles with e^{-2}-beam half-width w_0 of 2.55 μm and 3 μm, respectively. Figure 4.5(b) shows the same measurements for the 8 μm aperture device with 8 μm spacer at 5.5 mA and 6 mA fitted to Gaussian profiles with $w_0 = 4.25\,\mu$m (not drawn) and 4.4 μm, respectively. Figures 4.5(c) and (d) represent the measured far-field distributions around the switching point for the two cases considered including the corresponding Fourier transformations of the Gaussian profiles. It becomes apparent that the Gaussian fits represent the measured data very well. The determined e^{-2}-beam half-widths w_0 versus cw driving current for single transverse mode operation are summarized in Fig. 4.6(a). The open squares represent the data for a VCSEL with $\mathrm{D}_a = 4\,\mu$m and spacer length $\mathrm{L}_s = 2\,\mu$m and show a sudden increase of w_0 at 4 mA at which switching between the $\mathrm{LP}_{01}^{(+1)}$ and $\mathrm{LP}_{01}^{(0)}$ modes occurs. This means that the $\mathrm{LP}_{01}^{(+1)}$ mode experiences much stronger index guiding than the $\mathrm{LP}_{01}^{(0)}$ mode, in accordance with Fig. 4.3. The open circles illustrate the same effect for a VCSEL with $\mathrm{D}_a = 8\,\mu$m and $\mathrm{L}_s = 8\,\mu$m but in this case switching takes place between the $\mathrm{LP}_{01}^{(-1)}$ and $\mathrm{LP}_{01}^{(0)}$ modes. The open triangles stand for the VCSEL with $\mathrm{D}_a = 7\,\mu$m and $\mathrm{L}_s = 4\,\mu$m. Figure 4.6(b) represents the e^{-2}-beam half-angle θ from the independent far-field measurements for the three cases considered. As expected, the sudden increases of the beam half-widths in the near-fields translate into decreases of far-field angles at the switching points.

To understand the measurements theoretically, (3.42) is used to determine the total induced index difference Δ_n. For simplicity, the free carrier induced index $\Delta\bar{n}_\mathrm{fc}$ is set to a free parameter for each device to fit the measured near-field data with theoretical ones. The total induced index difference Δ_n is calculated for the three cases under investigation with the optimum value of $\Delta\bar{n}_\mathrm{fc}$ and is plotted versus pumping current in Fig. 4.6(c). In case of the 2 μm spacer we get $\Delta\bar{n}_\mathrm{fc} = -10^{-3}$ and the solid curve shows a large discontinuity in Δ_n at 4 mA because the $\mathrm{LP}_{01}^{(+1)}$ mode experiences an oxide index step of about $\Delta\bar{n}_\mathrm{ox} = 3\cdot 10^{-3}$ which is nearly ten times that of the $\mathrm{LP}_{01}^{(0)}$ mode. Therefore oxide-guiding is dominant for the $\mathrm{LP}_{01}^{(+1)}$ and the index profile is well approximated by a step function. This in turn results in w_0 described by (3.27) which agrees well with the measured values, as illustrated by the thin dashed curve in Fig. 4.6(a). Using (3.11) fails in reproducing these data as seen from the thick dashed curve in the same figure. For the weakly confined $\mathrm{LP}_{01}^{(0)}$ mode the situation is different since at 4 mA the induced thermal lensing $\Delta\bar{n}_\mathrm{t}$ is dominant and the index profile is approximated well by a parabolic profile. (3.11) nicely fits the experimental data as seen from the solid curve in the same figure. At the switching

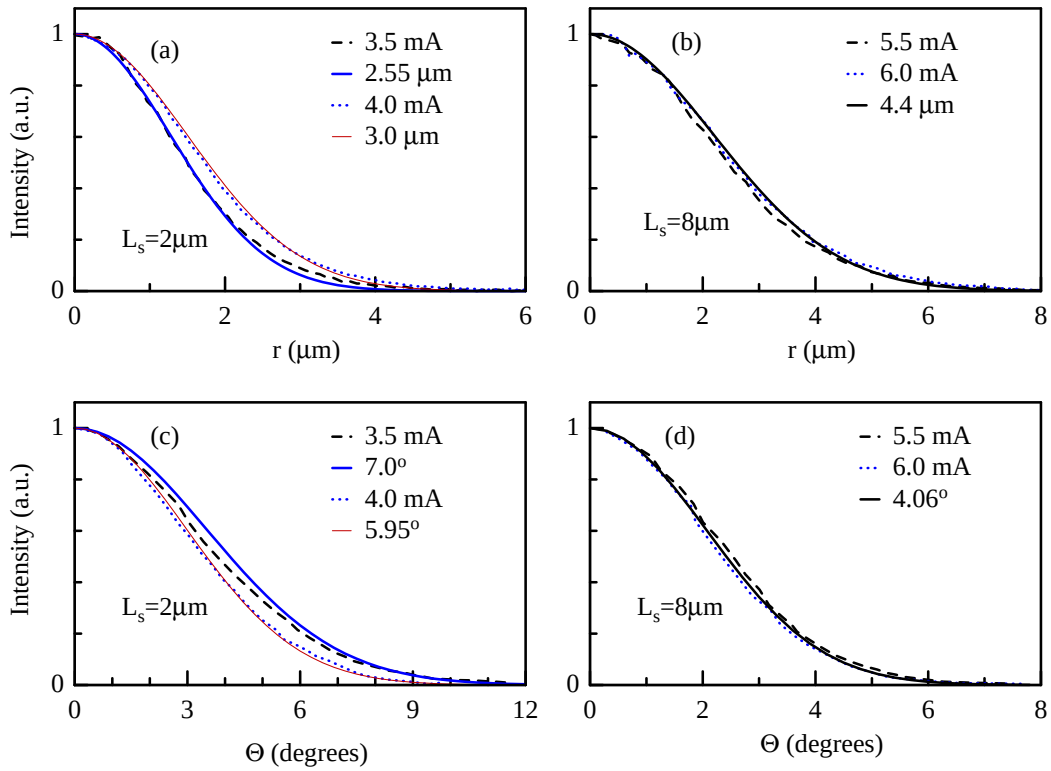


Fig. 4.5: *(a) Measured near-field intensity distributions for a 4 µm aperture device at 3.5 mA (dashed curve) and 4 mA (dotted curve) and fit data (thick and thin solid curves) with the mode radius w_0 given in the legend. (b) The same measurements as in (a) for a VCSEL with 8 µm active diameter at 5.5 mA (dashed curve) and 6 mA (dotted curve), the latter fitted to a Gaussian profile (thick solid curve). (c) Measured far-field intensity distributions for the same case as in (a) and the Fourier transformation of the Gaussian profiles (thick and thin solid curves) with their respective values of θ. (d) Measurements and calculations as in (c) for the device from (b).*

point these calculations show 17 % beam half-width shrinkage for the strongly confined mode $\mathrm{LP}_{01}^{(+1)}$, which is in agreement with the measured value. If a transition from step- to parabolic-like guiding is not taken into account, this value is increased to 34 %. In the case of $\mathrm{L}_s = 8\,\mu\mathrm{m}$, corresponding to the dotted curve in Fig. 4.6(c), only a small difference in Δ_n at 6 mA is observed because the oxide induced index change for the two modes is reduced owing to the increased cavity length and thus reduced longitudinal filling factor. Thermal lensing is also reduced due to the increased spacer length and associated smaller thermal resistance but is increased of course for increasing pumping current. In total, this leads to the dominance of thermal lensing and thus the index profile can be approximated by a parabolic profile over the whole current range. The use of (3.11) fits the measured data when $\Delta\bar{n}_\mathrm{fc} = -5 \cdot 10^{-4}$, as shown by the dotted curve in Fig. 4.6(a). The beam half-width shrinkage in this case for the strongly confined mode $\mathrm{LP}_{01}^{(-1)}$ is reduced to 5 %

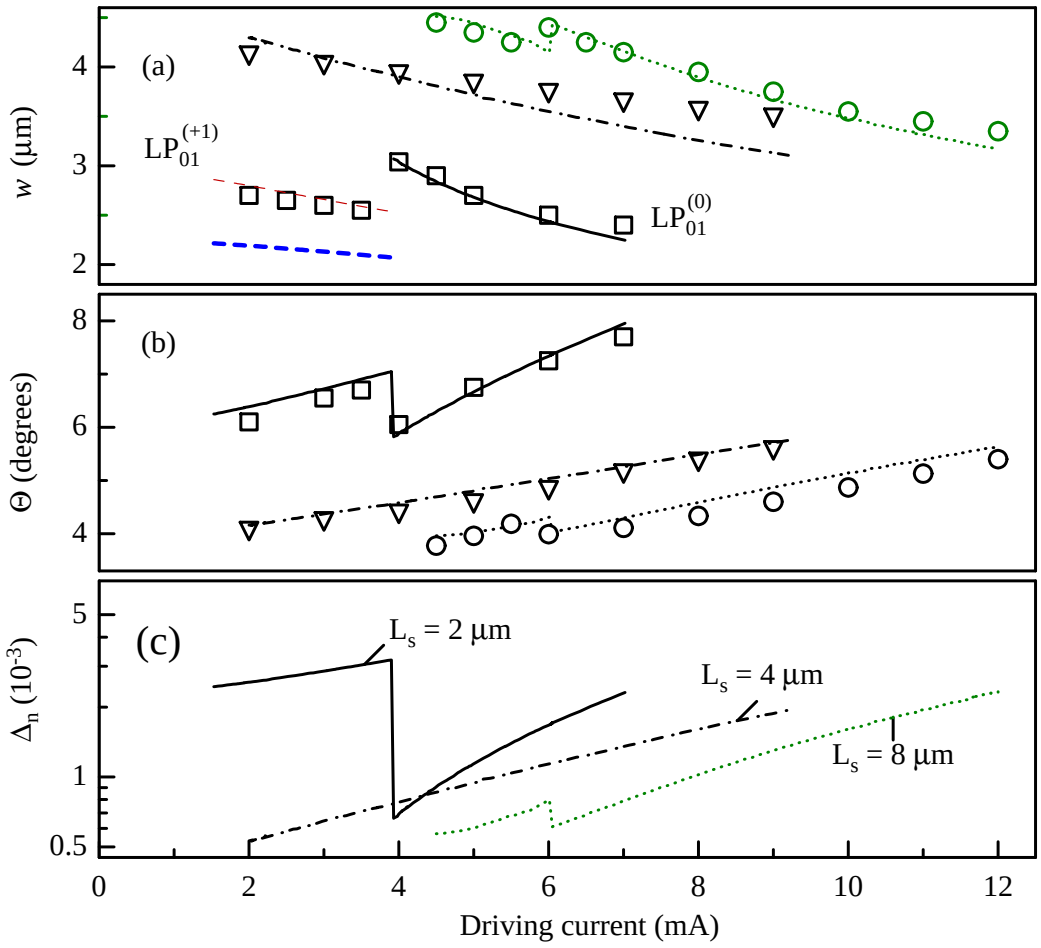


Fig. 4.6: *For the VCSELs of Fig. 4.4: (a) Measured beam radius w_0 (open squares, triangles and circles) and calculated values using (3.27) (thin dashed curve) and (3.11) (solid, thick dashed, dotted dashed and dotted curves). (b) Measured beam divergence half-angle Θ (open squares, triangles and circles) and the calculated values (solid, dashed dotted and dotted curves). (c) Calculated induced index step.*

at the switching point because $\Delta\bar{n}_{\mathrm{ox}}$ is reduced by an order of magnitude compared to the $L_s = 2\,\mu$m device. In the case of $L_s = 4\,\mu$m, the dashed dotted curve in Fig. 4.6(c) represents Δ_{n} with $\Delta\bar{n}_{\mathrm{fc}} = -2 \cdot 10^{-4}$. In this case there is no mode switching and the use of (3.11) reproduces the experimental data as illustrated by the dashed dotted curve in Fig. 4.6(a). A smaller $|\Delta\bar{n}_{\mathrm{fc}}|$ is to be expected since the cumulative free carrier induced wavelength shift is dependent on the effective cavity length. The value $|\Delta\bar{n}_{\mathrm{fc}}|$ for $L_s = 4\,\mu$m is smaller than that for the $8\,\mu$m spacer because the latter shows significantly increased threshold current. The e^{-2}-beam divergence half-angle θ is calculated using the formula (3.38) which reproduces the measured data for all lasers, as seen in Fig. 4.6(b).

4.2 Transverse Mode Structure

To investigate the effect of increasing the cavity length on the transverse mode structure and output characteristics of VCSEL it is most convenient to study the two cases in which only one longitudinal mode oscillates, namely the cases of 0 and 4 μm spacer lengths.

4.2.1 Output characteristics

Figure 4.7(a) shows the output characteristics for a 5 μm active diameter VCSELs with 0 μm spacer (solid curves) and 4 μm spacer (dashed curves).

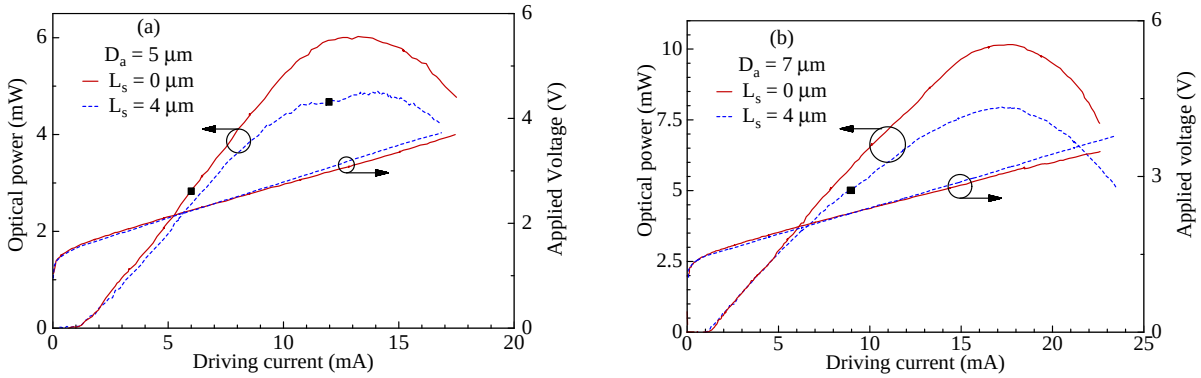


Fig. 4.7: *(a) Light output characteristics for VCSELs with the same active diameter $D_a = 5\,\mu m$, but different spacer thickness L_s of 0 and 4 μm defined by solid and dashed curves, respectively. (b) The same as in (a), but for VCSELs with $D_a = 7\,\mu m$. Solid squares indicate the onset of higher order transverse modes, i.e. the decrease of side-mode suppression ratio below 30 dB.*

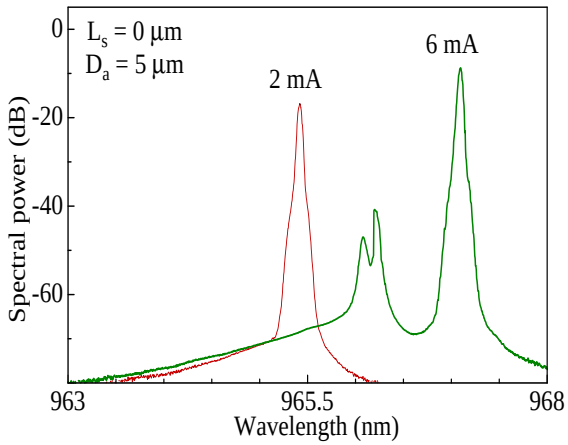
As can be seen the two devices have the same threshold currents, but the case of 4 μm spacer length results in a slightly lower differential efficiency than the 0 μm spacer. In part (b) of Fig. 4.7 the output characteristics for a 7 μm active diameter VCSELs with 0 μm spacer (solid curves) and 4 μm spacer (dashed curves) is depicted. The general characteristics are similar to those in part (a) especially the decrease of the differential efficiency for the VCSEL with 4 μm spacer length. Maximum single-mode output is determined by 30 dB sidemode suppression ratio (SMSR) which for a 5 μm aperture VCSELs is indicated in Fig. 4.7(a) by solid squares. It reveals that the current range for single-mode operation for a 4 μm spacer device is two times that of the 0 μm one. Also, the case of the 7 μm aperture VCSEL is surprising since the 4 μm spacer device oscillates on single transverse mode up to 9 mA whereas the 0 μm spacer device begins to oscillate on two transverse

modes at threshold current. Spectra of the emitted light measured by using a spectrum analyzer[1] with a maximum resolution of 10 pm will be introduced in the next section.

4.2.2 Near-field measurements

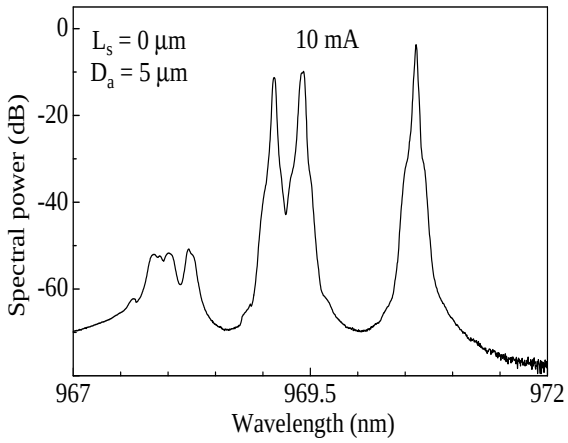
The spatial distributions of the eigenmodes for the above mentioned VCSELs are measured using a near field setup. The measured intensity distributions of the transverse modes emitted from a 5 μm aperture device with 0 μm spacer at 6, 10 and 16 mA drive currents are summarized in Fig. 4.8. In the range from threshold up to 6 mA only the fundamental LP_{01} mode oscillates because this device is relatively small and as a result this mode has highest gain. At 10 mA drive current, besides LP_{01} there are two orthogonal higher order LP_{11} modes. These two modes agree with the calculated ones in Fig. 3.4 which correspond to the inclusion of the theoretical solution (3.13) of either $\cos^2(l\varphi)$ or $\sin^2(l\varphi)$. As the current increases up to 16 mA, the LP_{01} mode disappears and besides the two LP_{11} modes another higher order LP_{02} mode oscillates which is slightly distorted. The distortion of this mode is also observed in [39] and is caused by a slightly non-circular symmetry of the oxidation layer in the VCSEL device which may arise from the dependence of the oxidation rate on the crystal direction. In total, the number of the eigenmodes of this device is four. This number is increased to twelve modes by increasing the active diameter to 7 μm as can be seen in Fig. 4.9. This VCSEL device begins to lase on a multiple mode due to its relatively large active diameter. In such large devices, the lateral carrier distribution can be changed in such a way that the higher order modes can attain the same gain as the fundamental mode or even more. At 6 mA drive current, besides LP_{01} there are two orthogonal higher order LP_{11} modes. In addition to these higher LP_{11} modes, another two orthogonal LP_{21} modes and an LP_{02} are observed at 16 mA. Finally, at 22 mA four pairs of LP_{21}, LP_{12}, LP_{31}, and LP_{41} modes oscillate simultaneously in addition to the LP_{02}.
The total number of transverse modes for VCSELs with 4 μm spacer is reduced significantly. As can be seen In Fig. 4.10 for a 4μm VCSEL of this type, only the fundamental LP_{01} mode oscillates up to 12 mA and the two components of the higher order LP_{11} modes are superposed to give LP^*_{11} (donut-mode) at 16 mA. In comparison with the same size VCSEL with 0 μm spacer of Fig. 4.8 one can conclude that the wavelength difference between the LP_{11} mode components becomes too small to be detected and as a result giving rise to the existence of a superposition of these two components in the form of LP^*_{11} mode. Also, the LP_{02} mode disappears by increasing the cavity length of such small devices.

[1] ANDO Optical Spectrum Analyser AQ6317



LP_{01} (967.08 nm)

6 mA
$\Longrightarrow$



$\Longleftarrow$ 10 mA
$\Downarrow$

LP_{01} (970.62 nm)

LP_{11} (969.41 nm)

LP_{11} (969.11 nm)

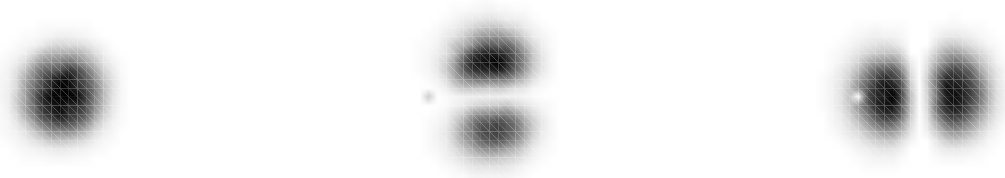
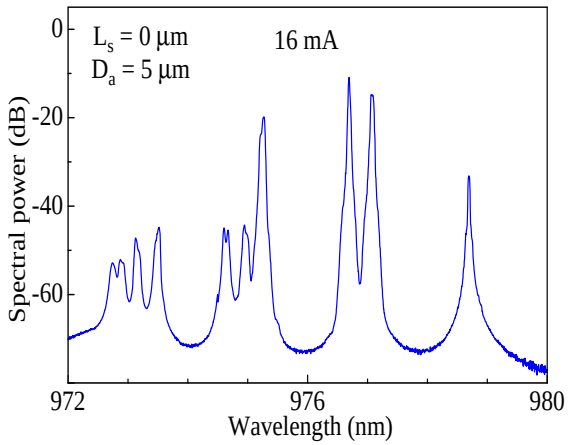


Fig. 4.8: *Measured near field eigenmodes of a* $5\,\mu m$ *aperture VCSEL with* $0\,\mu m$ *spacer at* $6, and 10\,mA$ *drive currents.*



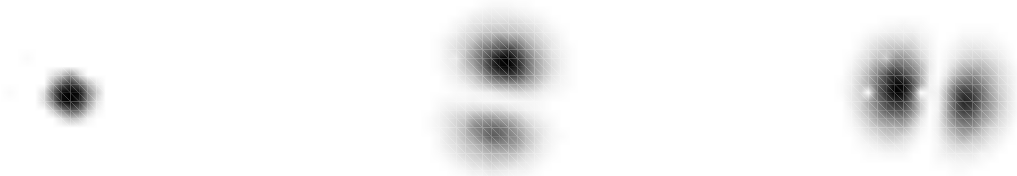
$\Longleftarrow$ 16 mA

$\Downarrow$

LP_{01} (978.69 nm)

LP_{11} (977.07 nm)

LP_{11} (976.69 nm)



LP_{02} (975.23 nm)

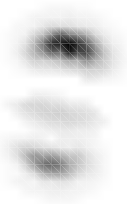
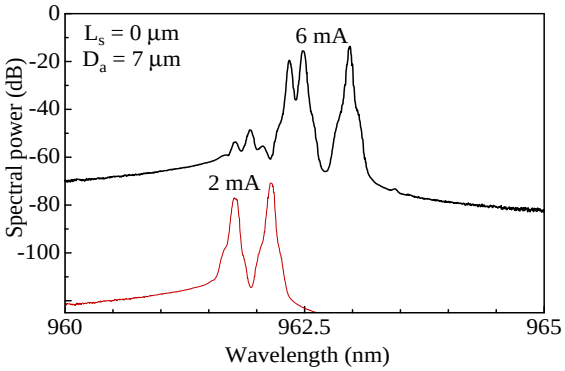
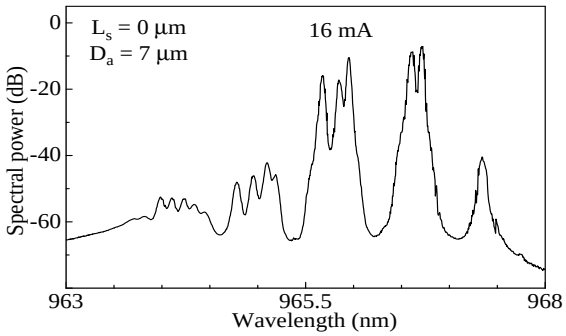


Fig.4.8: *Continued measurements at* 16 *mA drive current.*





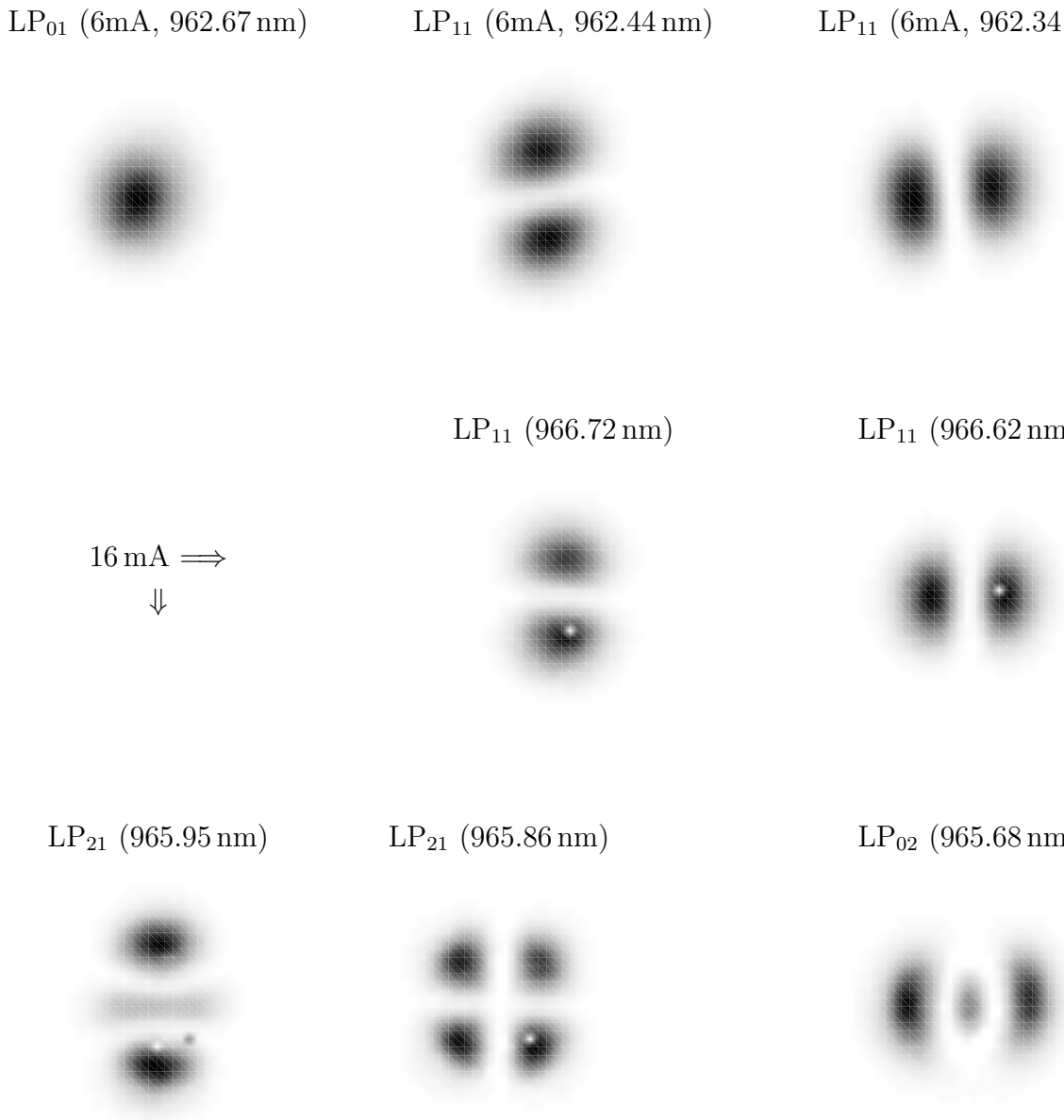
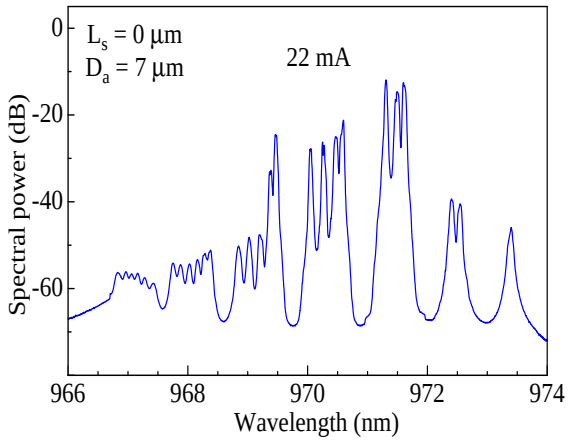
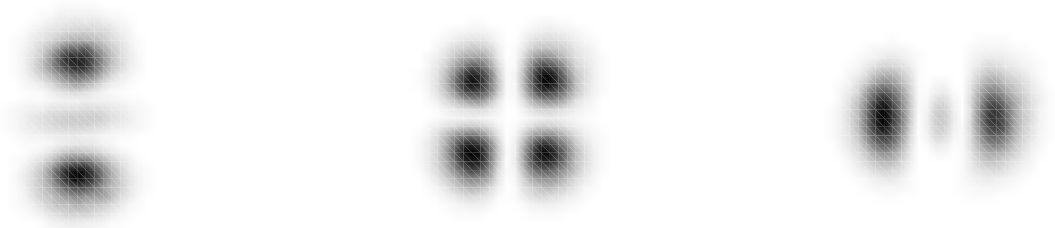


Fig. 4.9: *Measured near field eigenmodes of a* $7\,\mu m$ *aperture VCSEL with* $0\,\mu m$ *spacer at* $6, 16$ *and* $22\,mA$ *drive currents.*

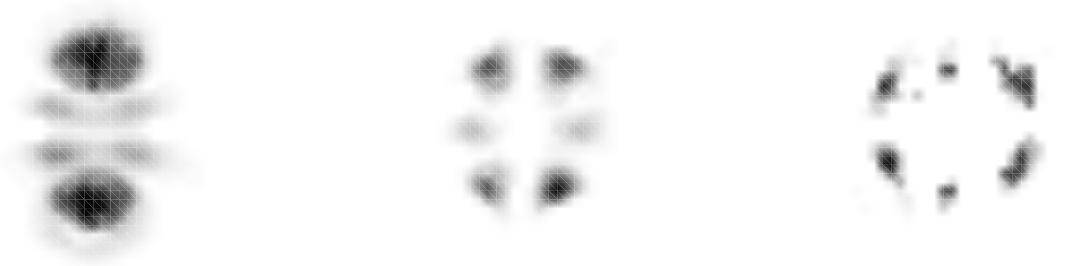


⟸ 22 mA
⇓

LP_{21} (971.61 nm) LP_{21} (971.5 nm) LP_{02} (971.31 nm)



LP_{12} (970.58 nm) LP_{31} (970.47 nm) LP_{31} (970.26 nm)



LP_{12} (970.05 nm) LP_{41} (969.47 nm) LP_{41} (969.38 nm)

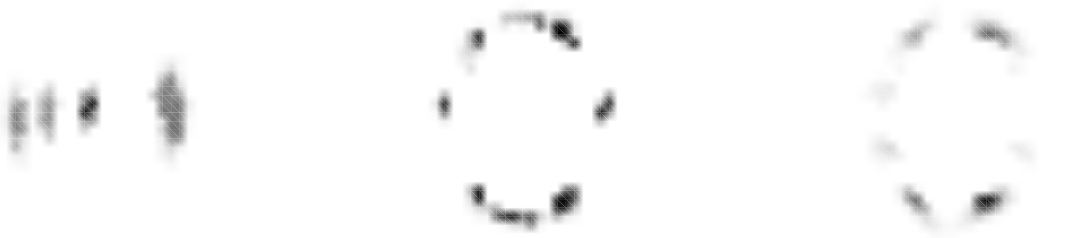


Fig.4.9: *Continued measurements at 22 mA drive current.*

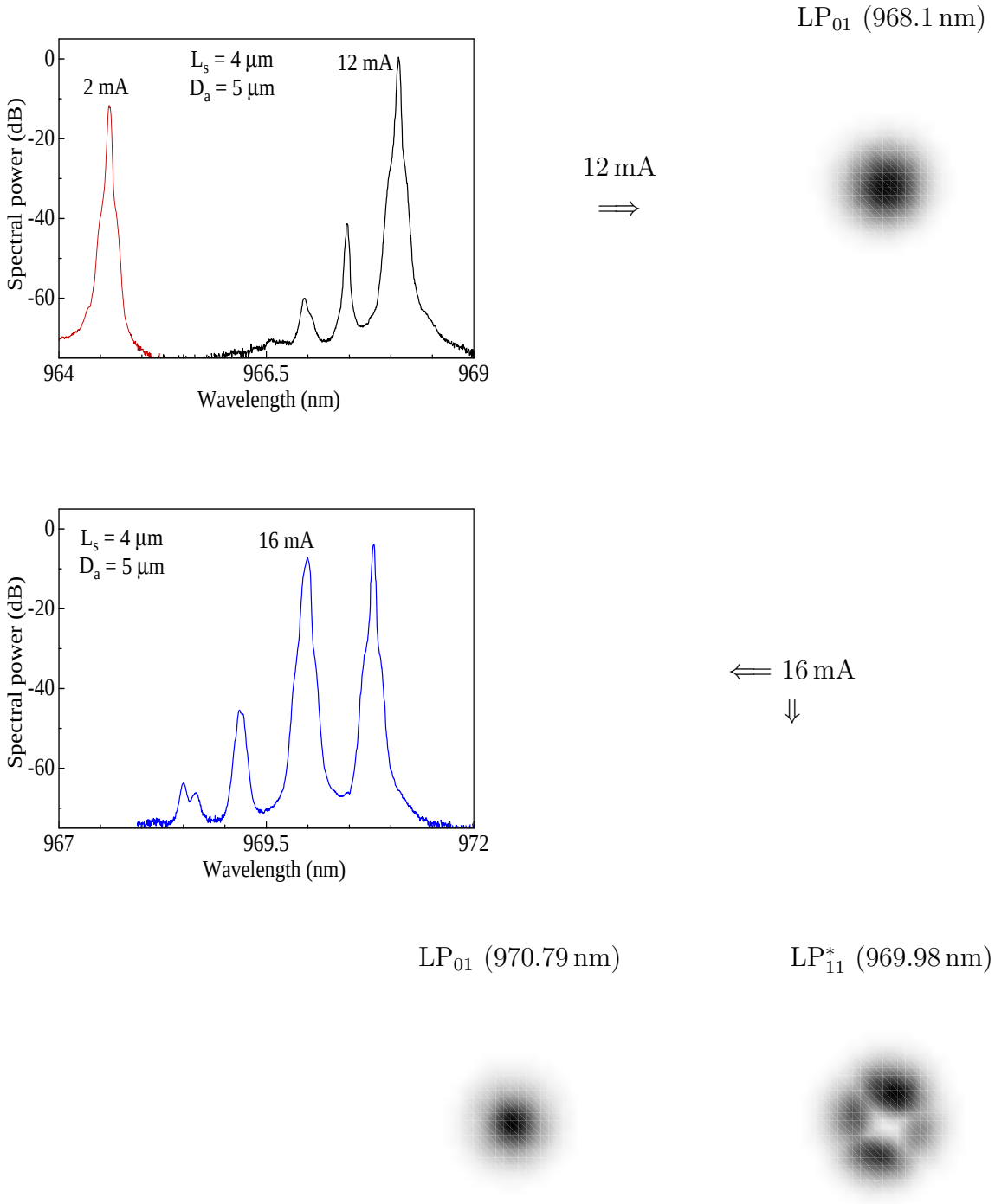


Fig. 4.10: *The same measurements as in Fig. 4.9 but for VCSEL with* $4\,\mu m$ *spacer at* 12*, and* $16\,mA$ *drive currents.*

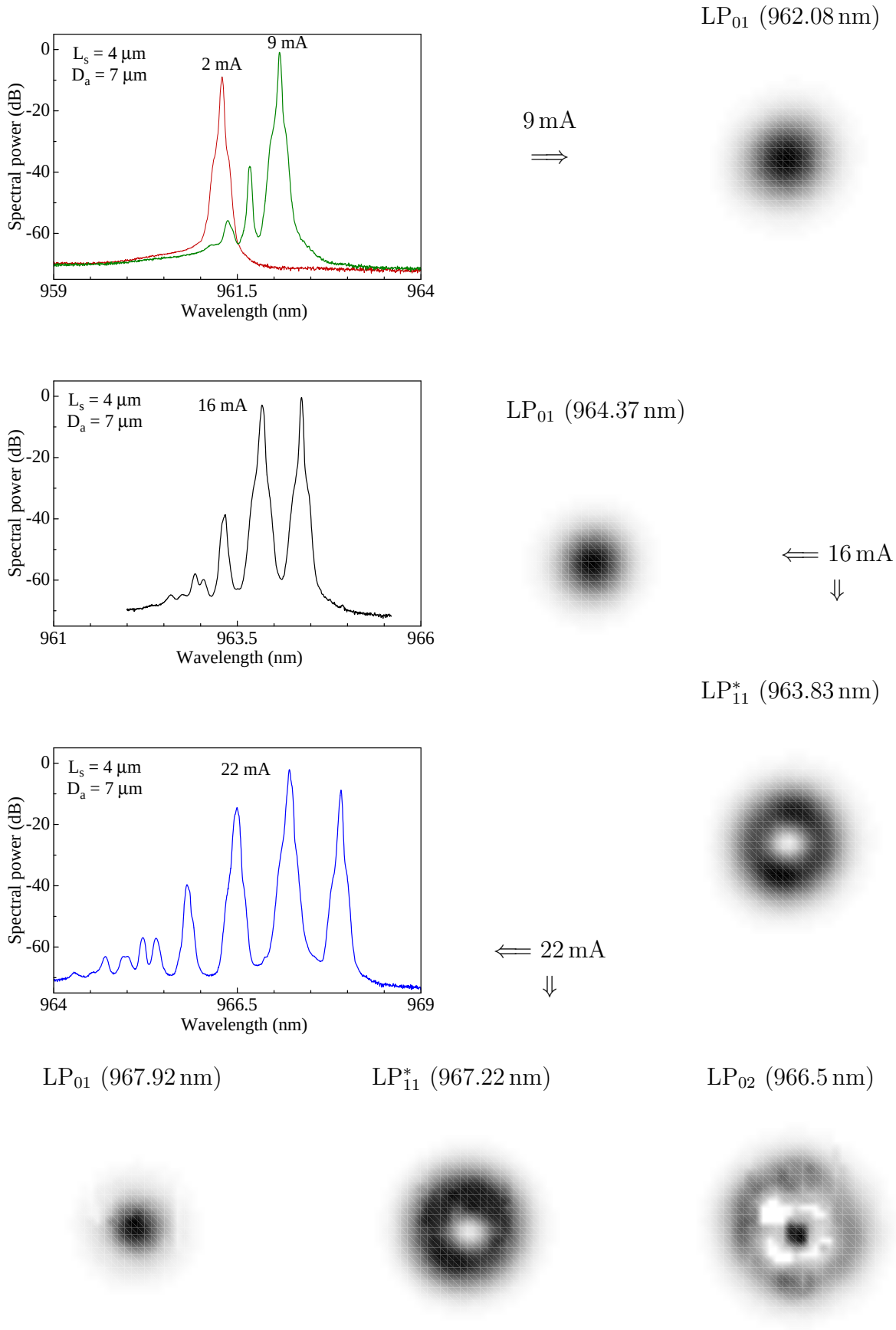


Fig. 4.11: *The same measurements as in Fig. 4.9 but for VCSEL with* $4\,\mu m$ *spacer at* 9, 16 *and* 22 *mA drive currents.*

Figure 4.11 shows the measured eigenmodes of a 7μm aperture device with 4μm spacer. As can be seen, only the the fundamental LP_{01} mode is dominant up to 9 mA. This mode oscillates simultaneously with the LP^{*}_{11} mode at 16 mA. Finally, at 22 mA the LP_{02} mode is added to these two modes during lasing action. The same conclusion as that for the 4μm aperture VCSEL can be drawn for the LP^{*}_{11} mode. Also, in comparison with the same size VCSEL with 0μm spacer of Fig. 4.9 one can see that the four pairs of LP_{21}, LP_{11}, LP_{31}, and LP_{41}, modes disappear by increasing the cavity length of such relatively large devices.

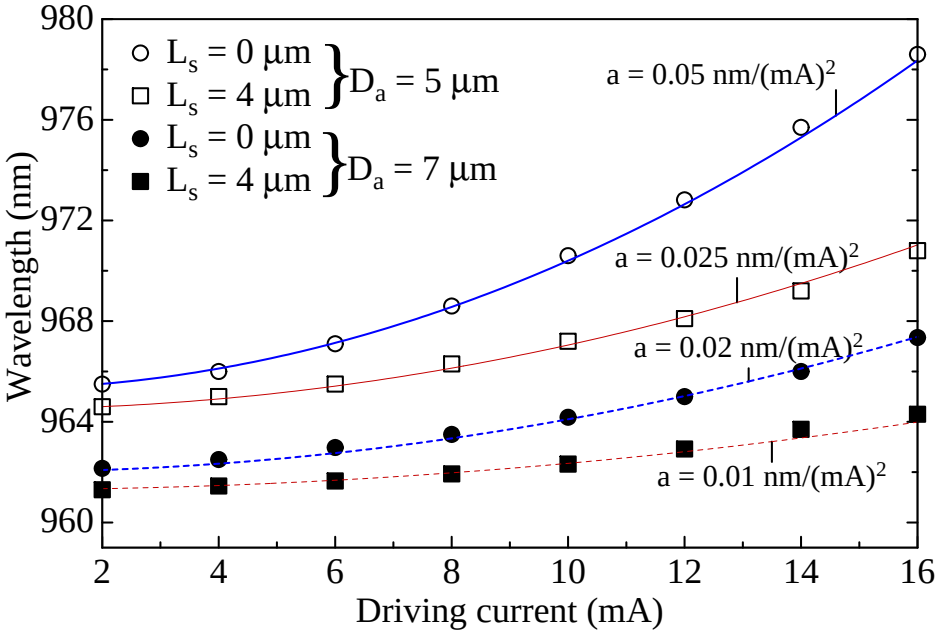


Fig. 4.12: *Wavelengths of the zeroth order mode as a function of injection current. The parameter a describes the curvature fit parameter of the parabolic curve.*

The reduced number of eigenmodes for VCSELs with long cavity acts as an important feature for these devices. This confirms the principle of design for these devices, i.e. the increased scattering losses of the higher order modes due to the lateral increase of the mode area with increasing the cavity length. This can also explain why there exists a decrease of the differential efficiency for such these devices. Moreover, the increased range of pump current in single-mode operation is due to the reduction of the induced refractive index as the cavity length is increased. Another interesting feature of this class of VCSELs is the relatively stable operating wavelength by changing the drive current specially for large devices. In Fig. 4.12 the wavelengths of the the zeroth mode for the VCSELs in Fig. 4.7 are plotted as a function of current. The wavelength increases with drive current as joule heating increases the refractive index and thus the resonance wavelength. This effect is much stronger in small lasers with 0 μm spacer length. However, the wavelength

of the zeroth order mode in the 4 μm spacer lasers redshifts at a much lower rate. This can be seen in Fig. 4.12 where a parabolic profile $\Delta\lambda = a(I - I_{th})^2$ is used to fit the observed wavelength shift of the fundamental mode. It shows that the curvature parameter a in the case of 4 μm spacer devices is reduced by a factor of two compared to the case of 0 μm spacer.

Chapter 5

Glass Optical Fibers

The optical fibers represent a certain type of dielectric waveguides for guiding light waves. These waveguides are called fibers because of their filamentary appearance. The present chapter is devoted to a discussion of the properties and types of optical fibers. In addition, the theory of modal fields, butt-coupling efficiency, and macrobending fiber effects will be presented.

5.1 Theory

5.1.1 Optical principles and properties

Typically, an optical fiber consists of three main concentric elements as shown in Fig. 5.1(a). The central region (core), made of silica with refractive index $\bar{n}_{\mathrm{c}}$, is the light-transmitting region of the fiber. The cladding can be made of the same material as the core, but with a refractive index $\bar{n}_{\mathrm{cl}}$ about 1 % lower. This causes internal reflection within the core so that light is transmitted through the fiber. The coating consists of one or more layers of plastic that protect against physical or environmental damage to the light-transmitting region. Two classes of optical fibers are usually distinguished. In the first class, the core material is homogeneous and has a flat index profile with an index step Δ_n at the core-cladding interface, as shown in Fig. 5.1(b) and (c). Reflection in this situation is governed by Snell's law [33]. Thus in terms of complementary angles, the incident ray with an angle θ at the core-cladding interface is totally internally reflected if $0 < \theta \leq \theta_{\mathrm{c}}$, and is partially reflected and partially refracted if $\theta_{\mathrm{c}} < \theta \leq \pi/2$, where θ_{c} is the complement of the critical angle α_c for total internal reflection, which according to Snell's law is

$$\theta_{\mathrm{c}} = \cos^{-1}\left(\frac{\bar{n}_{\mathrm{cl}}}{\bar{n}_{\mathrm{c}}}\right) = \sin^{-1}\left(1 - \frac{\bar{n}_{\mathrm{cl}}^2}{\bar{n}_{\mathrm{c}}^2}\right) \quad . \tag{5.1}$$

When electromagnetic radiation is guided, such as light in an optical fiber, the wave nature of the radiation results in phase shifts of the wavefronts at the reflective boundaries. There are discrete number of paths, called modes, for which the reflections at the interface produce constructive phase shifts that reinforce the transmission. Each mode travels

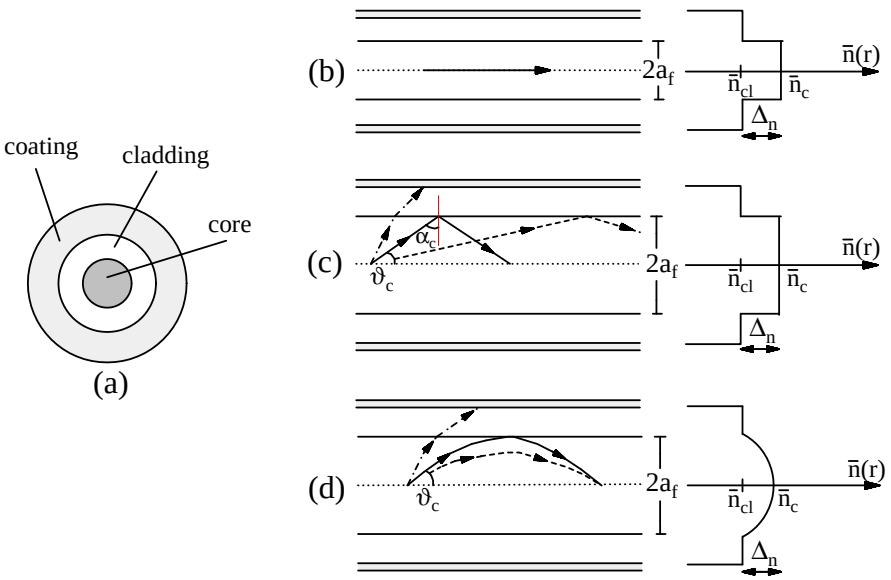


Fig. 5.1: *Schematic cross section of an optical fiber (a). Sketch of single-mode with homogeneous core (b), two cladded multi-mode fibers with a homogeneous core (c) and with a graded core (d). The critical ray is indicated by a solid line whereas the possible guided and unguided rays are represented by broken lines.*

through the fiber at a different angle to the fiber axis, so each one travels a different path length from input to output of the fiber. The number of modes that can be propagated in a given optical fiber is determined by the wavelength λ of the light and the properties of the the fiber such as core radius a_f, core refractive index $\bar{n}_\mathrm{c}$ and cladding refractive index $\bar{n}_\mathrm{cl}$. These parameters are combined in a single dimensionless parameter $\bar{V}$, known as waveguide frequency parameter [33]

$$\bar{V} = \frac{2\pi a_\mathrm{f}}{\lambda}\sqrt{\bar{n}_\mathrm{c}^2 - \bar{n}_\mathrm{cl}^2} = \frac{2\pi a_\mathrm{f}}{\lambda} \cdot NA \quad , \tag{5.2}$$

where the quantity $NA = (\bar{n}_\mathrm{c}^2 - \bar{n}_\mathrm{cl}^2)^{1/2}$ is often referred to as the numerical aperture of the fiber. The dimensions of the inner core that permit single mode operation depend critically on the ratio of $\bar{n}_\mathrm{c}/\bar{n}_\mathrm{cl}$. The larger this ratio, the smaller a_f must be to ensure that only one guided mode can propagate. The condition of single-mode operation is that

$$\bar{V} < \bar{V}_\mathrm{cutoff} = 2.405 \quad . \tag{5.3}$$

For lasers typically used as sources with wavelengths in the range of 850-1550 nm, the core diameter of single-mode fiber is in the range of 3-10 μm. This type of fiber has high bandwidth (a measure of the data carrying capacity) of 100 GHz·km, so that all modern long range communication systems employ single-mode fiber. On the other hand,

step index multi-mode fiber has a core diameter of 100-1500 μm and has two disadvantages. The first is the scatter loss of the guided signal produced by imperfections at the core cladding interface and the second is the delay distortion of the signal arising from pathlength differences among the possible propagation directions. These fibers have low bandwidth in the order of 20 MHz·km. For communication applications, the transmission distances must be kept short to reduce modal dispersion. These fibers are suitable for applications requiring high power density like medical and industrial laser power delivery. In the second class as can be seen in Fig. 5.1(d), an inhomogeneous core with a graded-index (GI) profile diminishs these problems. The graded profile provides continuous focusing to the light, so that the energy is concentrated along the axis, and a little of it reaches the interface. Pathlength differences among the various propagation paths are compensated by velocity variations across the core region leaving very little delay distortion. This greatly reduces modal dispersion in the fiber. GI fibers have bandwidths of 500 and 160 MHz·km at 1300 and 850 nm, respectively. It is significantly higher than step-index multi-mode fibers (but still much lower than single-mode fibers). The core diameters of GI fibers are 50, 62.5, or 100 microns. Their main application is in medium-range communications, such as local area network.

5.1.2 Mode profiles in step-index fibers

For a cylindrical waveguide with effective refractive indices $\bar{n}_\mathrm{c}$ for the core and $\bar{n}_\mathrm{cl}$ for the cladding, the scalar Helmholtz equation has the form [33]

$$\nabla_{tr}^2 E(r,\varphi) + (\bar{n}^2 k^2 - \beta^2) E(r,\varphi) = 0 \quad . \tag{5.4}$$

The transverse electric field $E_l(r,\varphi)$ of linearly polarized LP_{lp} mode, where the indices l and p stand for azimuthal and radial order of the mode, can be expressed by Bessel function J_l and modified Hankel function K_l of order l as

$$E(r,\varphi) = E\cos(l\varphi) \cdot \begin{cases} J_l(ur/a_\mathrm{f})/J_l(u) & \text{for } r \le a_\mathrm{f} \\ K_l(vr/a_\mathrm{f})/K_l(v) & \text{for } r > a_\mathrm{f} \end{cases} \tag{5.5}$$

with azimuthal angle φ, propagation constant β, and electric field strength E. On non-absorbing waveguides bound modes have real values of u and v called modal parameters for the core and cladding defined by

$$u = a_\mathrm{f}\sqrt{k^2\bar{n}_\mathrm{c}^2 - \beta^2} \quad , \quad v = a_\mathrm{f}\sqrt{\beta^2 - k^2\bar{n}_\mathrm{cl}^2} \tag{5.6}$$

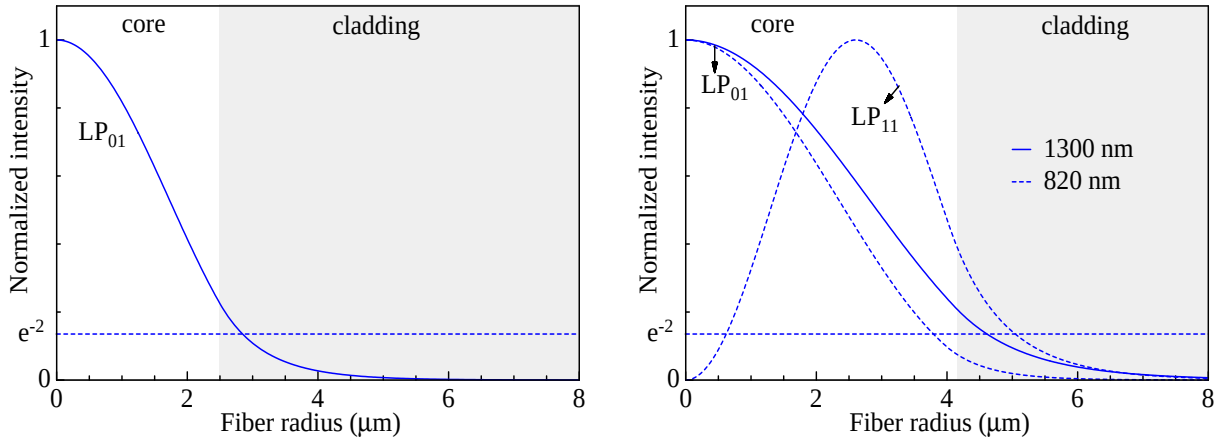


Fig. 5.2: *Intensity profile of the fundamental LP_{01} mode of a step index SMF with $a_f = 2.5\,\mu m$ at 820 nm wavelength (left) and first two LP_{lp} modes of SMF with $a_f = 4.15$ (right) at 1300 nm (solid curve) and 820 nm (dashed curves). Fiber index parameters are $NA = 0.11$ and $n_c = 1.54$.*

where $\bar{n}_c$ and $\bar{n}_{cl}$ are the core and cladding refractive indices and $k = 2\pi/\lambda$. The magnitude square of $E(r, \varphi)$ gives the intensity profile of the fiber eigenmodes. For example, the $5\,\mu$m SMF with index parameters, $NA = 0.11$, and $n_c = 1.54$ [44] has $\bar{V} = 2.1$ at 820 nm wavelength. According to the condition (5.3), only the fundamental LP_{01} mode can propagate in this fiber. The left part of Fig. 5.2 shows the calculated intensity profile of this mode. As can be seen because of the small size of the core in a SMF, approximately 20 % of the intensity propagates in the cladding. The mode field radius w_F is defined as the the spot radius at which the intensity has dropped to $1/e^2$ of its maximum value at the center which in this case equals $2.85\,\mu$m. On the other hand, the $8.3\,\mu$m standard SMF for 1300 nm wavelength with the same index parameters as the forementioned SMF has $\bar{V} = 2.2$. This means also that only the fundamental LP_{01} mode can propagate in this fiber at the operating wavelength as illustrated by the solid curve in the right part of Fig. 5.2. When the wavelength is reduced to 820 nm, the frequency parameter increases to $\bar{V} = 3.4$ and as a result both LP_{01} and LP_{11} can be guided in this fiber as can be seen in the right part of Fig. 5.2, dashed curves. It becomes clear that w_F of the LP_{01} mode increases from $3.8\,\mu$m to $4.65\,\mu$m by increasing the wavelength from 820 nm to 1300 nm, respectively.

5.1.3 Attenuation by waveguide bends

Microbending is the result of microscopic imperfections in the fiber geometry caused by manufacturing process or mechanical stress. Macrobending occurs when the fiber is bent into a curvature with diameter on the order of centimeters. Both effects cause light rays

to hit the core-cladding interface at less than the critical angle, so that optical energy is lost into the cladding.

5.1.4 Macrobending of optical fibers

On a straight fiber of arbitrary profile, the modal field at every point in the cross section propagates parallel to the fiber axis with the same phase velocity, so that planes of constant phase are orthogonal to the axis. However, if the fiber is bent into a planar arc of constant radius R, as can be seen in Fig. 5.3, it is intuitive that the fields and phase fronts rotate about the center of curvature of the bend with constant angular velocity. Consequently, the phase velocity parallel to the fiber axis must increase linearly with distance from the center of curvature, so that

$$v_{ph}(r) = (R + r)v_{ph}(R)/R \quad , \tag{5.7}$$

where $v_{ph}(R) = \omega/\beta = \omega/(kn_c \sin\alpha)$ denotes the phase velocity on the axis, α is the angle of incidence and $k = 2\pi/\lambda$. Since the fiber has a uniform cladding and the phase velocity cannot exceed the local speed of light, there will be a certain radius R_c in the plane of the bend at which the phase velocity of the surrounding cladding is reached i.e.

$$v_{ph}(R_c) = \omega/(kn_{\mathrm{cl}}) \quad . \tag{5.8}$$

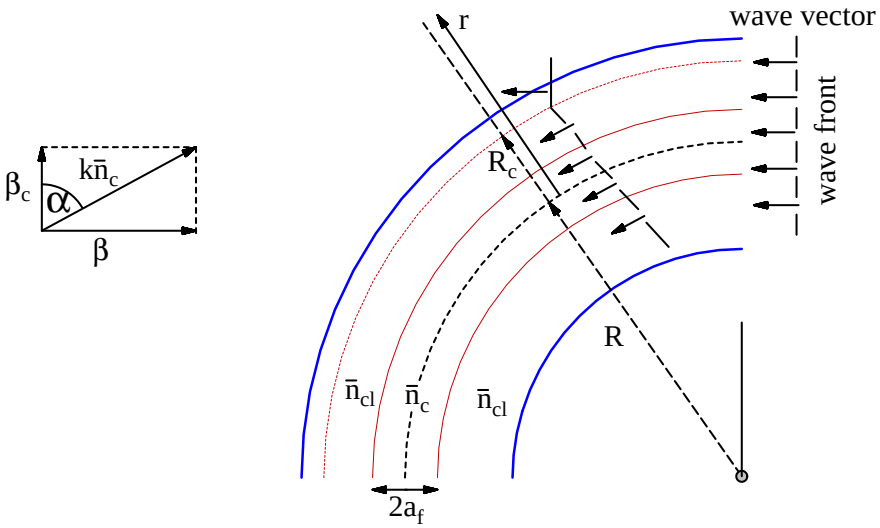


Fig. 5.3: *Section of a fiber bent into an arc of radius R. The core profile has index n_c over the diameter $2a_f$, and n_{cl} is the uniform cladding index. The fiber fields are denoted by arrows.*

Beyond R_c the phase velocity cannot remain in step, and the fields in this region must therefore become radiative. In a circular fiber loop of radius R and length z the optical power of a given mode decreases according to

$$P(z) = P_0 \exp(-\alpha\, z) \tag{5.9}$$

where P_0 is the initial mode power, α is the power attenuation coefficient which for LP_{lp} modes has the form [45]

$$\alpha = \frac{c_1}{\sqrt{a_\mathrm{f}\, R}} \exp(-R/c_2) \quad , \tag{5.10}$$

with the constants

$$\begin{aligned} c_1 &= \frac{\frac{\sqrt{\pi}}{(1+\delta_{l0})}}{K_{l-1}(v)\, K_{l+1}(v)} \left(\frac{u}{\bar{V}}\right)^2 v^{-\frac{3}{2}} \quad , \\ c_2 &= \frac{3}{4} \frac{\bar{V}^2}{v^3} \frac{a_\mathrm{f}}{\Delta} \quad , \\ \delta_{l0} &= \begin{cases} 1 & l = 0 \\ 0 & l \neq 0 \end{cases} \quad , \end{aligned}$$

where K_l is Hankel function and the modal parameters u and v are defined by (5.6).

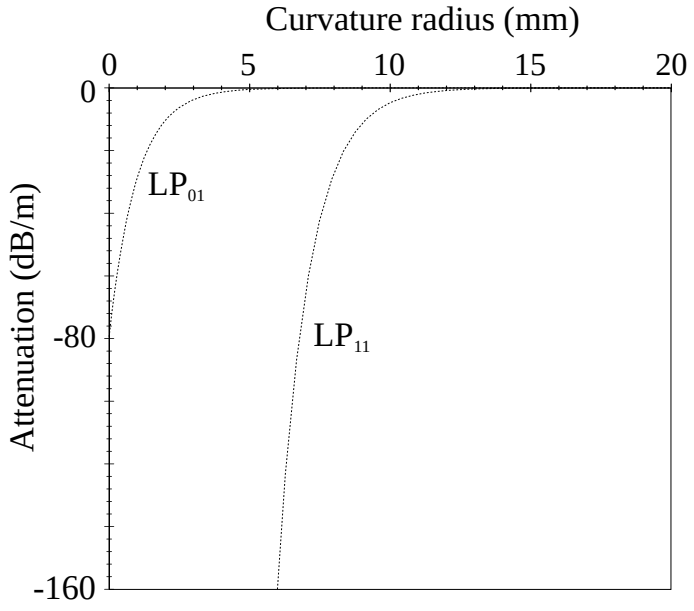


Fig. 5.4: *Power attenuation coefficient of LP_{01} and LP_{11} in relation to the bend radius for 8.3 µm SMF at 820 nm wavelength.*

Figure 5.4 illustrates the calculated power attenuation coefficient for LP_{01} and LP_{11} modes in relation to the curvature radius R. These calculations are carried out using (5.10) for an optical fiber with 8.3 μm core diameter at 820 nm wavelength. It is seen that the modal power for both LP_{11} and LP_{01} begins to attenuate at the bend radii of 13 and 5 mm, respectively. This means that the higher order LP_{01} mode is less sensitive for the bend radius than LP_{11} because the latter has a significant modal power in the cladding region as can be seen in Fig. 5.2. Although the power attenuation by macrobending represents a disadvantage of an optical fiber, it is sometimes useful to be used as a filter that selects the fundamental LP_{01} mode and attenuates the other higher order modes.

5.1.5 Coupling efficiency

The modal butt-coupling efficiency η_m of VCSEL into flat cut uncoated optical fibers can be calculated by evaluating the overlap integral [46] , [1] between VCSEL and fiber mode fields in the plane perpendicular to the fiber and laser axes as can be seen in Fig. 5.5.

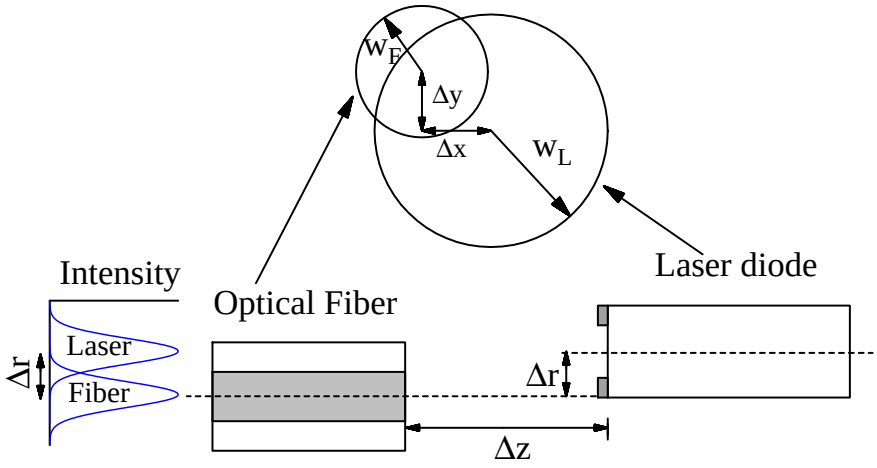


Fig. 5.5: *Schematic view of coupling efficiency of laser diode into flat cut single-mode optical fiber (SMF).*

The overlap integral is

$$\eta_m = \frac{\left| \int\int_{-\infty}^{+\infty} E_L(x,y)\, E_F^*(x,y) dx\, dy \right|^2}{\int\int_{-\infty}^{+\infty} |E_L(x,y)|^2\, dx\, dy \int\int_{-\infty}^{+\infty} |E_F(x,y)|^2\, dx\, dy} \quad . \tag{5.11}$$

To calculate the integral analytically, a normalized Gaussian function is used for the zeroth LP_{01} mode fields in both VCSEL $E_L(x,y)$ and fiber $E_F(x,y)$ with field radii w_L and w_F, respectively. The fields are given by

$$E_L(x,y) = \exp\left(-\frac{x^2+y^2}{w_L^2}\right) \tag{5.12}$$

and

$$E_F(x,y) = \exp\left(-\frac{(x+\Delta x)^2}{w_F^2} - \frac{(y+\Delta y)^2}{w_F^2}\right) \quad , \tag{5.13}$$

where Δx and Δy represent the displacement of the fiber axis relative to the laser axis in both x and y directions. However, it is assumed that the axes of VCSEL and fiber are not tilted, and field curvature is neglected. The integration (5.11) is easily evaluated to give

$$\eta_m = \frac{4}{\left(\frac{w_F}{w_L} + \frac{w_L}{w_F}\right)^2} \cdot \exp\left(\frac{-2\Delta r^2}{w_L^2 + w_F^2}\right) \tag{5.14}$$

with $\Delta r^2 = \Delta x^2 + \Delta y^2$. It is clear from (5.14) that η_m depends mainly on the offset (Δr) between the laser and fiber axes and the field radii of both laser and optical fiber. In addition, it depends on the longitudinal translation (Δz) which is included in w_L as a dominant variable as described by (3.35) where the laser beam diverges as it emanates from the source.

5.2 Experiment and Discussion

5.2.1 Step-index single-mode fibers

The spatial variation of η_c is measured using the near field scanning system mentioned in chapter 3. Figure 5.6 shows the measured η_m (open circles) for an optical fiber with core diameter $D_F = 5\,\mu$m at the longitudinal positions $\Delta z = 10$, 20, and $30\,\mu$m from a VCSEL with spot size $w_L = 2.7$, 3.3, and $4.1\,\mu$m at these positions, respectively. The solid curves in this figure define the calculations using (5.14) which are in agreement with the measured data except some deviations around the maximum value. It becomes clear that the coupling efficiency depends mainly on the matching between the field radii of both the optical fiber and the light source which is maximized at 93 % when $w_L = 2.7\,\mu$m which is nearly the same value as w_F and decreases to 79 % when $w_L = 4.1\,\mu$m where a mismatching between the mode field radii of both VCSEL and fiber exists. The dependence of η_m on Δz because the latter is a dominant variable in the spot size i.e. $w_L = w_L(\Delta z)$.
In the case of $8.3\,\mu$m core diameter standard telecommunication SMF for 1300 nm, the given 820 nm range operating wavelengths results in a frequency parameter $\bar{V} = 3.4$.

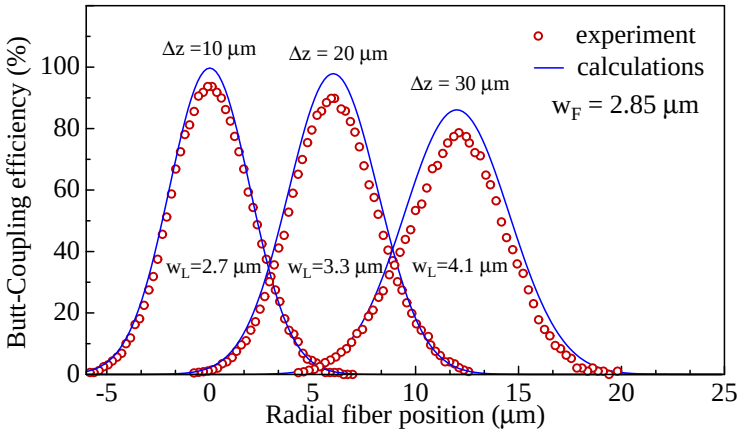


Fig. 5.6: *Dependence of butt-coupling efficiency on lateral displacement Δr for single-mode fiber with mode field radius $w_F = 2.85\,\mu m$ using a VCSEL with mode radii $w_L = 2.7$, 3.2 and 4.1 μm at longitudinal translations between VCSEL and fiber of $\Delta z = 10$, 20, and 30 μm, respectively, where a scale offset is used for $\Delta z = 20$ and 30 μm. The open circles represent the measured data and the solid curves are the calculations using (5.14).*

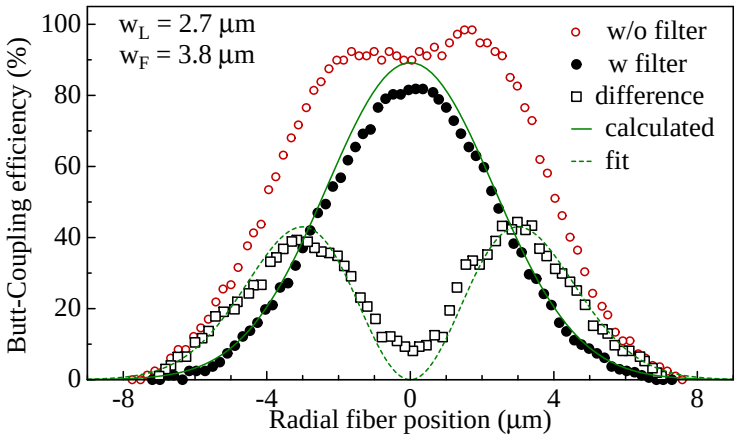


Fig. 5.7: *Dependence of butt-coupling efficiency on lateral displacement Δr for single-mode fiber with mode field radius $w_F = 3.8\,\mu m$ from the same VCSEL of Fig. 5.6 with $w_L = 2.7\,\mu m$ at longitudinal translation $\Delta z = 10\,\mu m$. The measured data are represented by open circles (without filter), closed circles (with filter), and closed squares (the difference in between) whereas the solid curve represent the calculations using (5.14) and the dashed curve represent the fit of the difference to LP_{11} mode profile.*

Step index fibers are single-mode up to $\bar{V} = 2.405$ and are two-mode up to $\bar{V} = 3.83$ value, so that the fiber supports two modes. Mode filtering is realized by macrobending of the fiber as mentioned in section 5.1.4. This filter consists of a fiber loop with 12 mm diameter and 5 windings. The butt-coupling efficiency of this fiber is measured by using the VCSEL of Fig. 5.6 with $w_L = 2.7\,\mu m$ at $10\,\mu m$ distance apart. Figure 5.7 shows the

spatial distribution of η_m where the solid lines represent the calculations using (5.14) along with the field radii of both the optical fiber and VCSEL of 3.8 and 2.7 μm, respectively, open circles represent the measured data without filter, the closed circles represent the measured data using the simple fiber mode filter and the closed squares stand for the difference between the two measured cases. It is seen that measured spatial distribution of η_m without filter is no longer Gaussian and the difference between it and the case with filter can be fitted with LP_{11} mode profile. However, by using the filter the measurements are improved significantly and agree well with the calculations. This idea is also used for 3 Gb/s and 1 Gb/s data transmission experiments with 820 nm single-mode VCSEL over 1300 nm SMF of 4.3 km length [47], [48].

5.2.2 Graded-index multi-mode fiber

Since the main application of the GI multi-mode fiber is the medium-range communications, it is important to study its radial distribution butt-coupling efficiency. The number of bound modes which can propagate in a multi-mode, clad parabolic-profile fiber is given by [33]

$$M = \bar{V}^2/4 \quad . \tag{5.15}$$

Thus, for example, the 50 μm GI fiber with $NA = 0.21$ at 850 nm wavelength has 376 modes. Due to this large number of modes and the large core diameter of this fiber, (5.14) is invalid for calculating butt-coupling efficiency.

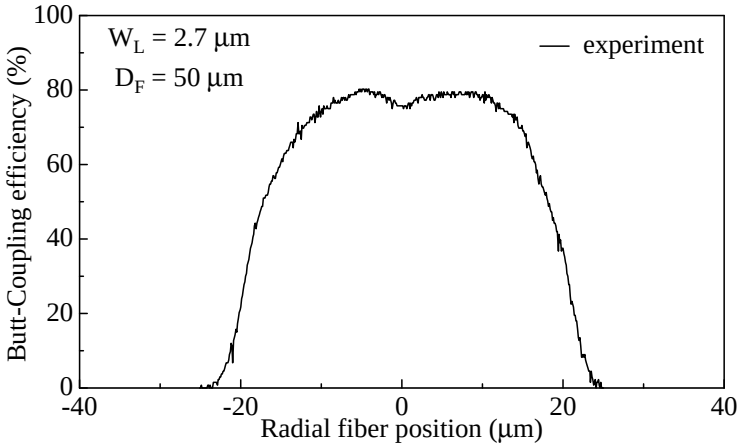


Fig. 5.8: *Measured butt-coupling efficiency at different lateral displacement Δr for 50 μm GI multi-mode fiber using the same VCSEL of Fig. 5.6 with $w_L = 2.7\,\mu m$ at longitudinal translation $\Delta z = 10\,\mu m$.*

Figure 5.8 shows the measured radial distribution of η_m for GI multi-mode fiber using the single-mode VCSEL of Fig. 5.6 with $w_L = 2.7\,\mu$m at longitudinal translation $\Delta z = 10\,\mu$m. As can be seen, η_m has a wide radial tolerance equal nearly the core diameter and has a maximum value of about 80 %. In addition, no optical power propagates in the cladding in contrasy to SMF where approximately 20 % of the tranmitted power exists in the cladding. The dip exists around the central region is probably due to either a defect in the fiber core manufacture or the excitation of the higher order modes of the fiber.

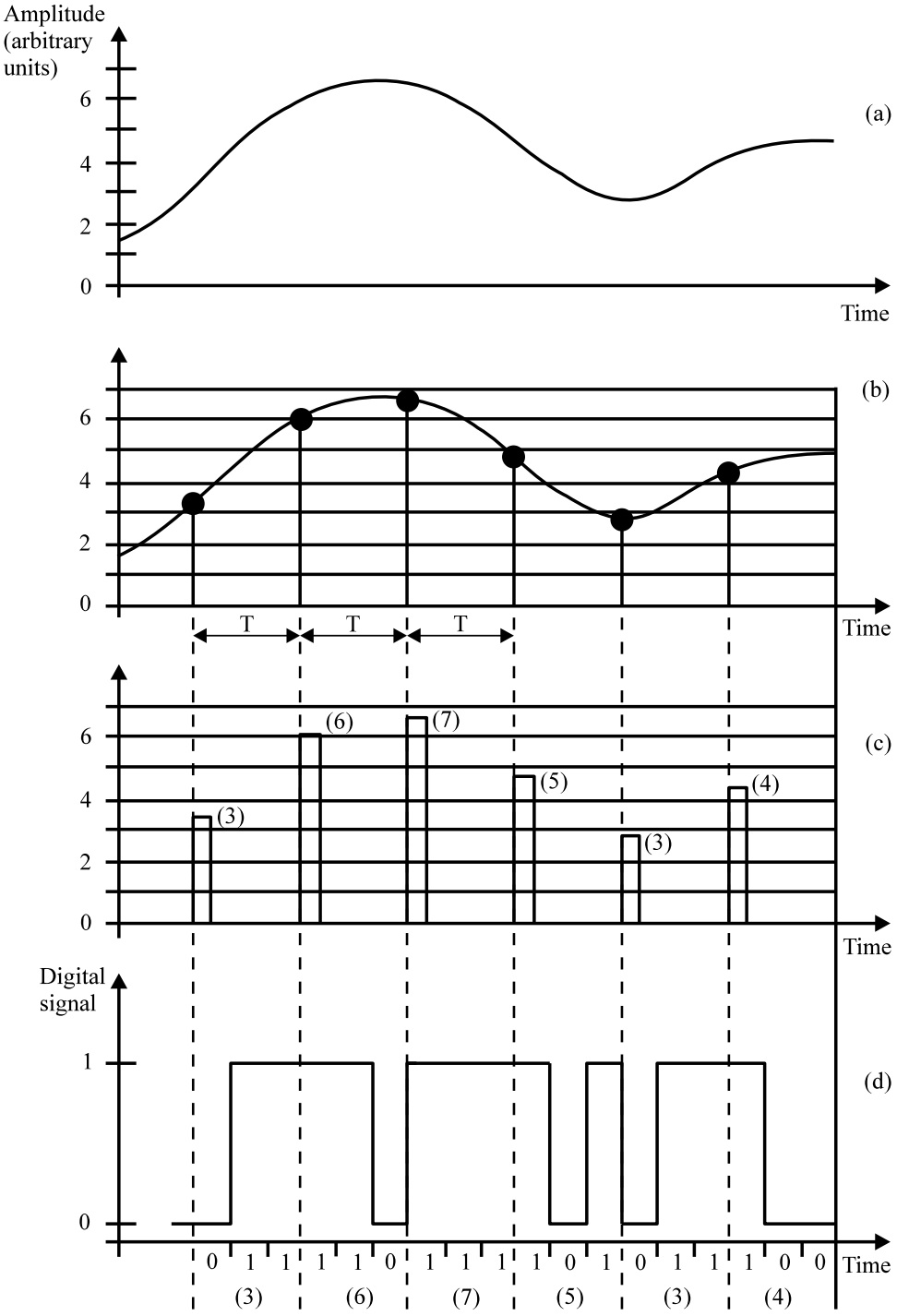
Chapter 6

VCSEL as a Transmitter in Optical Communication Systems

Optical information technology has matured and found practical importance in two areas, namely optical fiber data transmission and compact disk optical storage. It uses a relatively small portion of the whole electromagnetic spectrum between $\lambda = 0.8\,\mu$m and $\lambda = 1.6\,\mu$m. In this range Silica fibers have extremely small losses of less than 1 dB/km which is to be compared to the attenuation in coaxial cables of about 20 dB/km at radio frequencies of 100 MHz. A light source of great scientific and commercial interest is the vertical-cavity surface-emitting laser (VCSEL) because it offers a number of favorable properties like low lasing threshold current [49], dynamic single-mode operation [50], low divergence circular beams [42], high packing density [51], and high-speed current modulation for multi-Gb/s data generation [52]. Despite these attractive features, the complex transverse modal behavior of VCSELs at high pump rates and large active diameters is a major drawback mainly in datacom applications. The mode dynamics are strongly dependent on the spatial carrier distribution which itself is governed by the influence of pump induced current spreading, hole burning, and thermal gradients in the laser cavity [53], [54]. The details of the transverse mode pattern in the device are of concern especially for fiber coupling where today both single-mode and multi-mode VCSEL approaches are followed in combination with a graded-index multi-mode fiber (MMF). In addition, the laser turn-on event depends on the driving current and consequently can be expected to be influenced by the transverse mode structure of the device. In this chapter, some system aspects of an optical signal transmission channel will be considered. Moreover, near-field measurements will be employed to investigate the spectral and spatial intensity distributions of transverse modes in VCSELs with 4 and 6 μm active diameters during turn-on. The same approach will be used to perform bit error measurements at moderate bit rates of 1 and 2.5 Gb/s for different lateral fiber coupling offsets.

6.1 Requirements on Information Transmission

Optical signals are usually transmitted in digitally encoded form. Fig. 6.1 illustrates the conversion of an arbitrary analog waveform into a binary digital signal.



Steps in the conversion of an analog waveform into a binary digital signal :
(a) part of an analog waveform ;
(b) analog waveform sampled at time intervals of T ;
(c) the sampled waveform showing allocation of amplitude to one of $2^3 = 8$ levels ;
(d) sampled information converted to binary digital form with 3 bits/sample.

Fig. 6.1: *Conversion of an analog signal into a binary digital signal.*

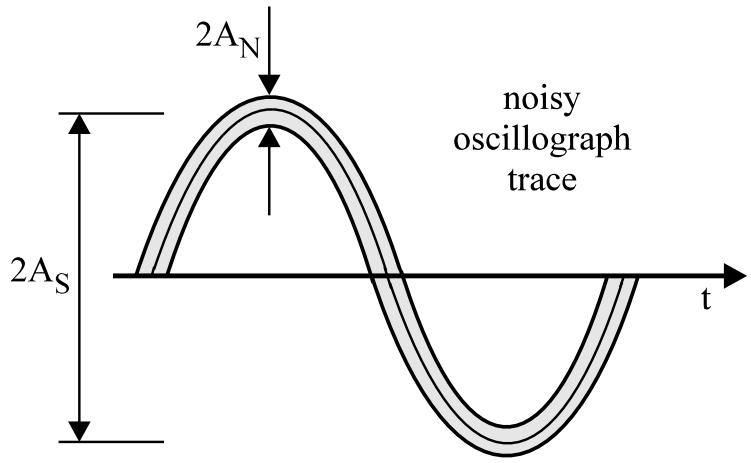


Fig. 6.2: *Noisy waveform*

The first step is to sample the signal at discrete equidistant intervals of time, where the sampling period is T. According to the sampling theorem it is necessary that the sampling frequency $f_{\text{samp}} = 1/T$ should be larger than twice the highest frequency f_{max} contained in the original waveform to be able to fully recover the original waveform. The frequency f_{max} is often referred to as the bandwidth of the signal. The sampling theorem requires

$$f_{\text{samp}} \quad > \quad 2\ f_{\text{max}} \quad . \tag{6.1}$$

If this so-called Nyquist condition is met one may put the sampled waveform through an ideal low-pass filter with corner frequency f_{max} to obtain the original signal at the output of the filter. The next step is to allocate each sampled level to one of a finite number of amplitude levels. This process is called quantization. In reality there are always random fluctuations superimposed on the intended waveform. This system noise makes it unprofitable to attempt to distinguish between amplitude levels that are smaller than the standard deviation of the noise. Fig. 6.2 represents a noisy waveform with maximum signal amplitude A_S and root mean square (r.m.s.) noise amplitude A_N. The dynamic range

$$D = A_S/A_N \tag{6.2}$$

determines the number of levels needed to give a sufficiently precise representation of the original waveform. Let m denote the smallest integer larger or equal to D, i.e.

$$m = [D] \ . \tag{6.3}$$

Then each sampled level requires

$$M \ = \ \log_2 \ m \tag{6.4}$$

binary digits to encode it. The lower part of Fig. 6.1 shows how the sampled waveform is encoded in simple binary form. When the binary digital signal is decoded back to reproduce the original waveform, the errors produced by the quantization of the sampled amplitudes lead to additional noise, known as quantization noise. It can be shown that the quantization noise is comparable to or less than the original noise of the waveform if

$$m = [D] \;\geq\; \left(1 + \frac{A_S^2}{A_N^2}\right)^{1/2} \quad . \tag{6.5}$$

Therefore, the reproduction of the original analog waveform of bandwidth $f_{\max}$ and dynamic range D requires a minimum of B binary digits per second, where

$$\begin{aligned} B \;=\; 2\; f_{\max}\; M \quad &= \quad 2 f_{\max} \log_2 \left(1 + \left(\frac{A_S}{A_N}\right)^2\right)^{1/2} \\ &= \quad f_{\max} \log_2 \left(1 + \frac{A_S^2}{A_N^2}\right) \; . \end{aligned} \tag{6.6}$$

The unit of B is bit/s. B is referred to as channel capacity. It denotes the minimum bit rate to digitally transmit an analog waveform without excessive quantization noise.
A communication channel which is able to transmit analog signals of bandwidth $f_{\max}$ and signal-to-noise ratio A_S/A_N is said to have a channel capacity of B, where B is given by formula (6.6). This formula originally given by Shannon is used for the comparison of the information capacity of different communication channels. In any case, the transmission rate has to be proportional to the bandwidth of the signal being sent and the logarithm of the minimum signal-to-noise ratio. Often, higher bit rates than required from (6.6) are transmitted. This redundancy leads to an information content that is smaller than the channel capacity.
In practical systems a large signal-to-noise ratio is required, i.e. $A_S \gg A_N$, resulting in

$$B = 2 f_{\max} \log_2 (A_S/A_N) \; . \tag{6.7}$$

The signal-to-noise ratio is often given in decibel according to

$$\frac{S/N}{[\mathrm{dB}]} \;=\; 10 \log_{10} \frac{A_S^2}{A_N^2} \;=\; 20 \; \log_{10} \frac{A_S}{A_N} \tag{6.8}$$

As $\log_2 10 = 3.32$, one obtains the useful relation

$$\frac{B}{[\mathrm{bit/s}]} \;=\; 0.332 \; \frac{S/N}{[\mathrm{dB}]} \; \frac{f_{\max}}{[\mathrm{Hz}]} \tag{6.9}$$

for the channel capacity.

6.2 Optical Fiber Communication Systems

An Optical Transmission System (OTS) consists of transmitter, transmission medium, and receiver. The system in Fig. 6.3 contains a laser diode source, an optical fiber for guiding the light, and a photodiode for converting optical information into electrical signals.

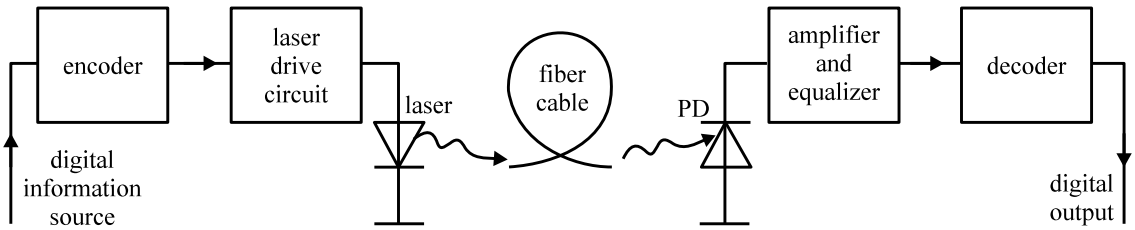


Fig. 6.3: *Optical fiber communication system.*

6.2.1 Properties of optical information transmission systems

Optical information transmission systems have a number of advantages compared to their electrical counterparts including the following:

1. Bandwidth
   Optical carrier frequencies in the range from 10^{13} to 10^{16} Hz, usually around 10^{14} Hz in the infrared spectral region, offer much higher potential bandwidths compared to electrical cables. Due to increasing attenuation with increasing frequency, transmission in coaxial cables is limited to frequencies below about 1 GHz, thus setting the limit for the transmission bandwidth. Today's optical fiber transmission systems operate already at 2.5 or 10 Gbit/s and accordingly exceed electrical systems. Attenuation in fibers is much less than in coaxial cables allowing considerably larger distances between repeaters for long haul transmission.

2. Size and weight
   Compared to copper cables, optical fibers even with protective coatings are thin and light. In congested ducts in cities one can put fibers instead of copper to expand signal transmission. The small weight is advantageous for signal transmission in mobile systems such as aircrafts, cars, or ships.

3. Electrical isolation
   Optical fibers are fabricated from glass or sometimes plastic polymer being electrical isolators. Thus earth loops and electrical potential problems at interfaces do not arise.

4. Immunity to interference and crosstalk
   Optical transmission in fibers is essentially free from electromagnetic interference (EMI), radiofrequency interference (RFI), or switching transients giving electromagnetic pulses (EMP). No shielding is required. As the transmitted signal is strictly confined to the fiber, crosstalk between fibers or to the environment is negligible.

5. Signal security
   As the light is confined to the fiber and does not radiate, a transmitted signal cannot be obtained from a fiber in a non-invasive manner. This is an attractive aspect for transmitting sensitive data.

6.2.2 Noise sources in optical tansmission systems

In optical transmission systems, there are three major noise sources:

1. **Transmitter noise:**
   The relative intensity noise (RIN) generated in the optical device relates the photon density fluctuations to the mean photon density squared by [55]

$$RIN(\nu) = 2\,\frac{\langle|\Delta\widetilde{N}(\nu)|^2\rangle}{\langle N\rangle^2}\ , \tag{6.10}$$

   where the angular brackets denote an average over the observation time and RIN(ν) is measured in dB/Hz.
   The intensity noise of the total light output of laser diodes is relatively low, however, the partition of different lasing modes in the total light output fluctuates considerably, yielding the so called mode partition noise.

2. **Transmission channel noise:**
   It depends on the properties of the optical fiber link like, coupling efficiency, mode dispersion, and sometimes disturbance in core refractive index.

3. **Receiver noise:**
   In this case, there are various sources of noise that add to the signal current and critically depend on the bandwidth $\Delta\nu$ of the measuring system [1]:
   - The drift of charge carriers through the depletion region of the photodiode makes a contribution to the shot noise

$$\langle\delta i_s^2\rangle \;=\; 2q\,\langle i_{ph}\rangle\,\Delta\nu, \tag{6.11}$$

     where it depends on the elementary charge q and the mean photo current i_{ph}.

- Even without light irradiation, charge carriers excited by thermal background radiation traverse the depletion layer and cause a dark current i_D, and consequently produce the shot noise

$$\langle \delta i_d^2 \rangle \ = 2q \ i_D \ \Delta\nu \ . \tag{6.12}$$

- Finally, there is also a contribution from the thermal noise of the load resistance R_L

$$\langle \delta i_t^2 \rangle \ = 4kT\Delta\nu / R_L \ . \tag{6.13}$$

The total noise is a superposition of these sources and is therefore given by

$$\langle \delta i_{tot}^2 \rangle = \langle \delta i_s^2 \rangle + \langle \delta i_d^2 \rangle + \langle \delta i_t^2 \rangle \tag{6.14}$$

6.2.3 Detection sensitivity for digital signal

A binary optical signal is simply defined according to Fig. 6.4 produces two discrete photocurrents $\langle i_0 \rangle$ and $\langle i_1 \rangle$. The mean value $\langle i_0 \rangle$ represents the logical zero, whilst $\langle i_1 \rangle$ stands for the logical unity. The photocurrent signal varies about the respective mean values $\langle i_1 \rangle$ and $\langle i_0 \rangle$, due to the reciever noise mentioned just before and also the statistical nature of the radiation incident on the detector. However, in practice the photon noise is small compared with the receiver noise. As a result, only the latter will be taken into account for calculating the bit error rate (BER) of both zero and one logics. The period T of the rectangular time signal defines the bit rate $B = 1/T$. In order to estimate the noise, a receiver with ideal low-pass characteristics

$$H(\nu) = \begin{cases} 1 & \text{for} \quad -B/2 \leq \nu \leq B/2 \\ 0 & \text{otherwise} \end{cases} \tag{6.15}$$

is assumed. The variance of the input noise current δi_{tot} is given by integration of the spectral power (6.14) as

$$\langle \delta i_{tot}^2 \rangle = \int_0^{B/2} \langle \delta i_{tot}^2(\nu) \rangle d\nu = q \ i_{ph} \ B + q \ i_D \ B + 2kTB/R_L \quad . \tag{6.16}$$

For simplicity, the instantaneous value of the current i is assumed to have a Gaussian distribution about the mean value $\langle i_0 \rangle$ or $\langle i_1 \rangle$ for logical zero or logical unity, respectively. The probability density for a logical zero is therefore

$$p_0(i) = \frac{1}{\sqrt{2\pi \langle \delta i_{tot}^2 \rangle}} \exp\left\{ -\frac{(i - \langle i_0 \rangle)^2}{2\langle \delta i_{tot}^2 \rangle} \right\} \ , \tag{6.17}$$

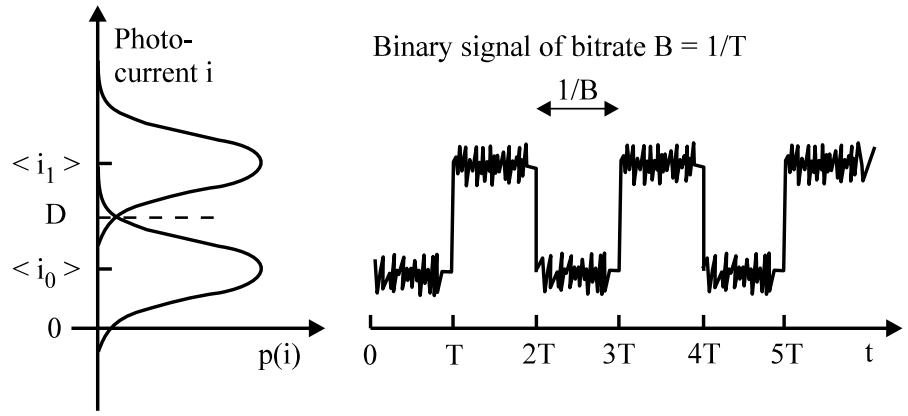


Fig. 6.4: *Noisy photocurrent signal with bit rate B and distribution $p(i)$ of the instantaneous current values about the logic levels $\langle i_0 \rangle$ and $\langle i_1 \rangle$.*

and for a logical unity

$$p_1(i) = \frac{1}{\sqrt{2\pi\langle \delta i_{tot}^2 \rangle}} \exp\left\{ -\frac{(i - \langle i_1 \rangle)^2}{2\langle \delta i_{tot}^2 \rangle} \right\} \ . \tag{6.18}$$

If, as is usually the case, logical zeros and logical unities are sent on average equally frequently, the time-averaged value of the current is given by

$$D = (\langle i_1 \rangle + \langle i_0 \rangle)/2 \ . \tag{6.19}$$

This value is defined as the decision threshold. For $i \leq D$ a logical zero is assigned to the detected signal. The probability of a false assignation is determined by the BER for the logical zero

$$\mathrm{BER}_0 = \int_D^\infty p_0(i) di = \frac{1}{\sqrt{2\pi}} \int_Q^\infty \exp\{-u^2/2\} du \ , \tag{6.20}$$

where the abbreviation $u = (i - \langle i_0 \rangle)/\sqrt{\langle \delta i_{tot}^2 \rangle}$ and the noise related level separation

$$Q = (\langle i_1 \rangle - \langle i_0 \rangle) \Big/ \left(2\sqrt{\langle \delta i_{tot}^2 \rangle} \right) \ , \tag{6.21}$$

are used. Q can be considered as the signal amplitude measured in units of the average noise level. Under the assumptions made one can easily show that the BER for the logical unity is just as great as for the logical zero

$$\mathrm{BER}_1 = \int_{-\infty}^D p_1(i) di = \mathrm{BER}_0 = \mathrm{BER} \ . \tag{6.22}$$

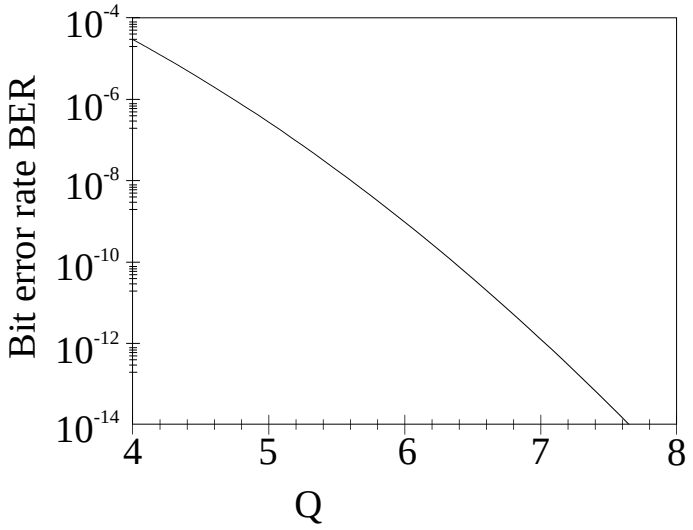


Fig. 6.5: *Bit error rate BER as a function of the noise related level separation Q.*

Accordingly the BER is given quite generally by

$$\mathrm{BER} = \frac{1}{\sqrt{2\pi}} \int_Q^\infty \exp\{-u^2/2\} du \approx \frac{1}{\sqrt{2\pi}Q} \exp\left\{-\frac{Q^2}{2}\right\} \left(1 - \frac{1}{Q^2}\right) \ . \tag{6.23}$$

The error in the approximation is smaller than one percent when $Q > 2$. The connection between the BER and the parameter Q is shown in Fig. 6.5. For example, when $Q = 6$ the BER $= 10^{-9}$, and when $Q = 7$ the BER $\approx 1.3 \cdot 10^{-12}$. Equation (6.21) can be transformed still further. The decision threshold D can be expressed in terms of the time-averaged optical power $\eta\langle P\rangle$ converted into the photocurrent

$$D = \frac{\langle i_1\rangle + \langle i_0\rangle}{2} = \eta \frac{q}{\hbar\omega} \langle P\rangle \quad , \tag{6.24}$$

and form the on/off-ratio

$$r_{10} = \langle i_1\rangle / \langle i_0\rangle \quad . \tag{6.25}$$

For a specified BER, the optical power needed in a binary signal is

$$\eta\langle P\rangle = \frac{\langle i_1\rangle + \langle i_0\rangle}{\langle i_1\rangle - \langle i_0\rangle} \frac{\hbar\omega}{q} Q \sqrt{\langle \delta i_{tot}^2 \rangle} \quad . \tag{6.26}$$

This quantity is called the receiver sensitivity and is optimal if the transmitted optical power for the logical zero and hence $\langle i_0\rangle$ vanishes. By using (6.25) into (6.26), the reciever sensitivity can be re-expressed as

$$\eta\langle P\rangle = \frac{r_{10}+1}{r_{10}-1}\frac{\hbar\omega}{q}Q\sqrt{\langle\delta i_{tot}^2\rangle}\ . \tag{6.27}$$

6.2.4 Eye diagram

A method which is often employed to obtain a qualitative indication of the performance of a PCM transmission system is the examination of the received waveform on an oscilloscope using a sweep rate which is a fraction of the bit rate of a random pulse sequence. The display observed over two bit intervals duration, which is the result of superimposing all possible pulse transitions, is called an eye pattern or an eye diagram. Fig. 6.6 illustrates an eye diagram for a binary signal with little distortion. It is observed that the pattern has the shape of a human eye which is open and that the decision time corresponds to the center of the opening. To regenerate the pulse sequence without error the eye must be open. The decision level and the decision time must lie in this open area. Noise and intersymbol interference may close the eye. Fluctuations of the bit rate or jitter of the sampling time similarly have a degrading effect on the BER characteristics. Typical bit error rates of BER = 10^{-9} are tolerated in optical communications. However, for data exchange between computers which is increasingly being performed with optical busses more stringent requirements of BER = 10^{-15} are needed.

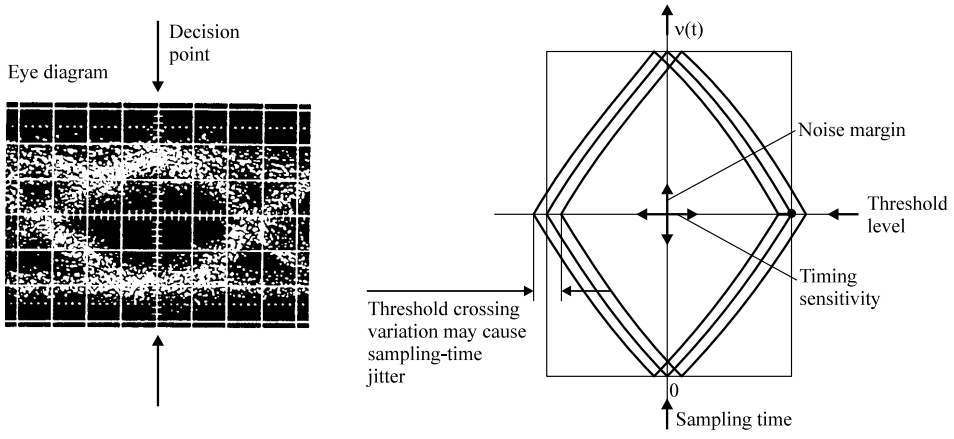


Fig. 6.6: *Eye pattern of a random PCM sequence.*

6.3 Dynamic behavior of VCSELs

Applications of VCSELs in data transmission systems rely on the dynamic and noise properties of the source. These characteristics are generally obtained from rate equations

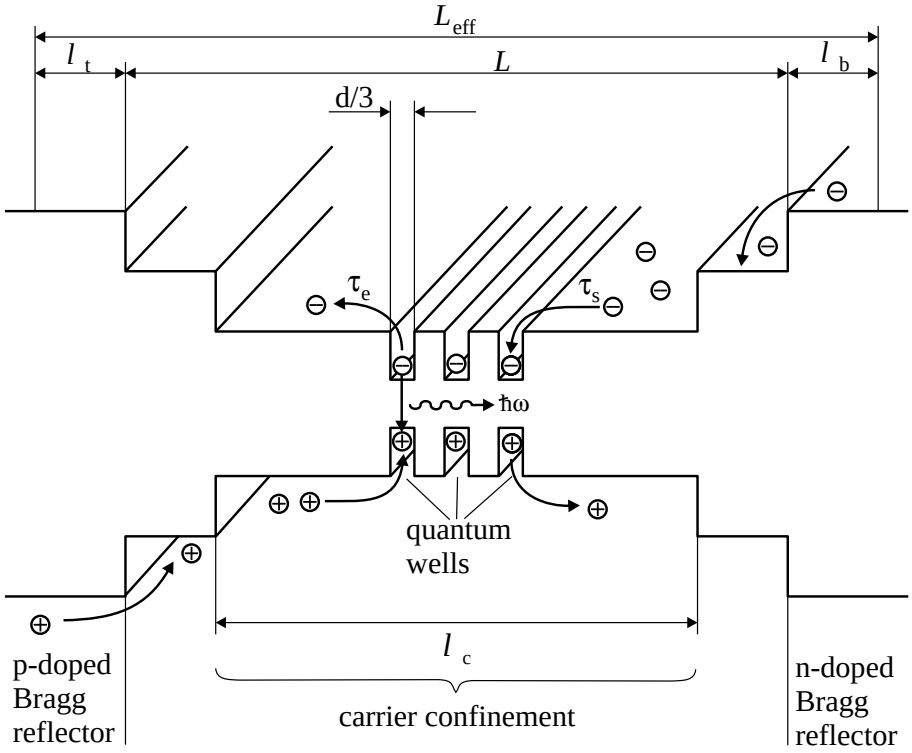


Fig. 6.7: *Dynamic model of a VCSEL active region, indicating electron injection into barriers as well as diffusion into and escape from the quantum wells.*

[1], [6] describing the interaction of electrons and photons in the laser cavity. Dynamic behavior is most easily inferred from the small signal current modulation transfer function. Noise originates from spontaneous emission whose statistic nature is expressed in the rate equations by Langevin forces for carriers and photons, especially leading to the relative intensity noise spectrum. For simplicity, single-mode laser will be considered.

6.3.1 Rate equations

A schematic model of an ideal VCSEL with three quantum wells is illustrated in Fig. 6.7. It is similar to that of Fig. 2.6, but in this case it describes the dynamic state of VCSEL. An external current source provides the barriers of volume $V_{\mathrm{b}} = A_{\mathrm{act}} \cdot (l_{\mathrm{c}} - d)$ with current I. The rate of change of the electrons density n_{b} in these barrieres is given by

$$\frac{dn_{\mathrm{b}}}{dt} = \frac{I}{qV_{\mathrm{b}}} + \frac{n_{\mathrm{w}}}{\tau_{\mathrm{e}}}\frac{V_{\mathrm{w}}}{V_{\mathrm{b}}} - \frac{n_{\mathrm{b}}}{\tau_{\mathrm{s}}} - \frac{n_{\mathrm{b}}}{\tau_{\mathrm{sp,b}}} \quad . \tag{6.28}$$

The different terms in the right hand side of this equation represent respectively the external electron density from the current source, the escape of carriers from the wells

of volume $V_\mathrm{w} = A_\mathrm{act} \cdot d$ and of electron density n_w into the barriers with τ_e, the carriers diffusion into undoped potential wells [56] with a transport time τ_s, and finally the removed carriers from the barriers by spontaneous emission with time constant $\tau_\mathrm{sp,b}$. Carriers captured in the well can take part in emission and absorption transitions. Spontaneous emission is characterized introducing the carrier lifetime $\tau_\mathrm{sp,w}$ and the statistical nature of spontaneous emission events require a Langevin force $F_\mathrm{n}(t)$. Stimulated emission processes depend on the modal material gain coefficient $g_\mathrm{p}(n_\mathrm{w})$ and the photon density N in the mode under consideration. Since the position of the quantum wells relative to the standing wave pattern in the cavity is very important as has been mentioned in Sect. 2.5, the relative confinement factor Γ_r has to be considered in the stimulated emission processes. Hence the well electron rate equation is written as

$$\frac{dn_\mathrm{w}}{dt} = \frac{n_\mathrm{b}}{\tau_\mathrm{s}}\frac{V_\mathrm{b}}{V_\mathrm{w}} - \frac{n_\mathrm{w}}{\tau_\mathrm{e}} - \frac{n_\mathrm{w}}{\tau_\mathrm{sp,w}} - \frac{\Gamma_\mathrm{r}\, v_\mathrm{gr}\, g_\mathrm{p}(n_\mathrm{w})}{1+\varepsilon N} + F_n(t) \quad . \tag{6.29}$$

where v_gr is the group velocity. The modal material gain coefficient is given by (2.15). Gain compression [57] due to effects like carrier leakage by heating, or spatial hole burning by photons is accounted by the denominator $1 + \varepsilon N$. The gain compression parameter ε is estimated from [58]

$$\varepsilon = \frac{\lambda^2 c \tau_\mathrm{intra}^2}{2\pi \bar{n}^3 \tau_\mathrm{sp,w}} \quad , \tag{6.30}$$

where c is the vacuum velocity of light and $\tau_\mathrm{intra} \approx 100\,\mathrm{fs}$ is the intraband relaxation time. In the photon rate equation

$$\frac{dN}{dt} = \bar{\beta}_\mathrm{sp}\frac{V_\mathrm{w}}{V_\mathrm{p}}\frac{n_\mathrm{w}}{\tau_\mathrm{sp,w}} - \frac{N}{\tau_\mathrm{p}} + \frac{V_\mathrm{W}}{V_\mathrm{p}}\frac{\Gamma_\mathrm{r}\, g_\mathrm{p}(n_\mathrm{w}) N\, v_\mathrm{gr}}{1+\varepsilon N} + F_N(t) \tag{6.31}$$

cavity losses described by a photon lifetime τ_p and stimulated as well as spontaneous emission are important. The statistical nature of spontaneous emission is suitably accounted for by a photon Langevin force $F_N(t)$. From the total number of spontaneuos emission events only the fraction given by the spontaneous emission coefficient $\bar{\beta}_\mathrm{sp}$ will go into the mode of interest [59]. Furthermore, for density related equations the ratio of well volume V_w for interacting electrons and cavity volume V_p for interacting photons comes into play. This ratio is also important for the stimulated emission rate. The electron rate equations (6.29) and (6.28) as well as the photon rate equation (6.31) govern dynamics and noise of quantum well VCSELs.

6.4 Transverse Mode Turn-On Dynamics

6.4.1 Device structure and output characteristics

The layer structure of the selectively oxidized top-emitting VCSELs used in this work is grown by solid source molecular beam epitaxy. The active region is formed by three 8 nm thick GaAs quantum wells embedded in $Al_{0.2}Ga_{0.8}As$ barriers for about 850 nm gain peak wavelength. The carbon doped p-type and silicon doped n-type Bragg reflectors consist of 19 and 35.5 $Al_{0.1}Ga_{0.9}As/Al_{0.9}Ga_{0.1}As$ pairs, respectively. For lateral current confinement, a single 25 nm thick AlAs layer is placed in the first quarter wavelength layer above the active zone and is subsequently oxidized after a mesa etching process. In Fig. 6.8 the light output characteristics of 4 μm (solid curves) and 6 μm (dashed curves) aperture diameter selectively oxidized VCSELs are depicted. The smaller device has a threshold current of 0.7 mA and emits in a single mode, as shown in Fig. 6.9(b). The threshold current of the larger device is 1.1 mA and it oscillates on the fundamental mode up to 1.5 mA, then becomes multi-mode for higher currents as illustrated in Fig. 6.9(d).

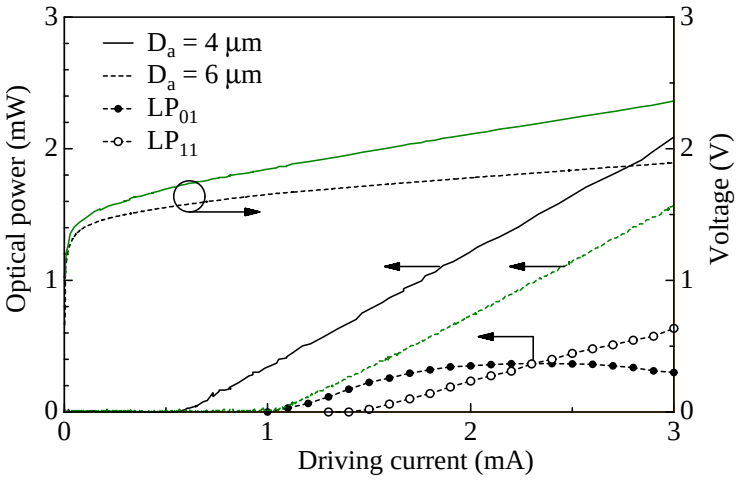


Fig. 6.8: *Light-current and current-voltage characteristics of 4 μm (solid curves) and 6 μm (dashed curves) aperture oxide-confined VCSELs. The closed and open circles define the peak spectral power emitted from the larger device in the LP_{01} and LP_{11} modes, respectively.*

The near-field measurement setup mentioned in chapter 3 is used to analyze the spatial profiles of the lasing modes. Fig. 6.9(a) shows a transverse central cross-section of the measured near-field intensity profile of the Gaussian-like transverse fundamental LP_{01} mode (solid circles) for the VCSEL with active diameter $D_a = 4\,\mu$m at 2 mA bias current and 300 mV modulation voltage of a 1 Gb/s data rate pseudo-random bit sequence (PRBS)

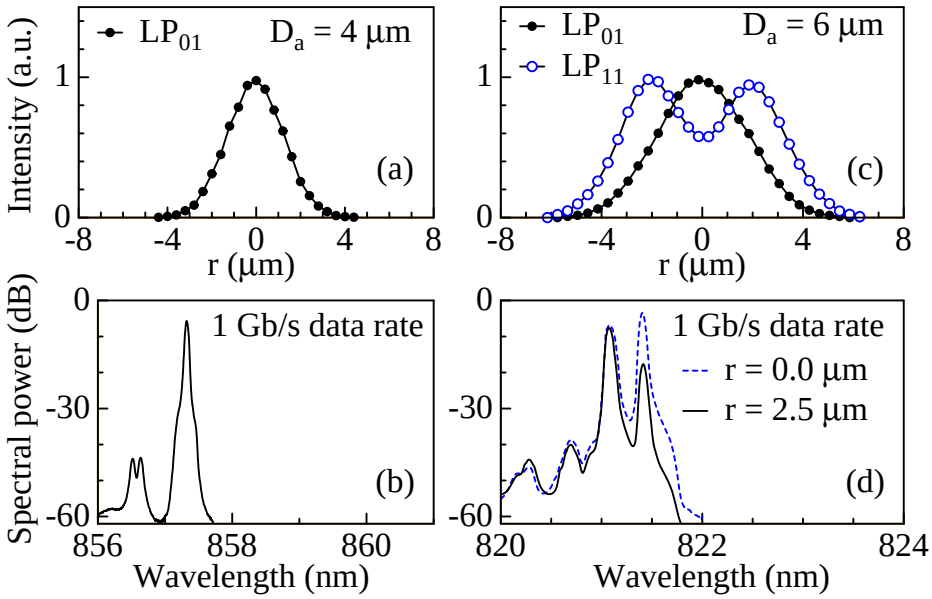


Fig. 6.9: *Spatial intensity distribution and emitted spectrum of a 4 µm aperture device at 2 mA bias current and 300 mV modulation voltage (a) and (b). The results of the same measurements on a 6 µm aperture device at 2 mA bias current and 150 mV modulation voltage are displayed in (c) and (d), where the additional spectrum in (d) is taken for* 2.5 *µm radial fiber offset.*

signal. Under these conditions, emission is single-mode with a sidemode suppression ratio of better than 30 dB, as illustrated in Fig. 6.9(b). The same measurements for the VCSEL with $D_a = 6\,\mu$m at 2 mA bias current and 150 mV modulation voltage are illustrated in Fig. 6.9(c). In this case the increase of the active diameter leads to the excitation of both LP_{01} mode (solid circles) and the higher order transverse LP_{11} mode (open circles). Both modes are circularly symmetric with the LP_{11} mode exhibiting an intensity dip in the center of the cavity. The emission spectrum in Fig. 6.9(d) shows that the LP_{11} mode is blue shifted from the LP_{01} mode by 0.4 nm.

6.4.2 Turn-on delay

The rate equations (6.28), (6.29), and (6.31) are solved numerically [60] for a VCSEL with 3 μm active diameter and the results are summarized in Fig. 6.10. It shows the development of the carrier and photon densities with time when the VCSEL device is modulated with an electric square pulse of $I_{\mathrm{on}} = 1.8 \cdot I_{\mathrm{th}}$. The electron density at first increases from its initial value to about threshold density $n_{w,th}$. Laser emission starts only when the threshold is reached after a time delay t_d. After that a very small interval of time in the range between 50 and 100 ps [60] is required to build the resonator. This time is called resonator built-up time t_{on}. The modal power shows damped relaxation

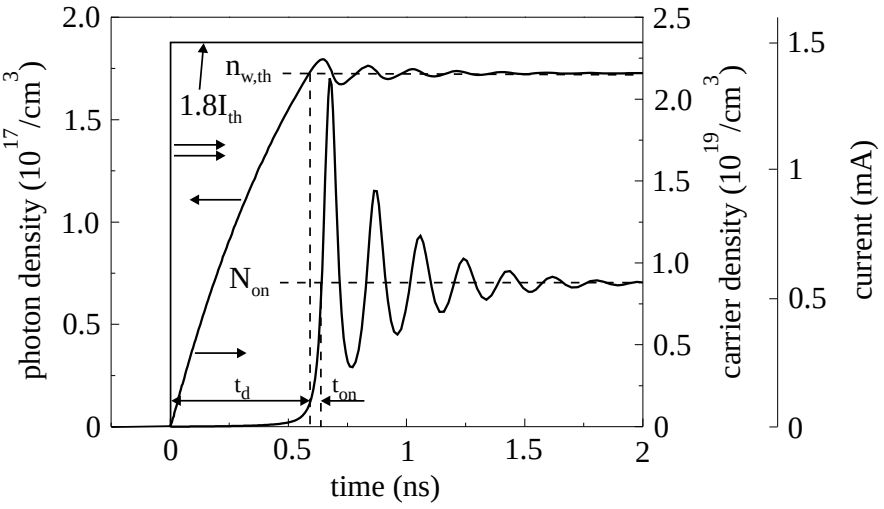


Fig. 6.10: *Simulations of time development of the photon density N and the electron density n after after an instantaneous change of the pumping current from* $I_{\text{off}} = 0$ *to* $I_{\text{on}} = 1.8 \cdot I_{\text{th}}$ *(from [60]).*

oscillations due to the presense of like oscillations in the carrier density. The time delay t_d can be obtained from the rate equation (6.29) from the position that stimulated process initially play no part [1] and under the boundary condition $n(t = 0) = 0$ or $I_{\text{off}} = 0$ is given by

$$t_d = \tau_{\text{sp,w}} \cdot \ln\left[\frac{I_{\text{on}}}{I_{\text{on}} - I_{\text{th}}}\right] \quad . \tag{6.32}$$

In general, the delay time can be shortened if the laser is biased at the current I_{off} just below the threshold and then eq. 6.32 has the form

$$t_d = \tau_{\text{sp,w}} \cdot \ln\left[\frac{I_{\text{on}} - I_{\text{off}}}{I_{\text{on}} - I_{\text{th}}}\right] \quad . \tag{6.33}$$

To measure the time delay, the setup in Fig. 6.11 is used. The VCSEL is contacted with the inner conductor of SMA-box through a gold bond wire of length $\approx 2\,\text{mm}$. Bias dc current and modulation signal from the pulse generator[1] are combined in a bias-tee[2] and fed to the VCSEL. The optical fiber is butt-coupled to the VCSEL and connected via an optical attenuator to the sampling optical oscilloscope[3] with 20 ps pulse rise time, 17 GHz bandwidth, and 10 nW sensitivity [61]. The left part of Fig. 6.12 shows the measured optical optical signal over 1 ns when the $4\,\mu$m aperture VCSEL is modulated with a large fignal with amplitude $V_{\text{pp}} = 2\,\text{V}$ at a frequency of 1 GHz (thick curve) and

[1] Anritsu Pulse Generator MP1652A, max. 3 GHz
[2] Picosecond Pulse Labs, 5550B
[3] Hamamatsu OOS-01/IR

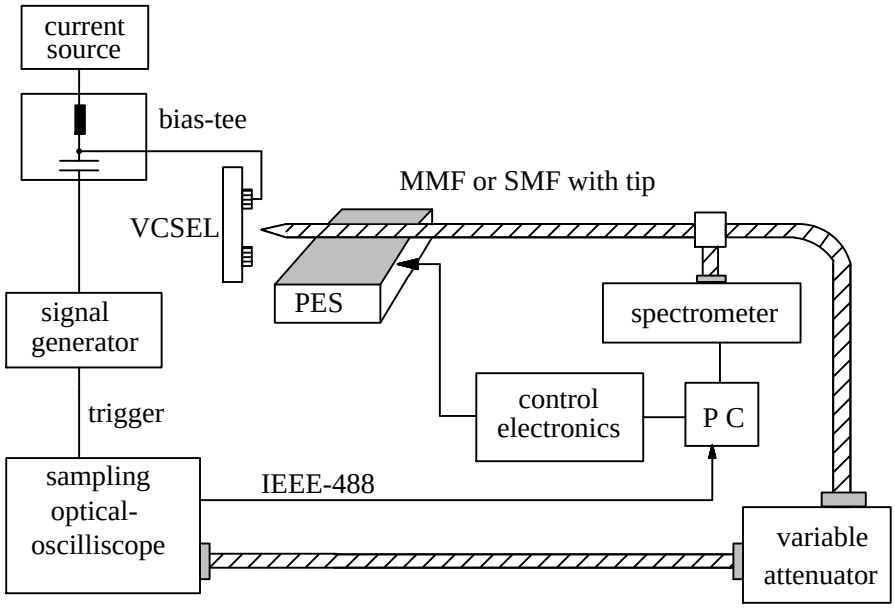


Fig. 6.11: *Setup for time delay experiment.*

along with a bias current $I_{\text{off}} = I_{\text{th}}$ (thin curve). It is seen that without bias current the device begins to lase after the delay time $t_d = 0.18\,\text{ns}$. Also, the modal power shows the typical damped relaxation oscillations as the calculated ones in 6.12. These relaxation oscillations are reduced and the delay time reaches zero when the VCSEL device is biased at $I_{\text{off}} = I_{\text{th}}$. After switching off the VCSEL in both cases, there are still carriers which can contribute to the stimulated emission after diffusing into the active region, yielding the tail in the light output pulse. The right part of Fig. 6.12 depicts the measured time delay for differeent modulation signals (open circles) compared with the calculated values (solid curve) using eq. (6.33) along with $\tau_{\text{sp,w}} = 0.8\,\text{ns}$. These measurments are in agreement with the calculations and the value of $\tau_{\text{sp,w}}$ is nearly the same as that obtained in ref. [60]. To measure the optical pulse at different lateral position, the same setup of Fig. 6.11 is used where the near field setup is already installed. The single-mode fiber (SMF) with tip is used for this purpose. Both single-mode and two-mode VCSELs of Fig. 6.8 are modulated with the same rectangular signal of 1 GHz frequency and 2 V amplitude without bias current. The results are shown in Fig. 6.12. As can be seen in the left part, the optical pulse of single-mode VCSEL looks the same over the time domain as the SMF fiber moves from the center at the radial position $r = 0$ to the edge at the radial position $r = 2\,\mu\text{m}$. In contrast, the optical pulse of the two-mode VCSEL in the right part shows a significant difference due to the different lateral distributions of both LP_{01} and LP_{11} modes. As the SMF moves from the center up to the radial position $r = 2\,\mu\text{m}$, both LP_{01} and LP_{11} modes are coupled into the fiber and the optical pulse shows nearly a constant

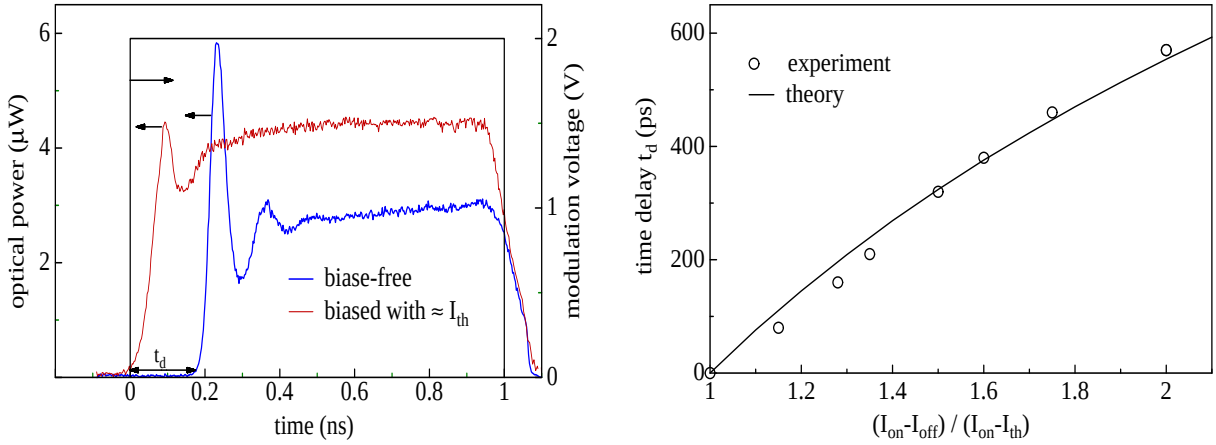


Fig. 6.12: *The left part represent the measured optical output pulse for single-mode VCSEL with 4 μm active diameter under modulation with rectangular electric pulse of 1 GHz frequency and amplitude $V_{\rm pp} = 2$ V (thick curve) and with the same signal along with bias current $I_{\rm off} = I_{\rm th}$ (thin curve). The right part represent the measured time delay t_d in relation with $\left[\frac{I_{\rm on}-I_{\rm off}}{I_{\rm on}-I_{\rm th}}\right]$ (open circles) copmared with the calculations (solid curve) using (6.33).*

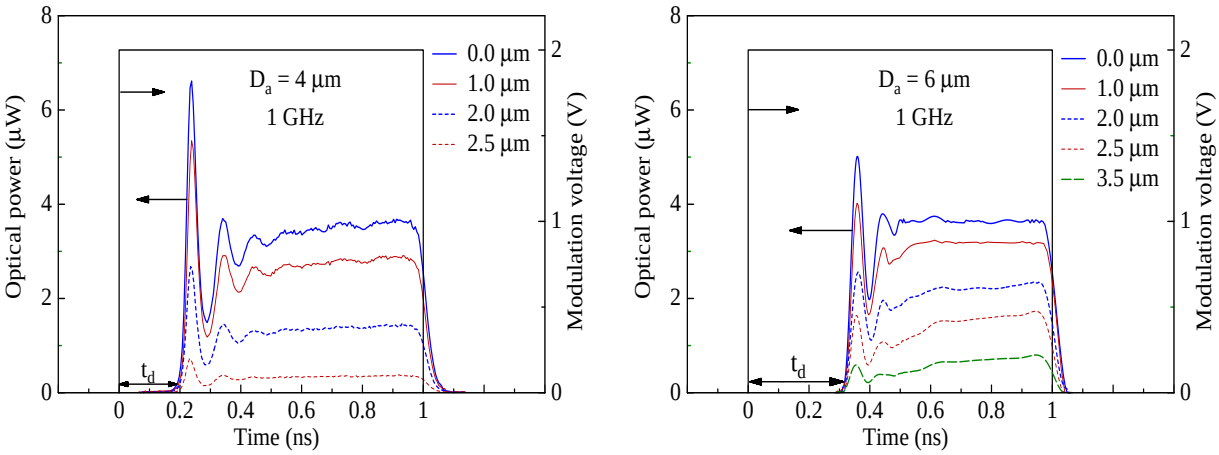


Fig. 6.13: *Optical output pulse at different lateral positions for single-mode VCSEL with 4 μm active diameter (left) and two-mode VCSEL with 6 μm active diameter (right). These VCSELs are modulated with rectangular electric pulse of 1 GHz frequency and amplitude $V_{\rm pp} = 2$ V.*

value after the initial relaxation oscillations. From $r = 2.5\,\mu$m up to $3.5\,\mu$m, the relaxation oscillations are observed, followed by a slow increase in optical power and then power reaches a constant value. This means that LP_{11} mode switches on later than LP_{01} mode. This phenomenon will be discussed in detail in the next section.

6.4.3 Data Transmission

The investigated VCSELs are used as transmitters in an optical link as illustrated in the setup of Fig. 6.14. Its components are the same as that in Fig. 6.11 except from the sampling optical oscilloscope which is replaced by a germanium avalanche photodiode (Ge-APD) of 2 GHz bandwidth. After amplification of the photocurrent, the signal is analyzed in a sampling oscilloscope or in a bit error detector.

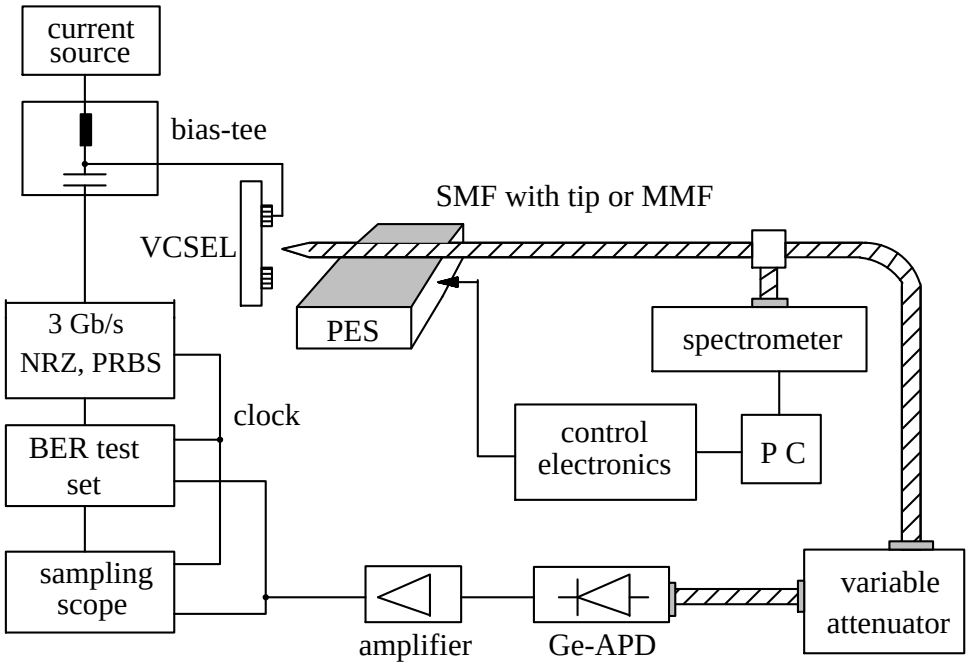


Fig. 6.14: *Setup for data transmission experiments with single-mode fiber (SMF) with tip or graded index multi-mode fiber (MMF).*

The theoretical treatment outlined in Section 6.2.3 gives an important equation, namely (6.27) which relates the receiver sensitivity $\eta\langle P\rangle$ to the on/off-ratio r_{10} and the receiver noise $\langle\delta i_{tot}\rangle$. To check the effect of on/off-ratio on $\eta\langle P\rangle$, a data transmission experment is done using a single-mode VCSEL with $D_a = 4\,\mu$m as a transmitter. In the bias free case, the VCSEL is fed with 1 Gb/s PRBS signal of $2^7 - 1$ word length and modulation voltage $V_{pp} = 2\,V$. This case is considered the ideal one because the logical zero $\langle i_0\rangle$ vanishes and hence the on/off-ratio is infinit, but some complications are encountered due to the turn-on delay which results in an assymetric eye diagram and consequently limits the bit rate of data transmission. A bias current of 2 mA and a 1 Gb/s PRBS signal of $2^7 - 1$ word length and modulation voltage $V_{pp} = 300\,mV$ are combined in a bias-tee and fed to the VCSEL.

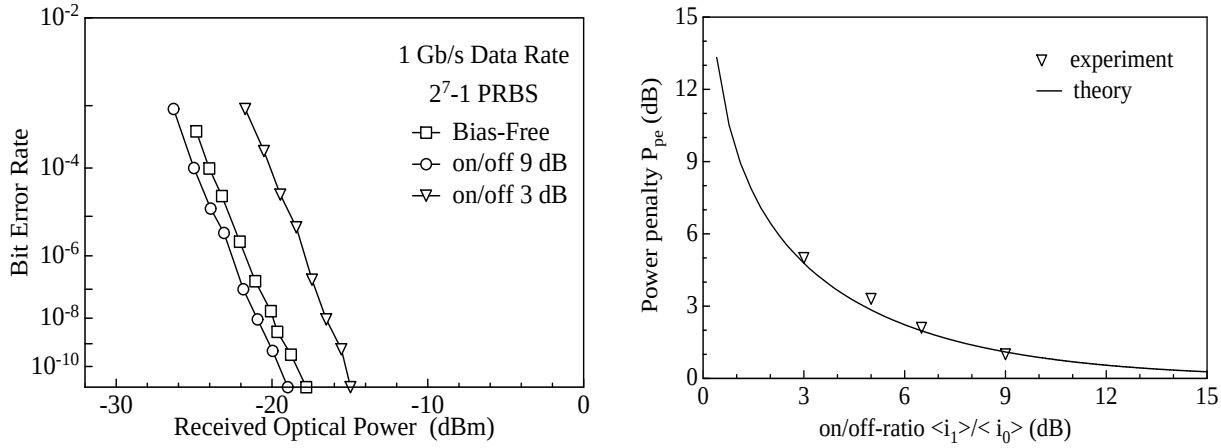


Fig. 6.15: *Bit error measurements using 5 m MMF and the 4 µm aperture single-mode VCSEL for three different cases defined by legends (left). Calculated (solid curve) and measured (open triangles) power penalty P_{pe} as a function of on/off-ratio (right).*

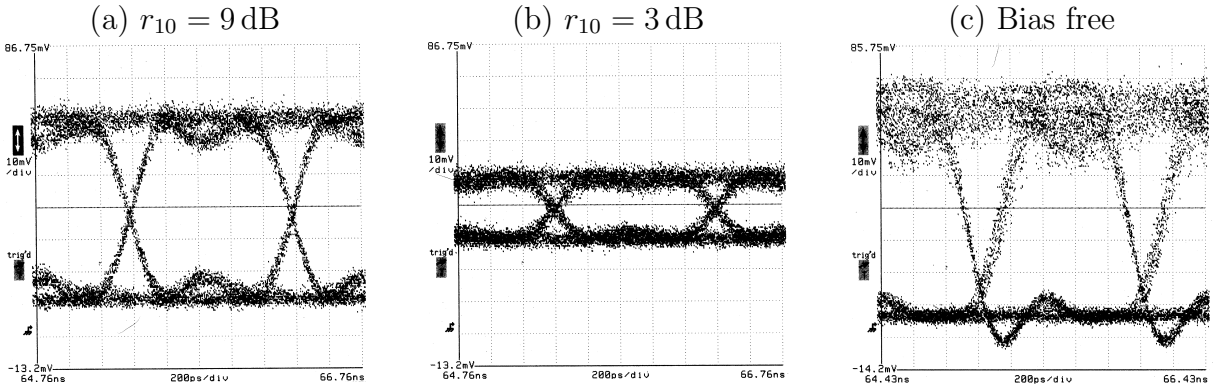


Fig. 6.16: *Eye diagrams recorded at* 10^{-11} *BER for the three cases of Fig. 6.15.*

The on/off-ratio is obtained from a sampling oscilloscope by dividing the average values of histograms on both the "1" and "0" rails of the eye diagram which is recoreded to be 9 dB in this case. By reducing the amplitude of the modulation voltage to $V_{pp} = 150\,\text{mV}$, the on/off-ratio is reduced to 3 dB. The results of the data transmission experiment using a 5 m length, 50 µm core diameter MMF are summarized in Fig. 6.15. The BER curves show that the received optical power for a BER of 10^{-11} is -19 dBm for $r_{10} = 9$ dB (open circles) with a power penalty of 1 dB for the case of bias free (open squares) and of 5 dB for $r_{10} = 3$ dB (open triangles). From (6.27) the power penalty (P_{pe}) in decibel can be expressed as

$$P_{pe} = 10 \log \left(\frac{r_{10} + 1}{r_{10} - 1} \right) \quad . \tag{6.34}$$

As shown in the right part of Fig. 6.15, the plot of P_{pe} as a function of $r_{10} = \langle i_1 \rangle / \langle i_0 \rangle$ agrees well with the observed data. Also, it is seen, as the on/off-ratio approaches infinty

the power penalty tends to zero. Practically this means the amplitude of modulation signal should be optimized in such a way that the on/off-ratio is kept as large as possible. Figure 6.16 shows the eye diagrams recorded at 10^{-11} BER for the three cases under investigation. In the bias cases (a) and (b) for 9 and 3 dB on/off-ratios, respectively, the eyes are open, symmetric, and without time delay. In contrast, in the case of bias free operation (c) the eye has much noise and is no longer symmetric due to the time delay of about 180 ps. That is why this case shows a penalty of 1 dB compared to the case of $r_{10} = 9\,\mathrm{dB}$ although it has $r_{10} = \infty$.
To investigate data transmission at different lateral fiber coupling offsets a SMF tip near-field scanning system is installed with a data transmission setup as shown in Fig. 6.14.

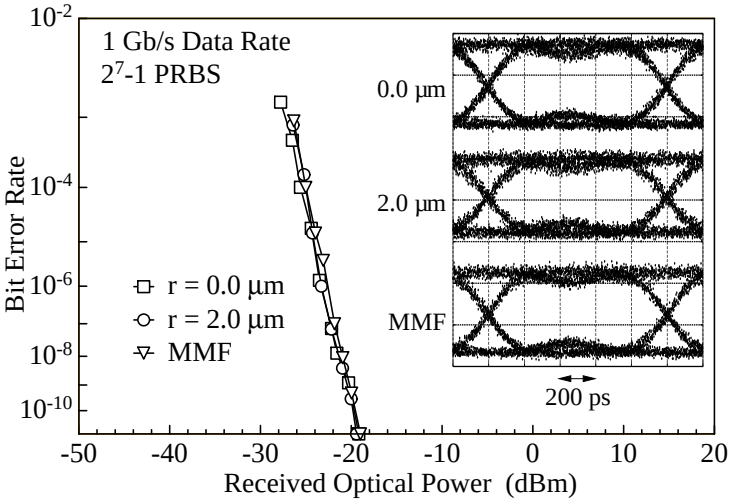


Fig. 6.17: *Bit error measurements using a 2 m length SMF at two different radial positions or using 5 m MMF. The 4 µm aperture single-mode VCSEL is biased at 2 mA dc and modulated with 1 Gb/s PRBS signals at a word length of* $2^7 - 1$ *and* $\mathrm{V_{pp}} = 300\,mV$*. The corresponding eyes are recorded at* 10^{-11} *BER.*

The bias current of 2 mA and a 1 Gb/s PRBS signal of $2^7 - 1$ word length and modulation voltage $\mathrm{V_{pp}} = 300\,\mathrm{mV}$ are combined in a bias-tee and fed to the VCSEL of $\mathrm{D_a} = 4\,\mu\mathrm{m}$. The results of the data transmission experiments using the 2 m length SMF whose tip has a semispherical lens and using a 5 m length, 50 μm core diameter MMF are summarized in Fig. 6.17. The eye diagrams in the inset show that as the SMF tip is moved laterally from the center at a radial position r = 0 to the edge of the $\mathrm{LP_{01}}$ mode at $\mathrm{r} = 2\,\mu\mathrm{m}$, the eye remains symmetric and has the same form as with the MMF. The received power for a BER of 10^{-11} is about $-19\,\mathrm{dBm}$ for both SMF and MMF. The radial distribution of $\langle i_1 \rangle / \langle i_0 \rangle$ is described by the closed squares in Fig. 6.18 and reveals a nearly constant ratio of 9 dB which is the same value as obtained by using MMF.

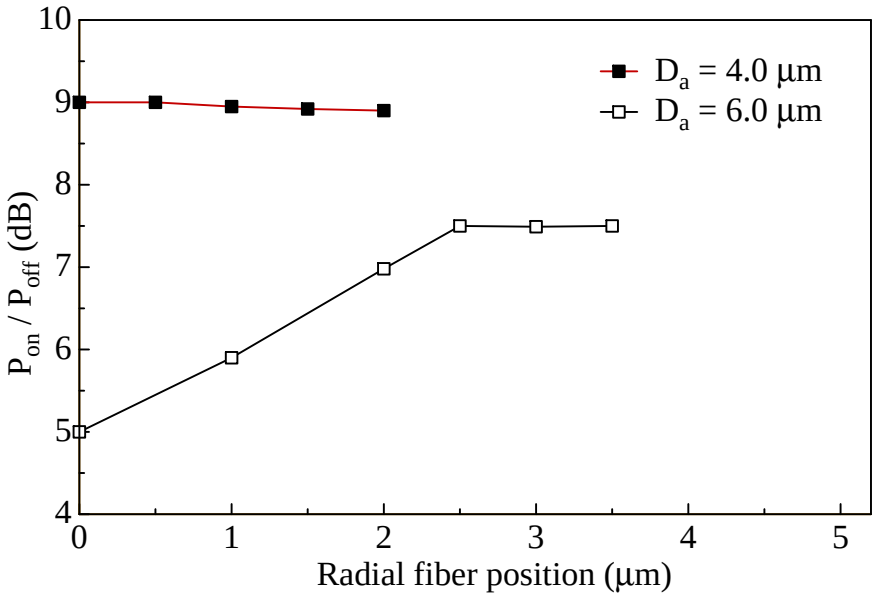


Fig. 6.18: *Spatial on/off-ratio distribution for a 4 µm aperture single-mode VCSEL (filled squares) under the same conditions as in Fig. 6.17 and for a 6 µm aperture two-mode device (open squares) under the same conditions as in Fig. 6.19.*

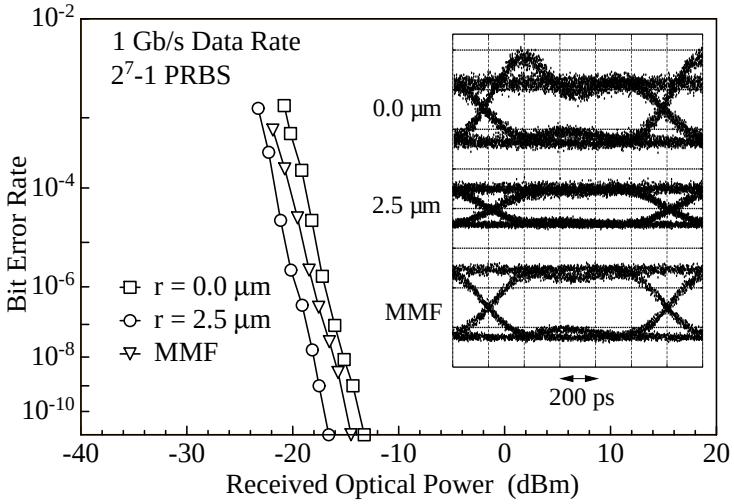


Fig. 6.19: *Bit error measurements using 2 m SMF at different radial positions defined by the legends or 5 m MMF for a 6 µm aperture two-mode device driven at 2 mA dc and 1 Gb/s PRBS signal at a word length* $2^7 - 1$ *and* $V_{pp} = 150\,mV$*. The corresponding eyes are recorded at* 10^{-11} *BER.*

In case of the multi-mode VCSEL, the same bias current and modulation signal, however with $V_{pp} = 150\,mV$, are chosen. In accordance with the emission spectrum in Fig. 6.9(d), at the center both LP_{01} and LP_{11} modal power is coupled into the SMF. As the tip is moved toward the edge of the VCSEL, the LP_{01} mode is strongly attenuated and shows

10 dB suppression ratio in the interval between r = 2.5 . . . 3.5 μm. This is evidenced in the results of the data transmission experiments in Fig. 6.19 using the forementioned fibers. The eye diagrams in the inset show that at r = 0 the eye is no longer symmetric because the LP_{01} and LP_{11} modes are both coupled into the SMF. Since the LP_{11} mode has a higher threshold current, as seen in Fig. 6.8, it has a lower resonance frequency at the same bias current and as a result gives rise to ringing in the eye diagram. At r = 2.5 μm, the dominance of LP_{11} at a sidemode suppression in the order of 10 dB gives a symmetric eye opening with a longer switch-on time than at r = 0, as expected. These conclusions are supported by the results of theoretical simulations performed in [62]. In calculations of the time traces of the LP_{11} and LP_{01} modal powers it was found that the latter has a shorter turn-on delay and accordingly the LP_{01} mode starts lasing emission. When a significant number of photons are present in the laser microcavity, a hole is burnt in the carrier profile which leads to the excitation of the higher order LP_{11} mode. Using a MMF, a superposition of all portions of the two modes gives an eye diagram with symmetric opening. The BER curves show that the received optical power for a BER of 10^{-11} is -16.6 dBm for the SMF at r = 2.5 μm with a power penalty of 3.3 dB at r = 0 and of 2.1 dB for the MMF. This difference is attributed to the radial change of $\langle i_1 \rangle / \langle i_0 \rangle$, as illustrated in Fig. 6.18 (open squares). The on/off-ratio is continually increasing up to r = 2.5 μm where it reaches a constant value of about 7.5 dB, while 6.5 dB ratio is recorded for the MMF. These results are also confirmed by the separate light-current characteristics in Fig. 6.8 which are obtained from the spectrometer as the peak spectral power of each mode. In accordance with these curves, the average differential efficiency for the LP_{01} mode is smaller than for LP_{11} in the interval around 2 mA at which the VCSEL

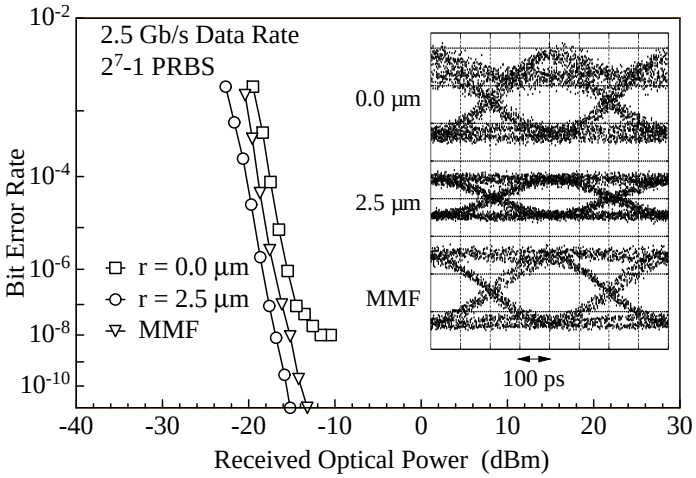


Fig. 6.20: *The same measurements as in Fig. 6.19 at 2.5 Gb/s data rate. The eyes are recorded at the minimum BER for each case.*

is modulated. The data transmission experiments are repeated with the same multi-mode VCSEL and fibers for 2.5 Gb/s data rate as shown in Fig. 6.20. The same effects as in the case of 1 Gb/s data transmission are seen, but a BER floor at 10^{-8} is observed at r = 0 because the "1" rail in the eye diagram exhibits much noise which reduces its opening. This incresed noise is probably due to mode partition because as the total optical power remains constant, the relative distribution of the modal powers fluctuates as shown in Fig. 6.8.

As can be seen from these data transmission experiments, the on/off-ratio has a significant influence on the BER when either a single-mode or multi-mode VCSEL is used as a transmitter. This in turn causes a significant penatly on the received power at very low bit error levels of 10^{-11}.

Chapter 7

Concluding Remarks

In order to benefit from the favorable properties of VCSELs as light sources for optical transmission systems, studies of the transverse mode characteristics of these device were the aim of the present thesis, since, for fiber coupling both single-mode and multimode VCSEL approaches are followed today in combination with graded-index multimode fibers. In this work, three phenomena are studied in the static case, i.e., under continuous wave operation. The first is an investigation of the waveguiding mechanism in VCSELs induced by the oxide layer. Secondly, longitudinal mode switching as a new phenomenon in long monolithic cavity VCSELs is examined. The third is related to the effect of increasing the cavity length of VCSELs on the output characteristics and the eigenmode structure. In the dynamic case, i.e. at large and small signal modulation, a spatial investigation of the transverse mode turn-on dynamics in VCSELs is made. From the results of these investigations the following conclusions may be drawn:

- Since single-mode VCSELs oscillate on the fundamental LP_{01} mode, there is good agreement between the theoretical Gaussian distribution and the measured near field (NF) data as mentioned in chapters 3 and 4. In addition, the transformation of the Gaussian profile from near field into far field is a Gaussian profile as well and is in agreement with the far field (FF) measurements. This indicates that stable positioning is achieved using the NF scanning system with resolution better than 50 nm. Moreover, the principle of using a single-mode fiber tip is suitable in the NF scanning system.

- According to the simulations presented in chapter 3, the position of the oxide layer relative to the standing wave pattern in the cavity is very important and it has to lie at a node of the standing wave pattern to reduce the induced refractive index step. In addition, its thickness should also be as small as possible for the same reason (the experimental limit is ≈ 20 nm). From an experimental point of view an inherent relation is found between this index step and both the mode confinement and the mode spacing. The larger the index step, the larger the mode confinement and the mode spacing are.

- For extended cavity VCSELs presented in chapter 4, it is shown that both modal gain and induced oxide index are responsible for switching between longitudinal modes. Consistent spectral as well as near- and far-field analyses combined with transfer matrix calculations well describe the observed data and show that the these modes are either dominantly guided by the built-in effective index step or the thermally induced index profile. As evidenced by the record values of 5 mW for devices with spacer length $L_s = 4\,\mu$m and 5.5 mW (if not regarding the longitudinal mode switching) for $L_s = 8\,\mu$m, VCSELs of the extended cavity type are suitable candidates to obtain higher single-mode output power from monolithic devices. Their reduced number of transverse eigenmodes compared with the standard VCSELs confirms the principle of design for these devices, i.e. the increased scattering losses of the higher order modes due to the lateral growing of the mode area with increasing cavity length. Also, their larger active diameter and thus reduced series resistance and driving current density is expected to improve both manufacturability and reliability. The obtained understanding of guiding effects should allow for better tailoring of emission properties in future laser designs.

- The calculated butt-coupling efficiency η_m of VCSELs into flat cut fibers using the measured parameters of beam half width yields a good agreement with the measured data as can be seen in chapter 5. Moreover, it is found that for SMF η_m depends mainly on the matching between the field radii of both the optical fiber and the light source and is maximized when these radii are the same. Of course, η_m is related to the translation distance Δz between the VCSEL and the fiber because this distance is a dominant variable in the spot size, i.e. $w_L = w_L(\Delta z)$. In the case of $8.3\,\mu$m Standard SMF for 1300 nm wavelength, the excited higher order modes for 850 nm wavelength is filtered by macrobending of this fiber. This filter consists simply of a fiber loop with 12 mm diameter and 5 windings. The inclusion of this simple filter leads to sufficient losses of the higher order modes and the fiber becomes single mode at 850 nm wavelengths.

- Bit error rate measurements at 1 Gb/s and 2.5 Gb/s for single-mode and multi-mode VCSELs have been presented for different lateral SMF offsets which point to a better performance of single-mode compared with multi-mode VCSELs. The multi-mode device has shown a lateral variation of the on/off-ratio which leads to a reduced BER for the LP_{11} mode at 10 dB LP_{01} suppression than when the two modes coexist. One can conclude from these results that at moderate bit rates the

on/off-ratio is the dominant mechanism governing the BER measurements regardless of the type of oscillating mode in the cavity. The difference between the switch-on times of the lasing modes in the multi-mode device can be of importance even at high bit rates.

References

[1] K.J. Ebeling, *Integrated Optoelectronics*. Berlin: Springer-Verlag, (1993).

[2] H.C. Casey and M.B. Panish, *Heterostructure Lasers*, Part B. New York: Academic Press, (1978).

[3] H. Soda, K. Iga, C. Kitahara, and Y. Suematsu, "GaInAsP/InP surface emitting injection lasers", *Jpn. J. Appl. Phys.* vol. 18, pp. 2329–2330, (1979).

[4] J.L. Jewell, A. Scherer, S.L. McCall, Y.H. Lee, S. Walker, J.P. Harbison, and L.T. Florez, "Low-threshold electrically pumped vertical-cavity surface-emitting microlasers", *Electron. Lett.*, vol. 25, pp. 1123–1124, (1989).

[5] K. Iga, *Fundamentals of Laser Optics*. New York: Plenum Press, (1994).

[6] L.A. Coldren and S.W. Corzine, *Diode Lasers and Photonic Integrated Circuits*. New York: J. Wiley & Sons, (1995).

[7] R.S. Geels, S.W. Corzine, J.W. Scott, D.B. Young, and L.A. Coldren, "Low threshold planarized vertical-cavity surface-emitting lasers", *IEEE Photon. Technol. Lett.*, vol. 2, pp. 234–236, (1990).

[8] M. Orenstein, A.C. Von Lehmen, C. Chang-Hasnain, N.G. Stoffel, J.P. Harbison, L.T. Florez, E. Clausen, and J.E. Jewell, "Vertical-cavity surface-emitting InGaAs/GaAs lasers with planar lateral definition", *Appl. Phys. Lett.*, vol. 56, pp. 2384–2386, (1990).

[9] B. Tell, Y.H. Lee, K.F. Brown-Goebeler, J.L. Jewell, R.E. Leibenguth, M.T. Asom, G. Livescu, L. Luther, and V.D. Mattera, "High-power cw vertical-cavity top surface-emitting GaAs quantum well lasers", *Appl. Phys. Lett.*, vol. 57, pp. 1855–1857, (1990).

[10] D.L. Huffaker, D.G. Deppe, K. Kumar, and T.J. Rogers, "Native-oxide defined ring contact for low threshold vertical-cavity lasers", *Appl. Phys. Lett.*, vol. 65, pp. 97–99, (1994).

[11] R.A. Morgan, J.A. Lehman, and M.K. Hibbs-Brenner, "Vertical-cavity surface-emitting lasers come of age", in *Fabrication, Testing, and Reliability of Semiconductor Lasers*, M. Fallahi and S.C. Wang (Eds.), Proc. SPIE 2683, pp. 18–29, (1996).

[12] K.D. Choquette and H.Q. Hou, "Vertical-cavity surface emitting lasers: Moving from research to manufacturing", *Proc. IEEE*, vol. 85, pp. 1730–1739, (1997).

[13] K.L. Lear, K.D. Choquette, R.P. Schneider, S.P. Kilcoyne, and K.M. Geib, "Selectively oxidised vertical cavity surface emitting lasers with 50 % power conversion efficiency", *Electron. Lett.*, vol. 31, pp. 208–209, (1995).

[14] B. Weigl, M. Grabherr, C. Jung, R. Jäger, G. Reiner, R. Michalzik, D. Sowada, and K.J. Ebeling, "High-performance oxide-confined GaAs VCSELs", *IEEE J. Sel. Top. Quantum Electron.*, vol. 3, pp. 409–415, (1997).

[15] D.L. Huffaker, L.A. Graham, H. Deng, and D.G. Deppe, "Sub-40 μA continuous-wave lasing in an oxidized vertical-cavity surface emitting laser with dielectric mirrors", *IEEE Photon. Technol. Lett.*, vol. 8, pp. 974–976, (1996).

[16] M. Grabherr, M. Miller, R. Jäger, R. Michalzik, U. Martin, H. Unold, and K.J. Ebeling, "High-power VCSEL's: Single devices and densely packed 2-D-arrays", *IEEE J. Sel. Top. Quantum Electron.*, vol. 5, pp. 495–502, (1999).

[17] Guy Verschaffelt, Jan Albert, Krassimir Panajotov, Bob Nagler, Michael Peeters, Hugo Thienpont, Irina Veretennicoff, Jan Danckaert, Sylvain Barbay, Giovanni Giacomelli, and Francesco Marin, "Frequency response of current modulation induced polarization switching in VCSELs", Proc. SPIE'2002, 4649, in Press, San Jose, California, USA, Jan. 2002.

[18] H. Kressel, and J.K. Butler, *Semiconductor Lasers and Heterojunction LEDs.* London: Academic Press (1977).

[19] P.W.A. McIlroy, A. Kurobe, and Y. Uematsu, "Analysis and application of theoretical gain curves to the design of multi-quantum-well lasers", *IEEE J. Quantum Electron.*, vol. 21, pp. 1958–1963, 1985.

[20] M. Born and E. Wolf, *Principles of Optics*, 6th ed. Oxford: Pergamon Press, (1989).

[21] P. Yeh, *Optical Waves in Layered Media.* New York: J. Wiley & Sons, (1988).

[22] K.J. Ebeling and L.A. Coldren, "Analysis of multielement semiconductor lasers", *J. Appl. Phys.*, vol. 54, pp. 2962–2969, (1983).

[23] S.W. Corzine, R.S. Geels, J.W. Scott, R.-H. Yan, and L.A. Coldren, "Design of Fabry-Perot surface-emitting lasers with a periodic gain structure", *IEEE J. Quantum Electron.*, vol. 25, pp. 1513–1524, (1989).

[24] R. Michalzik, K.J. Ebeling"Operation Principles of VCSELs", in *Vertical-Cavity Surface-Emitting Laser Devices*, E.H. Li and K. Iga (Eds.). Heidelberg: Springer Verlag, in press.

[25] S. Adachi, "GaAs, AlAs, and $Al_xGa_{1-x}As$: Material parameters for use in research and device applications", *J. Appl. Phys.*, vol. 58, pp. R1–R29, (1985).

[26] R. Michalzik,"Modellierung und Design von Laserdioden mit Vertikalresonator". *Ph. D. Thesis*, University of Ulm, Germany, (1996).

[27] R. Michalzik and K.J. Ebeling, "Modeling and design of proton-implanted ultralow-threshold vertical-cavity laser diodes", *IEEE J. Quantum Electron.*, vol. 29, pp. 1963–1974, (1993).

[28] G. Reiner, E. Zeeb, B. Möller, M. Ries, and K.J. Ebeling, "Optimization of planar Be-doped InGaAs VCSELs with two-sided output", *IEEE Photon. Technol. Lett.*, vol. 7, pp. 730–732, (1995).

[29] R. Jäger, M. Grabherr, C. Jung, R. Michazik, G. Reiner, B. Weigl, and K. J. Ebeling, "57% wallplug efficiency oxide-confined 850 nm wavelength GaAs VCSEL's", *Electron. Lett.*, vol. 33, pp. 330–331, (1997).

[30] M.H. MacDougal, H. Zhao, P.D. Dapkus, M. Ziari, and W.H. Steier, "Wide-bandwidth distributed Bragg reflectors using oxide/GaAs multilayers", *Electron. Lett.*, vol. 30, pp. 1147–1148, 1994.

[31] G.R. Hadley, "Effective index model for vertical-cavity surface-emitting lasers", *Opt. Lett.*, vol. 20, pp. 1483–1485, (1995).

[32] H.G. Unger, *Optische Nachrichtentechnik*. Heidelberg, Germany: Hüthig Verlag, (1985).

[33] A.W. Snyder and J.D. Love, *Optical Waveguide Theory*. London: Chapman & Hall, (1991).

[34] D. Marcuse, *Light Transmission Optics*. New York: Van Nostrand Reinhold Company, (1972).

[35] Operating manual. Physik Instrumente (PI) GmbH & Co., Waldbronn, Germany.

[36] TECOS GmbH, Düsseldorf, Germany.

[37] User's guide for HP 86120A Multi-Wavelength Meter, Hewlett Packard Company, USA, 1996.

[38] G. Grau, W. Freude, *Optische Nachrichtentechnik*. Berlin: Springer Verlag, 1991.

[39] K. Faltin, "Untersuchungen zur Nahfeldverteilung von Transversalmoden in Laserdioden mit Vertikalresonator". *Ph.D. Thesis*, University of Ulm, Germany, 1999.

[40] M. Brunner, K. Gulden, R. Hövel, M. Moser, and M. llegems, "Thermal lensing effects in small oxide confined vertical-cavity surface-emitting lasers", *Appl. Phys. Lett.*, vol. 76, pp. 7–9, 2000.

[41] N.K. Dutta, L.W. Tu, G. Zydzik, Y.H. Wang, and A.Y. Cho, "Anomalous temporal response of gain guided surface emitting lasers", *Electron. Lett.*, vol. 27, pp. 208–210, 1991.

[42] D.G. Deppe and D.L. Huffaker, "High spatial coherence vertical-cavity surface-emitting laser using a long monolithic cavity", *Electron. Lett.*, vol. 33, pp. 211–213, 1997.

[43] H.J. Unold, S.W.Z. Mahmoud, R. Jäger, M. Kicherer, M.C. Riedl, and K.J. Ebeling, "Improving single-mode VCSEL performance by introducing a long monolithic cavity", *IEEE Photon. Technol. Lett.*, vol. 12, pp. 939–941, 2000.

[44] Wave Optics, "Specialty Fiber Optic Products", Datenblatt, p. 5, 1996.

[45] D. Marcuse, "Curvature loss formula for optical fibers", *J. Opt. Soc. Am.*, vol. 66, pp. 216–220, 1976.

[46] J. Heinrich, E. Zeeb and K. J. Ebeling, "Butt-coupling efficiency of VCSEL's into multimode fibers", *IEEE Photon. Technol. Lett.*, vol. 9, pp. 1555–1557, 1997.

[47] P. Schnitzer, R. Jäger, M. Grabherr, D. Wiedenmann, F. Mederer, and K.J. Ebeling, "GaAs VCSELs for biased and bias-free multi Gb/s data transmission over 4.4 km standard 1300 nm single-mode fiber", in Proc. LEOS' 98, pp. 164–165, Orlando, FL, USA, Dec. 1998.

[48] P. Schnitzer, R. Jäger, C. Jung, R. Michalzik, D. Wiedenmann, F. Mederer, and K.J. Ebeling, "Biased and bias-free multi-Gb/s data links using GaAs VCSEL's and 1300 nm single-mode fiber", *IEEE Photon. Technol. Lett.*, vol. 10, pp. 1781–1783, 1998.

[49] D.G. Deppe, D.L. Huffaker, T. Oh, H. Deng, and Q. Deng "Low-threshold vertical-cavity surface-emitting lasers based on oxide-confined and high contrast distributed Bragg reflectors", *IEEE J. Sel. Topics Quantum Electron.*, vol. 3, pp. 893–904, 1997.

[50] C. Jung, R. Jäger, P. Schnitzer, R. Michalzik, B. Weigl, S. Müller, and K.J. Ebeling "4.8 mW single-mode oxide confined top-surface emitting vertical-cavity laser diodes", *Electron. Lett.*, vol. 32, pp. 1790–1791, 1997.

[51] R. King, R. Michalzik, C. Jung, M. Grabherr, F. Eberhard, R. Jäger, P. Schnitzer, and K.J. Ebeling "Oxide confined 2D VCSEL arrays for high-density inter/intra-chip interconnects", Proc. SPIE'98, 3286, 64–67, San Jose, California, USA, Jan. 1998.

[52] D. Wiedenmann, R. King, C. Jung, R. Jäger, P. Schnitzer, R. Michalzik, and K.J. Ebeling "Design and analysis of single-mode oxidized VCSEL's for high-speed optical interconnects", *IEEE J. Quantum Electron.*, vol. 5, pp. 503–511, 1999.

[53] C. Deng, I. Fischer, and W. Elsäßer, "Transverse modes in oxide confined VCSELs: Influence of pump profile, spatial hole burning, and thermal effects", *Optics Express*, vol. 5, pp. 38–47, 1999.

[54] Y.G. Zhao and J. McInerney, "Transverse-mode control of vertical-cavity surface-emitting lasers", *IEEE. J. Quantum Electron.*, vol. 32, pp. 1950–1958, 1996.

[55] K. Petermann, *Laser Diode Modulation and Noise*. Dordrecht: Kluwer Academic Publishers, 1991.

[56] R. Nagarajan, M. Ishikawa, T. Fukushima, R.S. Geels, and J.E. Bowers, "High speed quantum-well lasers and carrier transport effects", *IEEE J. Quantum Electron.*, vol. 28, pp. 1990–2008, 1992.

[57] K.Y. Lau, "Dynamics of quantum well lasers", in P.S. Zory, Jr. (Ed.), *Quantum Well Lasers.* Boston: Academic Press, 1993.

[58] A. Yariv, "Quantum Electronics", third edition, New York: Wiley 1982.

[59] J.H. Shin, Y.G. Ju, H.E. Shin, and Y.H. Lee, "Spontaneous emission factor of oxidized vertical-cavity surface-emitting lasers from the measured below-threshold cavity loss", *Appl. Phys. Lett.*, vol. 70, pp. 2344–2346, 1997.

[60] D. Wiedenmann,"Dynamische Eigenschaften und Rauschen selektiv oxidierter Vertikallaserdioden". *Ph.D. Thesis*, University of Ulm, Germany, 1999.

[61] User manual for Sampling Optical Oscilloscope OOS-01, Hamamatsu Photonics, 1988.

[62] J. Dellunde, M.C. Torrent, J.M. Sancho, and K.A. Shore, "Statistics of transverse-mode turn-on dynamics in VCSEL's", *IEEE J. Quantum Electron.*, vol. 33, pp. 1197–1204, 1997.

Appendix A

Sample Structures

In the following tables, the structure of the investigated samples are depicted. Tables A.1 and A.2 represent the structure of samples M46/97 and M108/97. They are designed for 850 nm wavelength VCSELs and have two different positions of the oxide layer in the cavity. Table A.3 gives the structure of sample M69/98 which is designed for a 980 nm standard VCSEL. This sample is taken as a reference for the extended cavity devices. In this class of VCSEL a n-doped GaAs spacer is added directly underneath the active layer as shown in table A.4 for sample M17/99 which stands for the case of 2 μm spacer. By the same way the other two cases are designed, namely with 4 and 8 μm spacer lengths for samples M67/99 and M80/99, respectively.

Tab. A.1: *Layer structure of sample M46/97.*

Function	Thickness (nm)	Material
contact layer	37	GaAs
	24	$Al_{0.21}Ga_{0.79}As$
p-DBR	$23 \times$ 22	$Al_{0.57}Ga_{0.43}As \rightarrow Al_{0.90}Ga_{0.10}As$
	$23 \times$ 30	$Al_{0.90}Ga_{0.10}As$
	$23 \times$ 22	$Al_{0.90}Ga_{0.10}As \rightarrow Al_{0.57}Ga_{0.43}As$
	$23 \times$ 63	$Al_{0.21}Ga_{0.79}As$
half mirror-pair of p-DBR	5	$Al_{0.57}Ga_{0.43}As$
	33	AlAs
	35	$Al_{0.57}Ga_{0.43}As$
last three mirror-pairs of p-DBR	$3 \times$ 24	$Al_{0.21}Ga_{0.79}As$
	$3 \times$ 22	$Al_{0.57}Ga_{0.43}As \rightarrow Al_{0.90}Ga_{0.10}As$
	$3 \times$ 30	$Al_{0.90}Ga_{0.10}As$
	$3 \times$ 22	$Al_{0.90}Ga_{0.10}As \rightarrow Al_{0.57}Ga_{0.43}As$
	$3 \times$ 63	$Al_{0.21}Ga_{0.79}As$
central cavity	70	$Al_{0.57}Ga_{0.43}As$
	40	$Al_{0.26}Ga_{0.74}As$
	8	GaAs
	11	$Al_{0.26}Ga_{0.74}As$
	8	GaAs
	11	$Al_{0.26}Ga_{0.74}As$
	8	GaAs
	40	$Al_{0.26}Ga_{0.74}As$
	70	$Al_{0.57}Ga_{0.43}As$
first three mirror-pairs of n-DBR	$3 \times$ 63	$Al_{0.57}Ga_{0.43}As$
	$3 \times$ 69	$Al_{0.21}Ga_{0.79}As$
n-DBR	$30 \times$ 58	$Al_{0.21}Ga_{0.79}As$
	$30 \times$ 5	$Al_{0.52}Ga_{0.48}As$
	$30 \times$ 71	AlAs
	$30 \times$ 5	$Al_{0.52}Ga_{0.48}As$
	122	$Al_{0.52}Ga_{0.48}As \rightarrow Al_{0.04}Ga_{0.96}As$
	24	GaAs
substrate		GaAs

Tab. A.2: *Layer structure of sample M108/97.*

Function	thickness (nm)	Material
Contact layer	39	GaAs
	10	$Al_{0.20}Ga_{0.80}As$
upper Bragg-Reflector	23 × 13	$Al_{0.27}Ga_{0.73}As \rightarrow Al_{0.47}Ga_{0.53}As$
	20	$Al_{0.47}Ga_{0.53}As \rightarrow Al_{0.90}Ga_{0.10}As$
	31	$Al_{0.90}Ga_{0.10}As$
	20	$Al_{0.90}Ga_{0.10}As \rightarrow Al_{0.47}Ga_{0.53}As$
	13	$Al_{0.47}Ga_{0.53}As \rightarrow Al_{0.27}Ga_{0.73}As$
	38	$Al_{0.20}Ga_{0.80}As$
last mirror of the upper Bragg-Reflector	13	$Al_{0.27}Ga_{0.73}As \rightarrow Al_{0.47}Ga_{0.53}As$
	24	$Al_{0.47}Ga_{0.53}As \rightarrow Al_{0.61}Ga_{0.39}As$
	96	$Al_{0.61}Ga_{0.39}As$
	33	AlAs
	120	$Al_{0.61}Ga_{0.39}As$
central cavity	23	$Al_{0.61}Ga_{0.39}As \rightarrow Al_{0.67}Ga_{0.33}As$
	45	$Al_{0.67}Ga_{0.33}As \rightarrow Al_{0.54}Ga_{0.46}As$
	42	$Al_{0.54}Ga_{0.46}As \rightarrow Al_{0.44}Ga_{0.56}As$
	24	$Al_{0.44}Ga_{0.56}As \rightarrow Al_{0.38}Ga_{0.22}As$
	41	$Al_{0.26}Ga_{0.74}As$
	8	GaAs
	2 × 10	$Al_{0.26}Ga_{0.74}As$
	8	GaAs
	41	$Al_{0.26}Ga_{0.74}As$
	24	$Al_{0.38}Ga_{0.62}As \rightarrow Al_{0.44}Ga_{0.56}As$
	42	$Al_{0.44}Ga_{0.56}As \rightarrow Al_{0.54}Ga_{0.46}As$
	45	$Al_{0.54}Ga_{0.46}As \rightarrow Al_{0.67}Ga_{0.33}As$
	23	$Al_{0.67}Ga_{0.33}As \rightarrow Al_{0.47}Ga_{0.53}As$
lower Bragg-Reflector	38 × 38	$Al_{0.20}Ga_{0.80}As$
	13	$Al_{0.27}Ga_{0.73}As \rightarrow Al_{0.47}Ga_{0.53}As$
	20	$Al_{0.47}Ga_{0.53}As \rightarrow Al_{0.90}Ga_{0.10}As$
	31	$Al_{0.90}Ga_{0.10}As$
	20	$Al_{0.90}Ga_{0.10}As \rightarrow Al_{0.47}Ga_{0.53}As$
	13	$Al_{0.47}Ga_{0.53}As \rightarrow Al_{0.27}Ga_{0.73}As$
	51	$Al_{0.20}Ga_{0.80}As$
	38	GaAs
	50	AlAs
	109	GaAs
Substrate		GaAs

Tab. A.3: *Layer structure of sample M69/98.*

Function	Thickness (nm)	Material
contact layer	22	GaAs
	8	GaAs
	30	GaAs
p-DBR	17 × 11	$Al_{0.37}Ga_{0.63}As \rightarrow Al_{0.20}Ga_{0.80}As$
	17 × 20	$Al_{0.89}Ga_{0.11}As \rightarrow Al_{0.47}Ga_{0.53}As$
	17 × 51	$Al_{0.93}Ga_{0.07}As$
	17 × 4	$Al_{0.84}Ga_{0.16}As$
	17 × 12	$Al_{0.47}Ga_{0.53}As \rightarrow Al_{0.84}Ga_{0.16}As$
	17 × 11	$Al_{0.20}Ga_{0.80}As \rightarrow Al_{0.37}Ga_{0.63}As$
	17 × 49	GaAs
last mirror of p-DBR	11	$Al_{0.37}Ga_{0.63}As \rightarrow Al_{0.20}Ga_{0.80}As$
	24	$Al_{0.60}Ga_{0.40}As \rightarrow Al_{0.47}Ga_{0.53}As$
	120	$Al_{0.60}Ga_{0.40}As$
	27	AlAs
	28	$Al_{0.47}Ga_{0.53}As \rightarrow Al_{0.60}Ga_{0.40}As$
	38	$Al_{0.47}Ga_{0.53}As$
central cavity	75	$Al_{0.37}Ga_{0.63}As$
	40	GaAs
	10	GaAs
	8	$In_{0.18}Ga_{0.82}As$
	2 × 10	GaAs
	2 × 8	$In_{0.18}Ga_{0.82}As$
	10	GaAs
	40	GaAs
	75	$Al_{0.37}Ga_{0.63}As$
first mirror of n-DBR	79	$Al_{0.47}Ga_{0.53}As$
	11	$Al_{0.20}Ga_{0.80}As \rightarrow Al_{0.37}Ga_{0.63}As$
n-DBR	40 × 49	GaAs
	40 × 11	$Al_{0.37}Ga_{0.63}As \rightarrow Al_{0.20}Ga_{0.80}As$
	40 × 12	$Al_{0.84}Ga_{0.16}As \rightarrow Al_{0.47}Ga_{0.53}As$
	40 × 51	$Al_{0.93}Ga_{0.07}As$
	40 × 20	$Al_{0.47}Ga_{0.53}As \rightarrow Al_{0.89}Ga_{0.11}As$
	40 × 11	$Al_{0.20}Ga_{0.80}As \rightarrow Al_{0.37}Ga_{0.63}As$
	109	GaAs
	88	GaAs
substrate		GaAs

Tab. A.4: *Layer structure of sample M17/99.*

Function	thickness (nm)	Material
Contact layer	24	GaAs
	8	GaAs
	30	GaAs
upper Bragg-Reflector	$17 \times$ 11	$Al_{0.37}Ga_{0.63}As \rightarrow Al_{0.20}Ga_{0.80}As$
	$17 \times$ 20	$Al_{0.89}Ga_{0.11}As \rightarrow Al_{0.47}Ga_{0.53}As$
	$17 \times$ 52	$Al_{0.93}Ga_{0.07}As$
	$17 \times$ 12	$Al_{0.47}Ga_{0.53}As \rightarrow Al_{0.84}Ga_{0.16}As$
	$17 \times$ 11	$Al_{0.20}Ga_{0.80}As \rightarrow Al_{0.37}Ga_{0.63}As$
	$17 \times$ 51	GaAs
last mirror of the upper Bragg-Reflector	11	$Al_{0.37}Ga_{0.63}As \rightarrow Al_{0.20}Ga_{0.80}As$
	25	$Al_{0.60}Ga_{0.40}As \rightarrow Al_{0.47}Ga_{0.53}As$
	123	$Al_{0.60}Ga_{0.40}As$
	27	AlAs
	28	$Al_{0.47}Ga_{0.53}As \rightarrow Al_{0.60}Ga_{0.40}As$
	39	$Al_{0.47}Ga_{0.53}As$
central cavity	77	$Al_{0.37}Ga_{0.63}As$
	35	GaAs
	10	GaAs
	8	$In_{0.19}Ga_{0.81}As$
	$2 \times$ 10	GaAs
	$2 \times$ 8	$In_{0.19}Ga_{0.81}As$
	10	GaAs
	35	GaAs
	77	$Al_{0.37}Ga_{0.63}As$
first mirror of the lower Bragg-Reflector	79	$Al_{0.47}Ga_{0.53}As$
	11	$Al_{0.20}Ga_{0.80}As \rightarrow Al_{0.37}Ga_{0.63}As$
Spacer	2036	GaAs
lower Bragg-Reflector	$40 \times$ 51	GaAs
	$40 \times$ 11	$Al_{0.37}Ga_{0.63}As \rightarrow Al_{0.20}Ga_{0.80}As$
	$40 \times$ 12	$Al_{0.84}Ga_{0.16}As \rightarrow Al_{0.47}Ga_{0.53}As$
	$40 \times$ 52	$Al_{0.47}Ga_{0.53}As \rightarrow Al_{0.89}Ga_{0.11}As$
	$40 \times$ 20	$Al_{0.20}Ga_{0.80}As \rightarrow Al_{0.37}Ga_{0.63}As$
	$40 \times$ 11	
	109	GaAs
	88	GaAs
Substrate		GaAs

Appendix B

List of Important Symbols

$a = \partial g/\partial n$	differential gain coefficient
a_c	laser active radius
a_f	fiber core radius
$\hat{a}$	lattice constant
A_N	signal noise amplitude
A_N	maximum sisgnal amplitude
B	bit rate
BER	bit error rate
c	velocity of light in vacuum
$D = A_S/A_N$	Dynamic range
D_a	active diameter of laser
E	electric field strength
$\vec{E}$	vector of the real electric field
$f_{\max}$	band width of signal
f_{samp}	sampling frequency
$F_n(t)$, $F_N(t)$	Langevin force for electron and photon densities, respectively
g	gain coefficient
g_{th}	threshold gain coefficient
g_m	mode gain coefficient
g_p	maximum gain coefficient
H	magnetic field strength
$\vec{H}$	vector of the real magnetic field
$H(\nu)$	transfer function
h	Planck's constant
$\hbar = h/2\pi$	reduced Plank's constant
I	electric current
i_D	dark photo current
i_{ph}	photo current
I_{on}	turn-on current
I_{off}	turn-off current

J_l	Bessel function of order l
k	Boltzmann's constant
K_l	modified Hankel function of order l
k_c, k_v	electron wave vectors in the conduction and valence bands
L	laser cavity length
l_{eff}	photon penetration depths in the mirrors
L_{eff}	effective resonator length
N	photon density
NA	numerical aperture of the optical fiber
$\bar{n}_{\mathrm{b}}$	electron density in the barrier
$\bar{n}_{\mathrm{c}}$	waveguide core refractive index
$\bar{n}_{\mathrm{cl}}$	waveguide cladding refractive index
$\Delta_{\mathrm{n}} = \bar{n}_{\mathrm{c}} - \bar{n}_{\mathrm{cl}}$	refractive index step
n_{w}	electron density in the quantum well
P	optical power
P_{el}	electrical power
$P_{abs} = P_{el} - P$	absorbed power
q	elementary charge
Q	heat generation per unit distance
R	radius of curvature
$r, r1, r2$	amplitude reflection coefficients
$R, R1, R2$	Intesity reflection coefficients
RIN	relative intesity noise
R_L	load resistance
$S(z)$	time-averaged electromagnetic energy flux density
$\vec{S}$	Poynting vector
S/N	signal-to-noise ratio
T	sampling period time
T	temperature
$t, t1, t2$	amplitude transmission coefficients
$\bar{V}$	waveguide frequency parameter
V_{b}	barrier volume
V_{gr}	group velocity
V_{k}	kink voltage
V_{p}	photon volume
v_{ph}	phase velocity on the axis
V_{w}	quantum well volume

W_c	electron energy at the conduction band
W_g	bandgap energy
w_0	e^{-2}-beam half width
W_F, W_L	e^{-2}-beam half width of fiber and laser
W_v	electron energy at the valence band
z_R	Rayleigh range of Gaussian beam
α	intensity absorption coeffient
α_a	power attenuation coefficient
α_i	interinsic loss
β	propagation constant
ε	gain compression parameter
η	detector sensitivity
η_{d}	differential quantum efficiency
η_{i}	internal quantum efficiency
η_m	modal butt-coupling efficiency
γ	complex propagation consatant in z-direction
Γ_r	relative confinement factor
ν	light frequency
ω	angular frequency of light
σ	thermal coductivity
τ_{eff}, τ_p	photon roundtrip time and photon lifetime in the cavity
τ_{s}	carrier transport time
$\tau_{\mathrm{sp,w}}$, $\tau_{\mathrm{sp,b}}$	spontaneous emission time constants in the quantum well and barrier
Θ	e^{-2}-beam diffraction angle
θ_c	complment of critical angle for total internal reflection

Appendix C

List of Own Publications

- H.J. Unold, S.W.Z. Mahmoud, F. Eberhard, R. Jäger, and K.J. Ebeling, "Large-area single-mode VCSELs: approaches and experimental", *in Vertical Cavity Surface Emitting Lasers IV , SPIE Proc.*, vol. 3946, pp. 207–218, San Jose, CA, USA, January (2000).

- S.W.Z. Mahmoud, H. Unold, W. Schmid, and K.J. Ebeling, "Analysis of longitudinal lasing modes in long cavity VCSELs", *in Proc. Semiconductor and Integrated Optoelectronics, SIOE 2000*, Cardiff, United Kingdom April 2000.

- H.J. Unold, S.W.Z. Mahmoud, R. Jäger, M. Kicherer, M.C. Riedl, and K.J. Ebeling, "Improving single-mode VCSEL performance by increasing a long monolithic cavity", *IEEE Photonics Technol. Lett.*, vol. 12, pp. 939, (2000).

- H.J. Unold, S.W.Z. Mahmoud, R. Jäger, R. Michalzik, and K.J. Ebeling, "Spatially varied anti-resonant DBR design for large-area single-mode VCSELs", in Proc. *IEEE International Semiconductor Laser conference*, pp. 57–58, Monterey, CA, USA, Sept. (2000).

- H.J. Unold, M.C. Riedel, S.W.Z. Mahmoud, R. Jäger, and K.J. Ebeling, "Long monolithic cavity VCSELs for high singlemode output power", *Electronics Letter*, vol. 37, pp. 178, (2001).

- S.W.Z. Mahmoud, H. Unold, W. Schmid, R. Jäger, R. Michalzik, and K.J. Ebeling, "Analysis of longitudinal mode wave guiding in vertical-cavity surface-emitting lasers with long monolithic cavity", *Appl. Phys. Lett.*, vol. 78, pp. 586–588, 2001.

- Heiko J. Unold, Safwat W.Z. Mahmoud, Roland Jäger, Martin Grabherr, Rainer Michalzik and K.J. Ebeling, "Large-Area Single-Mode VCSELs and the Self-Aligned Surface Relief", *IEEE Journal on selected topics in quantum electronics*, vol. 7, pp. 386–392, (2001).

- S.W.Z. Mahmoud, D. Wiedenmann, M. Kicherer, H.J. Unold, R. Jäger, R. Michalzik, and K.J. Ebeling, "Spatial Investigation of Transverse Mode Turn-On Dynamics in VCSELs", *IEEE Photonics Technol. Lett.*, vol. 13, pp. 939, (2001).

- Heiko J. Unold, Safwat W.Z. Mahmoud, Roland Jäger, Matthias Golling, Max Kicherer, Felix Mederer, Michael C. Riedl, Thomas Knödl, Michael Miller, Rainer Michalzik and K.J. Ebeling, "Single-Mode VCSELs", *in Vertical Cavity Surface Emitting Lasers IV , SPIE Proc. Vol. 4649*, in Press, San Jose, CA, USA, January (2002).

Biography

Mr. Safwat William Zaki Mahmoud was born on 01.01.1966, in El-Minia, Egypt. In 1989, he received the B.Sc. degree in physics from El-Minia University. He joined to the Department of Physics, Faculty of Science in the same university as a research assistant. In 1994, he received the M.Sc. degree in physics from El-Minia University and became assistant lecturer. In 1996, he was awarded a scholarship from the Egyptian government and started his researches towards Ph.D. at University of Ulm, Germany.